Doctoral Dissertations   Student Theses and Dissertations

Fall 2020

Development of radiation transport techniques for modelling a high-resolution multi-energy photon emission tomography system

Seth Kilby

DEVELOPMENT OF RADIATION TRANSPORT TECHNIQUES FOR MODELLING

A HIGH-RESOLUTION MULTI-ENERGY PHOTON EMISSION TOMOGRAPHY

SYSTEM

by

SETH MICHAEL KILBY

A DISSERTATION

Presented to the Graduate Faculty of the

MISSOURI UNIVERSITY OF SCIENCE AND TECHNOLOGY

In Partial Fulfillment of the Requirements for the Degree

DOCTOR OF PHILOSOPHY

in

NUCLEAR ENGINEERING

2020

Approved by:

Joesph Graham, Advisor
Ayodeji Alajo
Xin Liu
Hyoung-Koo Lee
Andrew Hoffman

PUBLICATION DISSERTATION OPTION

This dissertation consists of the following three articles, formatted in the style used by the Missouri University of Science and Technology:

Paper I, found on pages 39-61, has been published in *Journal of Radioanalytical and Nuclear Chemistry*.

Paper II, found on pages 62–90, has been submitted for publishing in *Nuclear Instruments and Methods in Physics Research A: Accelerators, Spectrometers, Detectors and Associated Equipment*.

Paper III, found on pages 91-98, has been submitted to and has been published in the Proceedings of the American Nuclear Society Conference in Washington DC, in November 2019.

ABSTRACT

Nondestructive characterization techniques such as gamma tomography represent powerful tools for the analysis and quantification of physical defects and radionuclide concentrations within nuclear fuel forms. Gamma emission tomography, in particular, has the ability to utilize the inherent radiation within spent nuclear fuel to provide users with information about the migration and concentration of fission and activation products within the fuel form. Idaho National Laboratory is interested in using this technology to analyze new nuclear fuel forms for potential use in next generation nuclear reactors. In this work, two aspect of the system are analyzed. The first is a semi-analytic radiation transport methodology in conjunction with a parallel beam collimator developed to facilitate the acquisition of data from Monte-Carlo modeling of a small submersible gamma tomography system, with a focus on emission information. The second is a pinhole collimator designed to optimize count rates, diameter, and acceptance angle to increase the sampling of the fuel forms to decrease data acquisition time. Utilizing the semi-analytical technique, computational savings of 10^7-10^{11} can be achieved with a degradation in accuracy of 18-45% compared to a standard isotropic uniform Monte-Carlo N Particle transport simulation. However, this loss in accuracy can be minimized by increasing the parallel beam collimator's aspect ratio where it tends towards a degenerate cylinder. The semi-analytic technique is also compared to inbuilt acceleration techniques. The pinhole collimator design yields count rates on the order of 100s-1000s which represents a 10^1-10^2 increase in actual count rates over the entirety of the photon spectrum.

ACKNOWLEDGMENTS

Dr. Graham, you have been an extremely amazing advisor and life coach to me over the years. You have dealt with my often-bullheaded approach to certain trials and tribulations with a calm and collected demeanor, and you have provided advice when I was lost and needed some words of wisdom. Dr. Alajo, you have shown me nothing but kindness and care. Without your support and knowledge, I would not be the researcher I am today, and I would not have been able to be an effective ANS president. You have influenced me a great deal and made me a better person for it. Drs Lee and Liu, I had the pleasure of having you in various classes, and I have a tremendous respect for your decency and academic knowledge. Andrew Hoffman, you have been not only a friend, but somebody I have relied upon for so much. You put up with my often overdramatic and energetic rantings and ravings, and you are always somebody I can rely on to tell me the hard truths.

I would also like to thank my amazing family, friends, and Anthony Gomulka. Without your support I would not have made it through graduate school. Lastly, I would like to give a special thanks to the person who always believed in my dream. Grandpa, I love you, and I miss you. You were always my number one supporter, and I hope that I made you proud. I will always miss our discussions and time together, because so much of my worldview was influenced by you. You always cared deeply about my academic pursuits, and at the end of my educational journey the last thing that I can do is have you immortalized in my dissertation.

TABLE OF CONTENTS

LIST OF ILLUSTRATIONS

PAPER III

SECTION

LIST OF TABLES

1. INTRODUCTION

This dissertation presents work on the development of a Monte-Carlo radiation transport methodology for a submersible gamma tomography system. Gamma tomography is a nondestructive characterization technique that utilizes the inherent radioactive gamma emitters within an object. As a technique, it is useful for providing radionuclide concentrations within nuclear fuels for regulatory and fuel performance characterization. However, it is also widely used within the field of nuclear medicine to provide for noninvasive procedures. The technology, while not new, is constantly expanding and increasingly becoming a major tool for future fuel design and inspection. In the following pages of this dissertation, the reader is introduced to the motivation of this work, nondestructive characterization using gamma radiation, gamma emission tomography, components of gamma emission tomography, and an overview of the overall design and modelling techniques to solve these problems.

This dissertation, in the main body, contains three papers that have either been published within peer-reviewed journals or have been submitted. These papers outline in great detail the development and validation of a semi-analytic variance reduction method to increase the computational efficiency of Monte-Carlo radiation transport for high aspect ratio parallel beam collimators for gamma emission tomography applications, and the design and optimization of a pinhole collimator with a pixelated CZT detector. Paper I outlines the development of the semi-analytic Monte-Carlo variance reduction method and validation for a high aspect ratio pencil beam collimator design. Paper II focuses primarily on the comparison of global variance reduction techniques within MCNP. The semi-

analytic method developed in paper I is compared not only to a Markovian isotropic run, but also compared to commonly utilized methods, such as geometry splitting and DXTRAN spheres. Paper III contains work done on designing a pinhole collimator for the system. This paper looks at optimizing count rates within a CZT detectors with parameters such as magnification, effective diameter, and acceptance angle.

A section following Paper III is provided to provide a preliminary design of a fuel phantom and a uniform distribution that are scanned with the intent of an image being produced. In the final section of this dissertation, conclusions from the previously mentioned papers will be addressed. Additionally, the reader will find conclusions regarding modelling methodologies. Finally, the reader will find recommendations for future work in this area.

1.1. MOTIVATION

Idaho National Laboratory (INL), in an attempt to construct additional research capabilities at the Advanced Test Reactor (ATR), is interested in testing a prototype submersible gamma tomography system designed by the Graham Research Group at Missouri S&T. The prototype is meant to show a proof of concept that will aid lab researchers in the design and construction of more elaborate pool-side imaging systems. The push for gamma tomography systems is a symptom of the ever-increasing interest in designing next generation and accident tolerant nuclear fuels. The main downside of these newer nuclear fuel forms is the lack of a comprehensive body knowledge that encompasses fuel behavior as a function of burnup. For a new fuel composition to be considered for use in a nuclear reactor, the behavior of that fuel over time in a reactor is necessary. The ability

to utilize common destructive characterization methodologies is hampered by the reality that these methods such as electron microscopy are only capable of looking at nuclear fuel at a single burnup point. Therefore, destructive techniques are incapable of providing the physical and chemical changes of nuclear fuels over time. To capture the physical and chemical changes over many burnup points that nuclear fuel undergoes while in a reactor environment, nondestructive methods are needed for characterization, and that is the focus of what INL hopes to develop. INL recognizes the need for confidence that these new nuclear fuel forms will not cause large scale fuel cladding failure, a compromise of fuel integrity, or some adverse radionuclide buildup.

1.2. BACKGROUND

Nondestructive interrogation methods consist of a multitude of different techniques and strategies. Nondestructive methods are characterized by their use of radiation to examine materials without the need to physically alter them. Gamma emission tomography, in particular, has proven to be a valuable tool for researchers and international regulators. This technology has been historically been used to examine the internal structure and fission product distributions within spent nuclear fuels. It has also been used as a method to examine nuclear fuel materials for partial defects.

1.2.1. Nondestructive Characterization Using Radiation Imaging. Non-destructive nuclear fuel imaging techniques have provided researchers and inspectors around the world the ability to analyze nuclear fuels without the need to destroy samples. The imaging methods that are the most common utilize neutrons, X-rays, or gamma rays.

Neutron interrogation generally provides information on structural integrity and fissile content. The benefits of using neutrons for imaging purposes include the ability to acquire higher spatial resolution images than photon-based radiation. Neutrons are also beneficial at interrogating well shielded containers at border crossings where heavy metal shielding is likely for concealing contraband material. Neutron imaging and interrogation techniques are dependent on the quantity of light elements such as hydrogen as opposed to the proton number that affects photon-based techniques. Neutrons within a light element scatter readily. However, in high proton number media such as lead, Neutrons do not readily scatter, and therefore have high penetration power. This results in the ability for neutrons imaging to have greater contrast in internal structures of high proton number materials whereas X-rays or lower energy gamma rays would just attenuate. This difference is seen in Figure 1.1
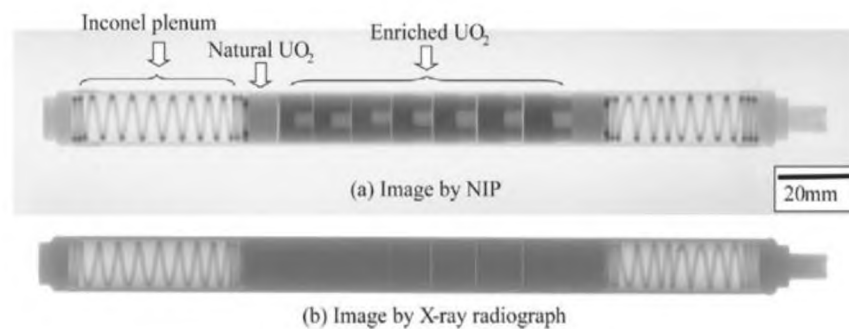
Figure 1.1: Neutron (a) and X-ray (b) images of a fresh variable enrichment nuclear fuel rod, and plenum [1], [2]

The neutron imaging technique better resolves the internal structure of the enriched uranium, and it is capable of discerning enrichment variations throughout the fuel material.

Whereas the X-ray imaging method is incapable of discerning the internal fuel structure let alone the enrichment variations. Additionally, neutron imaging provides greater contrast on the spring mechanisms within the fuel. This is a byproduct of the neutrons having higher contrast capabilities in the plenum region as well. However, neutron imaging is also important in determining the presence of fissile content. Since neutrons impinging upon a fuel assembly can induce a reaction, it is possible to use the induced fast neutrons for imaging purposes to determine where fission is occurring. An example of using neutron imaging on a nuclear fuel bundle can be seen in Figure 1.2
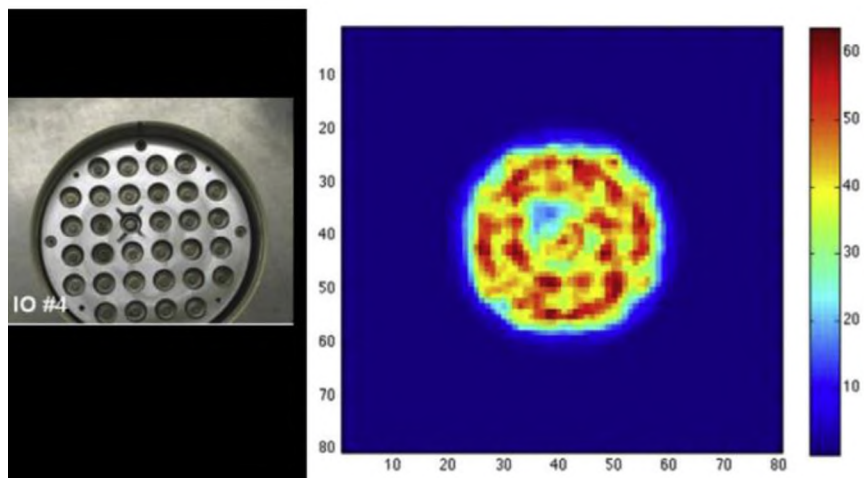
Figure 1.2: Emitted fast neutron tomograph of a MOX fuel assembly with a DU pin marked by an X on left [1], [3]

X-ray imaging, like neutron imaging, is also commonly used in fuel interrogation experiments. However, X-ray imaging is primarily useful to analyze cladding materials that encapsulate nuclear fuels. This is a direct response to the inability for X-rays to discern differences in materials with similar mass densities. Consequently, the data received is less

spatially resolved than that of neutron tomography. With the rise of interest in new fuel forms such as TRISO, X-ray imaging has been used to determine fuel kernel leakage into the surrounding pyrolytic carbon buffer zone within Tri-structural ISOtropic (TRISO) fuel. Since X-rays cannot discern differences in materials with similar mass densities, a Phase Contrast Imaging (PCI) regime can be utilized to mitigate the loss in contrast. This method is primarily useful in the analysis of TRISO particles where the physical particles are less than 1 mm wide. PCI works by analyzing the differences in refractive indexes between phase boundaries. When applying the associated post processing to PCI data, Figure 1.3 is obtained.
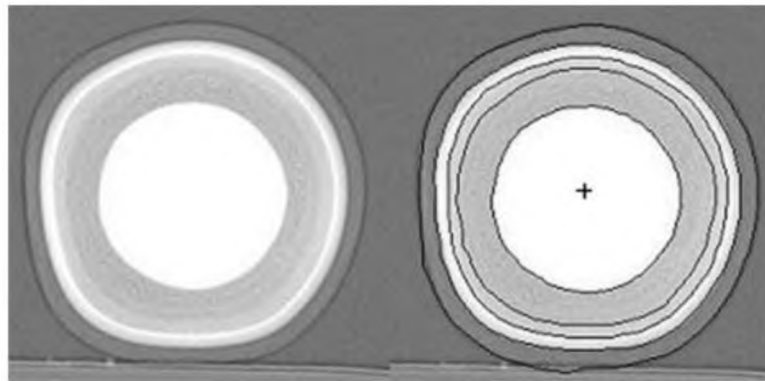
Figure 1.3: X-ray image of a TRISO particle (Left) and an X-ray image of a TRISO particle using PCI (Right) [1], [4]

As seen in the figure above, it is possible to characterize materials with similar mass densities using PCI. However, in quasi-homogenous materials such as nuclear fuel, X-rays simply do not have the ability to spatially resolve internal features within uranium fuel as was seen in Figure 1.1.

The ability to analyze fission products and fissile content through the use of radiation is primarily reserved for gamma ray imaging such as with a passive gamma emission tomography system. Historically, organizations such as the International Atomic Energy Agency use gamma ray imaging as a robust compliance tool to ensure a nation's cooperation with the Nonproliferation of Nuclear Weapons Treaty and the Additional Protocols, and organizations use gamma detection systems at border crossing to determine if illicit nuclear material is entering [5]–[12]. Researchers have been using gamma radiation for partial defect analysis and fission product quantification at the Halden Reactor Project [1] [13]–[22]. This work attempts to map a boiling water reactor (BWR) fuel assembly and provide information regarding Cs-137 and La/Ba-140 concentration. This not only provides information on the location of fission products, but also the ability to see if fuel has been diverted for use in nuclear weapons. Both of these instances can be seen in Figure 1.4.
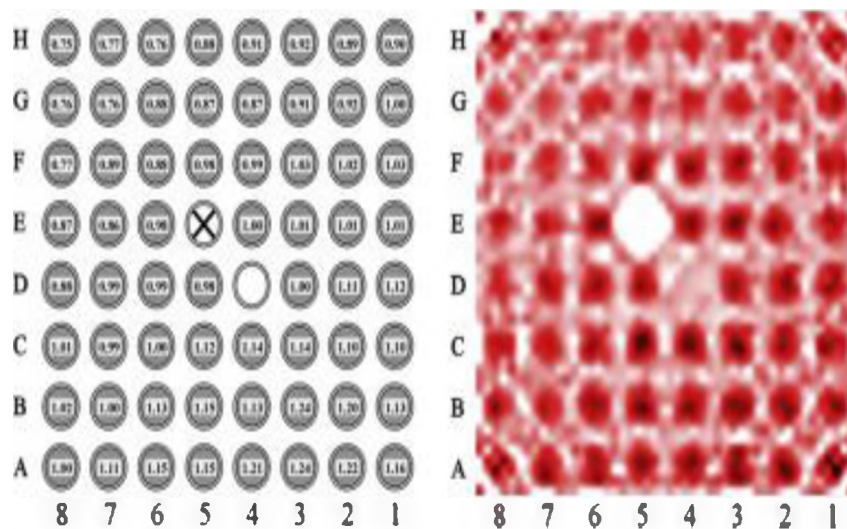
Figure 1.4: Left: Fuel assembly map where the "x" represents a missing rod and the blank circle represents a swapped rod. Right: Cs-137 tomogram and corresponding qualitative fission product concentration in each rod [1]

While nondestructive characterization is useful for compliance of international laws and standards, over the last few decades there has been an increasing reliance on utilizing this technology to analyze the behavior of fission products and associated activation products to quantify fuel performance for improving fuel design and lifetime.

1.2.2. Gamma Emission Tomography. Gamma emission tomography is a specific class of nondestructive testing that is common not only in nuclear engineering, but also within the field of radiation oncology. Gamma emission tomography is used in techniques such as Single Photon Emission Computed Tomography (SPECT) or Positron Emission Tomography (PET), common forms of nuclear medical imaging. SPECT and PET work by injecting a patient with a radioactive tracer element. The tracer uptakes to a specific part of the body that is dictated by the chemical nature of the tracer. The radionuclide tracers that are commonly used are Tc-99m and I-123 [23]. These radionuclides produce a gamma with a single energy of approximately 140 keV that is then captured with a gamma imaging device and an associated activity map of the internal organ is generated from a series of radiographic projections. For PET, a positron annihilation event occurs and, as a result, two 511 keV photons are emitted 180° apart and captured by a gamma imaging device in coincidence. Tracers again undergo uptake into a specific part of the body such as the heart. Tracers such as F-18, O-15, Rb-82, and N-13 are commonly used in these cardiac based imaging regimes, and they radioactively decay while emitting a positron [24]. This positron annihilates with an electron producing the two 511 keV photons.

Gamma emission tomography of nuclear fuels operates similarly to these common medical techniques. Spent nuclear fuel contains a multitude of internal high activity fission

products such as Cs-137, Nb-95, La/Ba-140, and many others. These fission products produce gamma rays from radioactive decay and are capable of being captured in a gamma camera system. By using the emitted gamma radiation over the course of many projections an activity map can be generated. Gamma emission tomography attempts to map the location and concentration of radionuclides within nuclear fuel materials. These radionuclides diffuse over the course of fuel lifetime in a reactor as the fuel depletes. Understanding the nature of fission product migration is important in the analysis of next generation nuclear fuels. The benefit of gamma emission tomography is that an activity map of fission products can be acquired as a function of burnup. Fission products can migrate to physical abnormalities such as cracks or voids as the nuclear fuel depletes and becomes damaged. As they migrate, and eventually congregate, they emit gamma rays proportional to the activity within that localized volume of radionuclides. However, each fission product behaves differently. For example, a fission product such as Eu-154 is less mobile than Cs-137. Eu-154 tends to maintain a uniform distribution throughout the fuel over large burn histories. Cs-137, on the other hand, tends to deplete in the center of the fuel causing a depression and migrates more to the peripheral areas of the fuel as seen in Figure 1.5. The cause of the migration within standard UO_2 ceramic fuel is well known. The europium fission product lacks gaseous precursors and is non-volatile at standard operating temperatures which drives the uniform distribution. Cesium migration, on the other hand, is influenced by three main constituents. One, migration will not occur if the fuel centerline temperature is below 1473 K [20], [25]. Two, the ratio of oxygen to metal also influences migration.
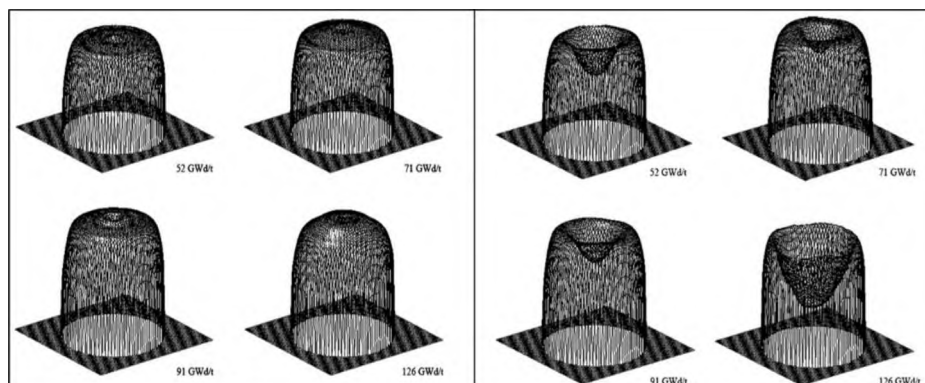
Figure 1.5: (Left) Activity distribution of Eu-154 in UO_2 from 52 GWd/t to 126 GWd/t acquired through gamma emission tomography. (Right) Activity distribution of Cs-137 in UO_2 from 52 GWd/t to 126 GWd/t acquired through gamma emission tomography [20]

If that ratio is high, then the cesium is less likely to migrate and vice-versa. Three, burnup and fuel density play a role as well. As fuel depletes, the mass density of the fuel will decrease. As this occurs, cesium tends to migrate outward within the nuclear fuel.

Gamma emission tomography is a powerful tool that allows researchers to look within high density materials through the use of gamma radiation. This technique relies upon the signal from internal radionuclides, and for these systems to work properly, it is imperative to have robust detector systems coupled with collimation. These components of gamma tomography need to be specifically designed for this application. The interactions between gamma radiation and nuclear fuels, gamma rays and collimators, and gamma rays and detector materials are important to characterize when designing these systems.

1.3. COMPONENTS OF GAMMA EMISSION TOMOGRAPHY

Gamma emission tomography consists of two main constituents outside of the source material. In order to acquire images from radiation, one needs both a collimator and detector system. The collimators attenuate and focus source photons into a cone or parallel

beam to examine smaller sub-volumes of the overall specimen. Detectors are used to count and record photon data. This data is used as the basis for reconstructing an image.

1.3.1. Collimators. Outside of the source, there are other key constituent components that are needed to utilize gamma emission tomography. Collimators play an integral role in filtering scattered gamma radiation and defining a component of the overall spatial resolution of the system. All gamma emission tomography systems utilize collimators to improve the quality of the resulting image and to minimize the impacts that scatter has on the degradation of image quality.

To reduce the adverse effect that scattered photons have on the system, high Z-number materials with high mass densities are used to create a shield that stops photons outside of the imaging plane from being scored in the detector system. In a sense, these act as tunnels for photons already in the imaging plane, and a barrier to those outside the plane. The three main physical properties that affect a material's ability to attenuate are: energy of the incoming gamma, thickness of the material, and mass density of the material. The relationship that describes the interplay of these parameters on a beam of photons, in a given material, is the Beer-Lambert law in Equation 1

$$I_f = I_o e^{-\mu x} \tag{1}$$

where I_f is the final intensity of the photon beam, I_o is the initial intensity of the photon beam, and $e^{-\mu x}$ is the exponential of linear attenuation, μ, multiplied by thickness, x. When designing collimators, the goal is to maximize $e^{-\mu x}$. To maximize the exponential, there are two main approaches. One, choose a high-density, high Z-number material. Two, increase the thickness of that material. High density, high z-number materials are chosen for these applications due to superior mass attenuation compared with low density

materials. Lead and tungsten will attenuate more photons than that of a material like carbon. The exception to this is if a photon has an energy well within Compton energy ranges. At these energies, materials, despite having potentially drastic variations in Z number, have similar mass attenuation coefficients. This is due to the strong dependence the Compton interaction has on high electron density. Low Z materials are more electron dense than high Z materials. This causes lighter elements to perform comparable to high Z elements. This can be seen in Figure 1.6.
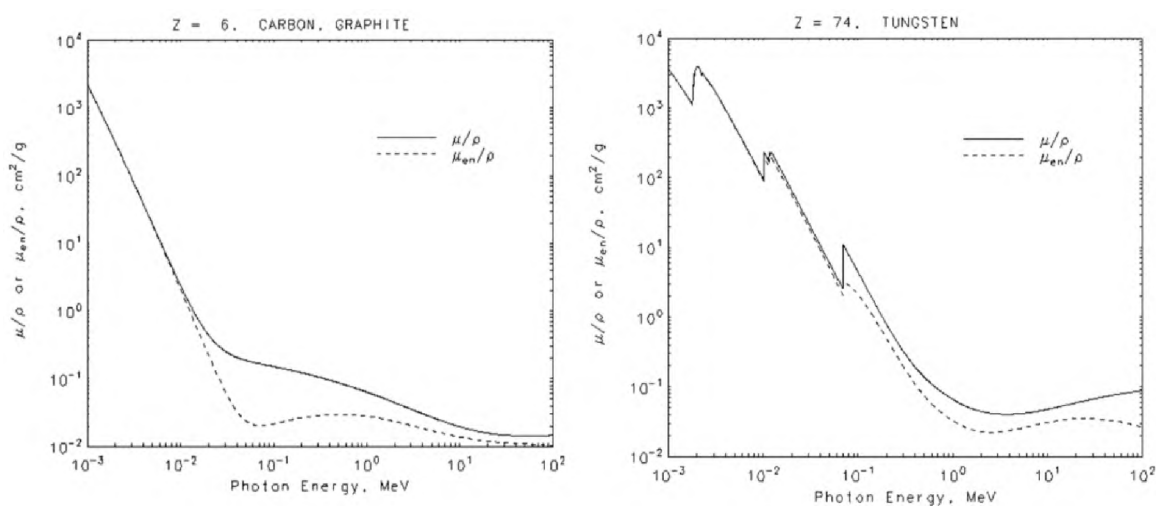
Figure 1.6: Mass attenuation of carbon from 0-20 MeV (Left) and mass attenuation of tungsten from 0-20 MeV (Right) [26]

While photon energy plays a significant role in the attenuation coefficient in gamma emission tomography of nuclear fuels, it is a variable that cannot be controlled as the user has no way to partition all radionuclides of a given type to well defined sub-volumes in the nuclear fuel material, but the user does have the ability to choose the medium that the nuclear fuel resides. While the nuclear fuel materials are relatively mass dense and consist

of high z elements such as uranium and plutonium, the medium surrounding the nuclear

fuel specimen

Primarily, for gamma emission tomography systems a specific class of collimators

called parallel or pencil beam collimators is used. These allow researchers to analyze a

subtended volume within the fuel by minimizing the scattered photons. An example

detection system can be seen in Figure 1.7.
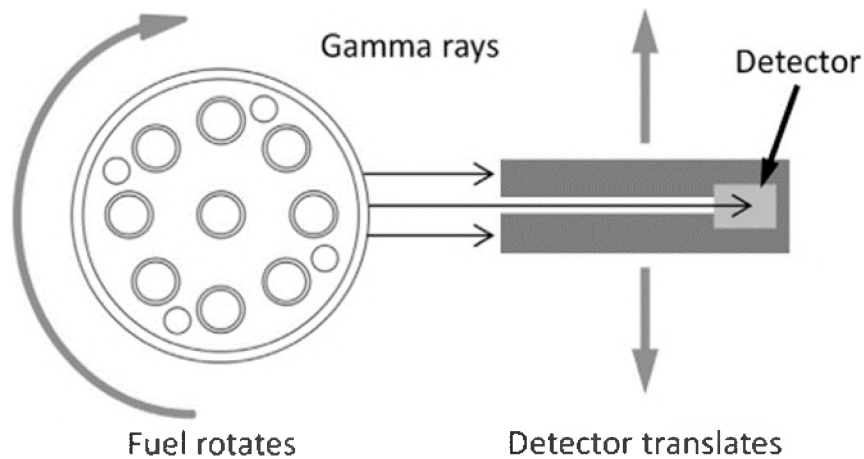
Figure 1.7: Gamma emission tomography system drawing of the Halden Reactor Project
system [27]

By utilizing parallel beam collimators, photons that are outside the collimator

aperture plane are subjected to high mass dense materials, which reduces the photon

intensity that could interact with the detector. As a result, data can be acquired from a slice

of the fuel that is approximately the dimension of the collimator aperture. Consequently,

in order to scan the entirety of the fuel assembly, thousands of projections are measured.

Moreover, as counterintuitive as it may seem, this is a benefit to the overall reconstructed

data set. In the case of the parallel beam geometries, each projection is a single parallel slice of the material, and as a result reconstructions can take on the order of 10^4 scans to create [13], [17]. More projection sets imply smaller collimator sizes or a reduction in rotation angle steps which improves a parameter known as spatial resolution.

Spatial resolution from a parallel beam collimator in 1D can be approximated by Equation 2 seen below.

$$R(FWHM) = \frac{DZ}{L} \qquad (2)$$

where D is the diameter of the collimator aperture, Z is the distance from the object plane to the detector, and L is length of the collimator [28]. The collimator spatial resolution will always be larger than the physical diameter of the aperture unless Z is minimized, and L is maximized. The overall resolution is mainly dictated by the diameter of the aperture. However, by doing this optimization problem, the count rates will be affected.

Within this dissertation, a pinhole collimator system is also investigated. Pinhole collimators are similar to parallel beam collimators in that they attenuate radiation, and they are a driver of overall system spatial resolution. However, pinholes have larger fields of view than parallel beams of similar aperture radii. Within a pinhole, there is an acceptance angle that governs a conical field of view whereas a parallel beam collimator has a significantly smaller acceptance, or divergence, angle, but the field of view is approximately cylindrical as the radius approaches zero. Pinhole collimators can be used to take multiple parallel projections simultaneously with some pixelated detector or other high spatial resolution data acquisition systems such as CCDs [29]–[31]. An example pinhole collimator diagram can be seen in Figure 1.8
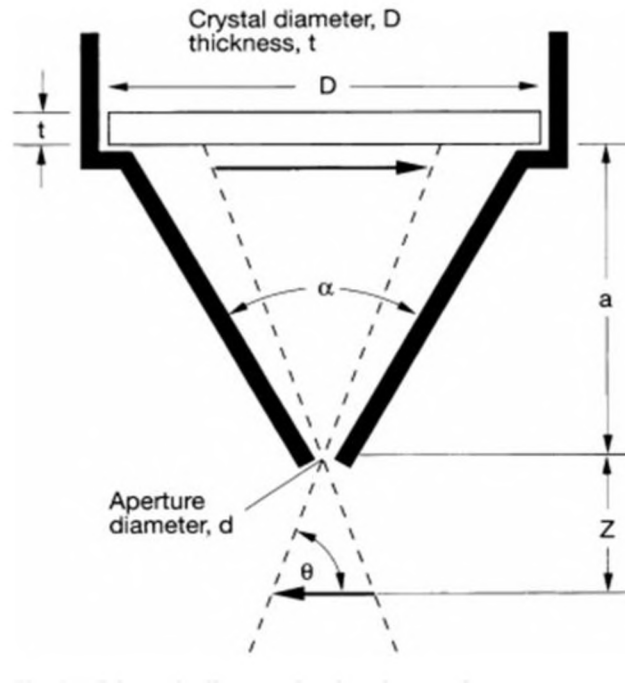
Figure 1.8: Diagram of a Pinhole collimator [32]

Pinhole collimators are used commonly in small animal SPECT applications and within Anger Cameras [29], [30], [33]–[36]. This allows for multiple projections to be taken simultaneously. However, by introducing a pinhole collimator, the spatial resolution needs to be corrected for the possibility that a photon will traverse through the septa, points where there is less attenuating material. The 1D spatial resolution for pinhole collimators can be approximated by using Equation 3.

$$R(FWHM) = \frac{(a + Z)}{a} d_e \tag{3}$$

where R is the resolution, a is the distance from the aperture to the detector, Z is the distance between the object and the aperture, and d_e is the effective diameter, which corrects for any streaming through the septa, calculated in Equation 4 [32], [37].

$$d_e = [d(d + 2\mu^{-1}tan\frac{\alpha}{2})]^2 \qquad (4)$$

d is the diameter of the pinhole, μ^{-1} is the mean free path of the photon, and α is the acceptance angle.

The effective diameter is always larger than the physical diameter, and the energy of the incoming photon has a direct impact on the collimator spatial resolution. In the case of gamma tomography of nuclear fuels, the resolution will depend upon which radioisotope is being counted. The collimator spatial resolution of Cs-137 for example will not be the same as the collimator spatial resolution of Eu-154 due to differing photon emission energies.

When comparing the two types of collimator systems, the parallel beam geometry allows for higher spatial resolution as there is a large acceptance angle, and there are not septa for photons to stream through. The geometry is heavily dependent on the aperture size. Pinhole collimators allow for parallel counting meaning that they can take multiple parallel projection sets at once. Each pixel represents a singular parallel projection. The benefit is that a user can reduce the scanning time by counting parallel, and the count rates over the detector volume are greater, since the source is likely completely encapsulated within the field of view. The main downside is the loss in spatial resolution. Since pinhole collimators have pronounced acceptance angles, the ability for photons to scatter into a given pixel increase, because more of the material is being sampled. Likewise, the introduction of areas where the collimator material is thinner can lead to streaming, or small angle scatter that will erode image quality.

1.3.2. Scintillator and Semiconductor Detector Systems. Collimators are just one aspect of gamma emission tomography data acquisition systems. In order to score and

count radiation, detectors are required. Within gamma emission tomography, there are primarily two classes of detectors that are considered. One being scintillators and the other being semiconductors.

Scintillator detectors convert radiation, such as photons and neutrons, into light which creates photoelectrons that are multiplied in a photomultiplier tube. A diagram of a generic scintillator is shown in Figure 1.9.
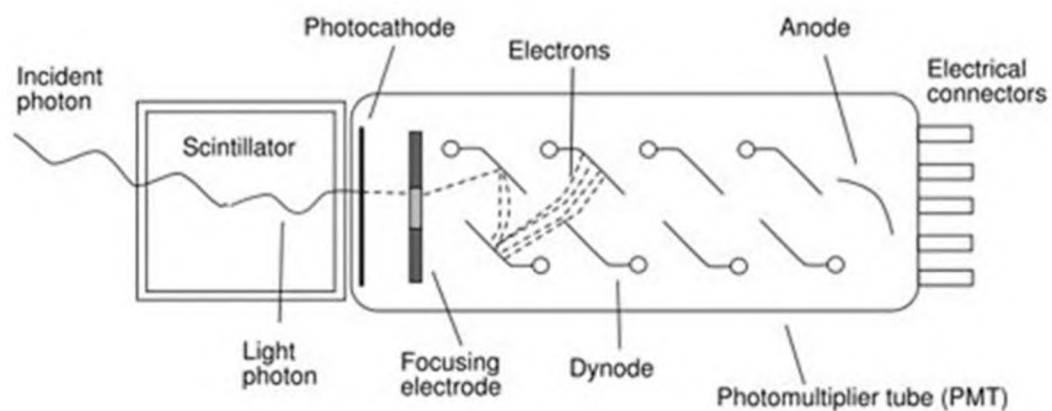
Figure 1.9: Diagram of a generic scintillator

Scintillator detectors work when incoming radiation interacts within the crystal. When the radiation imparts energy to the crystalline structure, an electron-hole pair is created. These pairs create more pairs in a cascade effect until the energy of the particles drop below the gap energy of the crystal. Afterwards, the pairs will travel within the crystal to luminescent centers, and these create the scintillation photons [38], [39]. The photons then interact with the photomultiplier tube, creating photoelectrons. The photomultiplier tube then multiplies these photoelectrons in order to correlate them to signal.

Scintillators are commonly used in gamma emission tomography applications in the medical field [40]–[45]. These detector types have some advantages over their semiconductor counterparts in this field. Inorganic scintillators have generally high densities, compared to gas detectors, high effective Z numbers, high stopping power, large light yields, and the number of photons generated is linear with respect to energy. A list of common inorganic scintillators and their associated properties can be seen in Figure 1.10.

	Specific Gravity	Wavelength of Max. Emission	Refractive Index	Decay Time (μs)	Abs. Light Yield in Photons/MeV
Alkali Halides					
NaI(Tl)	3.67	415	1.85	0.23	38,000
CsI(Tl)	4.51	540	1.80	0.68 (64%), 3.34 (36%)	65,000
CsI(Na)	4.51	420	1.84	0.46, 4.18	39,000
LiI(Eu)	4.08	470	1.96	1.4	11,000
Other Slow Inorganics					
BGO	7.13	480	2.15	0.30	8200
CdWO₄	7.90	470	2.3	1.1 (40%), 14.5 (60%)	15,000
CaWO₄	6.1	420	1.94	8	15,000
SrI₂(Eu)	4.6	435		1.2	85,000
ZnS(Ag) (polycrystalline)	4.09	450	2.36	0.2	
CaF₂ (Eu)	3.19	435	1.47	0.9	24,000
Unactivated Fast Inorganics					
BaF₂ (fast component)	4.89	220		0.0006	1400
BaF₂ (slow component)	4.89	310	1.56	0.63	9500
CsI (fast component)	4.51	305		0.002 (35%), 0.02 (65%)	2000
CsI (slow component)	4.51	450	1.80	multiple, up to several μs	varies
CeF₃	6.16	310, 340	1.68	0.005, 0.027	4400
Cerium-Activated Fast Inorganics					
GSO	6.71	440	1.85	0.056 (90%), 0.4 (10%)	9000
YAP	5.37	370	1.95	0.027	18,000
YAG	4.56	550	1.82	0.088 (72%), 0.302 (28%)	17,000
LSO	7.4	420	1.82	0.047	25,000
YSO	4.54	420		0.070	24,000
LuAP	8.4	365	1.94	0.017	17,000
LaCl₃(Ce)	3.79	350		0.028	46,000
LaBr₃(Ce)	5.29	380	2.05–2.10	0.026	63,000

Figure 1.10: List of common inorganic scintillators and their associated properties [38]

Scintillators have higher intrinsic efficiencies than their semiconductor counterparts, with the exception of well-type semiconductors [46]. The efficiency is calculated by the ratio between counts recorded into the detector and the source emitted gammas as seen in Equation 2

$$\varepsilon = \frac{N_p}{N_q} \tag{5}$$

where N_p is the number of pulses, and N_q is the number of radiation quanta incident on the detector surface [38], [47]. By having higher efficiencies, scintillators will record more counts per a given gamma emission over their semiconductor counterparts for a similar detection geometry. Scintillators lack the energy resolution of semiconductor counterparts, and the resulting photopeaks are broader in energy, and the amplitude is smaller. Scintillator fluorescence properties are also resilient to temperature changes, and as a result, can operate without the need for cryogenic cooling to correct for drift in photopeak position [48]. However, most scintillators tend to be hygroscopic, which means that the properties will degrade when exposed to water. Therefore, these detectors have to be encased and insulated against water ingress.

Scintillators are not a monolithic class of detectors. There are many property variations in different classes of scintillator detectors. For example, while scintillators do lack the energy resolution that semiconductors offer, this can be ameliorated by choosing a different type of scintillator detector. NaI, which is probably the most common of scintillators, has an energy resolution at 662 keV of 7-8%. $LaBr_3$, which is a cerium activated scintillator, has an energy resolution of 2.2-2.6% at 662 keV [49]. The wavelength of light that is generated from a scintillation reaction is not the same for different classifications of detectors. For example, NaI scintillation events lead to the creation of light with a wavelength of 415 nm; $LaBr_3$ scintillators release light with a wavelength of 380 nm. This becomes relevant when designing the data acquisition system.

Different photomultiplier tubes or CCD chips have higher conversion factors, or high quantum efficiencies, when examining particular wavelengths of light.

For imaging systems, the method of data acquisition is important. Scintillators coupled with high spatial resolution CCDs (EM-CCDs and I-CCDs) can spatially resolve an object on the order of 10^1-10^2 micron with high quantum efficiencies [50]–[55]. Quantum efficiency of these CCDs is dependent on the wavelength of light that the scintillator emits. For example, a CCD97, a type of EM-CCD, is 90% efficient between 500-650 nm, but degrades to approximately 50% at 380 nm [56]. Therefore, when choosing a readout device, the electronics need to be optimized for the scintillation wavelength. CCD chips also need to be cryogenically, or Peltier cooled as dark current rises with temperature as seen in Figure 1.11
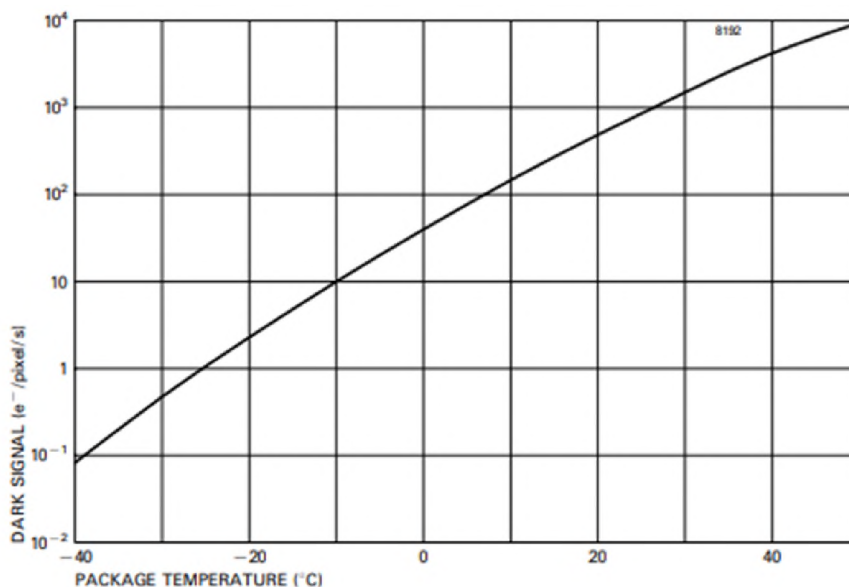
Figure 1.11: Dark Current curve for a CCD97 with respect to temperature [56]

Dark current is the signal associated with electron-hole pairs occurring in the CCD chip due to thermal energy imparted on the electron being higher than the gap energy in the readout device. This can lead to inflated signals within a pixelated medium like CCDs and can be a main driver of noise. Consequently, cooling is necessary to reduce the impact that dark current has on the ability to resolve images. The main downside to using CCDs for nuclear fuel imaging is the large degradation in energy resolution. This degradation from work done by the Beekman group in the Netherlands was anywhere from 34-65% at 141 keV for differing crystal thicknesses, which is more than the typical energy resolutions of the crystals themselves [30]. This means that despite the incredibly high spatial resolutions (80-148 micron) this system would not be able to distinguish between closely aligned photopeaks in a gamma spectrum of nuclear fuel.

CCDs are not the only option for scintillation-based imaging devices. Position sensitive PMTs and SiPMs can be used to image objects as well. Position sensitive PMTs have the benefit of having low readout noise, but they have low quantum efficiencies and larger pixel elements compared to CCDs and position sensitive PMTs. Position sensitive PMTs also contain the ability to localize gamma interactions due to the splitting of the PMT anode into multiple parts, and they also tend to have smaller elements over traditional PMTs, which makes them viable for imaging purposes [57]–[64]. SiPMs are silicon-based photomultiplier tubes that consist of a large array of avalanche photodiodes in Geiger mode. These diodes are biased with high voltages to ensure that the signal is maximized when one or more optical photons are absorbed [65]–[67]. They are used primarily in applications where temporal resolution is important due to superior timing resolution and low noise, but they have low quantum efficiencies. While SiPMs have found use in imaging

systems individually, they can also be used in conjunction with a CCD to improve energy resolution by accounting for more scintillation signal that would otherwise not interact with a scintillator-attached CCD.

Semiconductor detectors are another classification of detection system that are commonly used in emission tomography of spent nuclear fuel. Semiconductor based radiation detection system operate by using ionizing radiation to impart enough energy to surpass the gap energy threshold for electrons to move between valence and conduction bands. When an electron leaves the valence band and jumps to the conduction band, a hole is created. These electron-hole pairs are then biased towards either an anode or cathode. This phenomenon is shown in Figure 1.12.
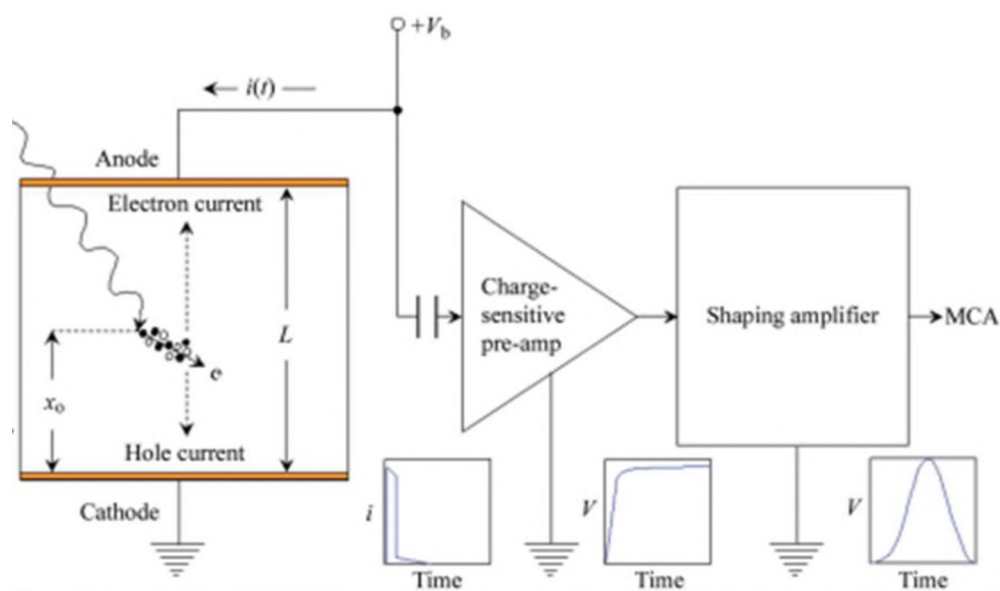
Figure 1.12: Example schematic of a semiconductor planar detection system. Electron-hole pairs are created from ionizing radiation directly proportional to the energy deposited [68]

The number of electron-hole pairs generated is directly related to the energy deposited by the incoming radiation and the energy required to produce a pair. As long as charge carriers are in motion signal is induced. This direct conversion only requires one stage, whereas scintillators require more than one stage to produce signal. and in order to produce a charge carrier pair within a scintillator the energy requirement is an order of magnitude higher than typical semiconductors [69].

The main reason these systems are utilized is for their superior energy resolution capabilities, usually below 1% at 662 keV. Despite the lack of inherent intrinsic efficiency, semiconductor detectors are preferred when imaging nuclear fuels, because of high energy resolution. Scintillators traditionally record more counts per radiation quanta in an energy bin defined by the FWHM of the photopeak, but since the FWHM is wider, the amplitude of the photopeak is narrower. When coupled with a shorter photopeak over wider energy ranges, scintillators such as NaI lack the ability to resolve photopeaks that are within the Compton regions of other higher energy photopeaks in nuclear fuels due to the proximity of the gamma rays in energy. Since semiconductors have high energy resolution, the counts distributed over the FWHM are fewer, but the amplitude of the photopeak is higher. This allows semiconductor detectors to have high Peak-to-Compton ratios. Therefore, they are generally capable of resolving lower energy photopeaks in the presence of higher energy peaks [38]. Because semiconductors yield high energy resolution, they are an alternative to scintillators in imaging applications and radioisotope identification [70]–[75].

Semiconductors detectors, like scintillators, are not a monolithic group as properties do vary among different semiconductor type detectors. A main difference is the requirement for cryogenic or electric cooling. For example, HPGe, a very commonly used

detector, has a band gap energy of 0.67 eV at 300 K [76]. Due to this relatively low band gap energy, cooling is required to reduce dark current effects within the detection system. However, not all semiconductors require cooling. Solid state semiconductors, like CdZn and CdZnTe (CZT) semiconductors do not require cooling mechanisms as the gap energy is greater than 1 eV, but each of these semiconductors still offer superior energy resolution. The main downside to utilizing these detectors over scintillators is the cost required for thicker semiconductor crystals. This is especially important in gamma tomography of nuclear fuels, because semiconductors need to be thicker to maximize the likelihood of photon interaction. CZT is more difficult to manufacture than other semiconductors, which limits the ability to have thick crystals.

Imaging using semiconductor detectors is common in nuclear fuel and nonproliferation applications. HPGe detectors are usually combined with a parallel beam collimator to define spatial resolution of the projections. However, using a monolithic spatially insensitive imaging device is time consuming as thousands of projections are needed for a reconstruction. In addition, the ability for HPGe to be used with pinhole collimators is limited. However, over the years there have been attempts to utilize segmented HPGe detectors for position sensitive applications, including Compton cameras with spatial resolutions ranging from 0.5 mm to 2 mm [77]–[80]. An alternative imaging system for pinhole applications is to utilize a position sensitive pixelated CZT detector. CZT is an attractive semiconductor material due to its relatively large bandgap energy, which means it can operate at ambient temperatures, and they offer better spatial and energy resolution than NaI scintillators for SPECT,PET, and gamma spectroscopy applications [81]–[85].

CZT imaging systems, however, have issues with charge carrier trapping, carrier diffusion, and charge induction efficiency variations within pixel positions in the grid. Since CZT is a compound semiconductor, it is more prone to charge carrier trapping which results in a tail effect on the photopeaks as seen in Figure 1.13.
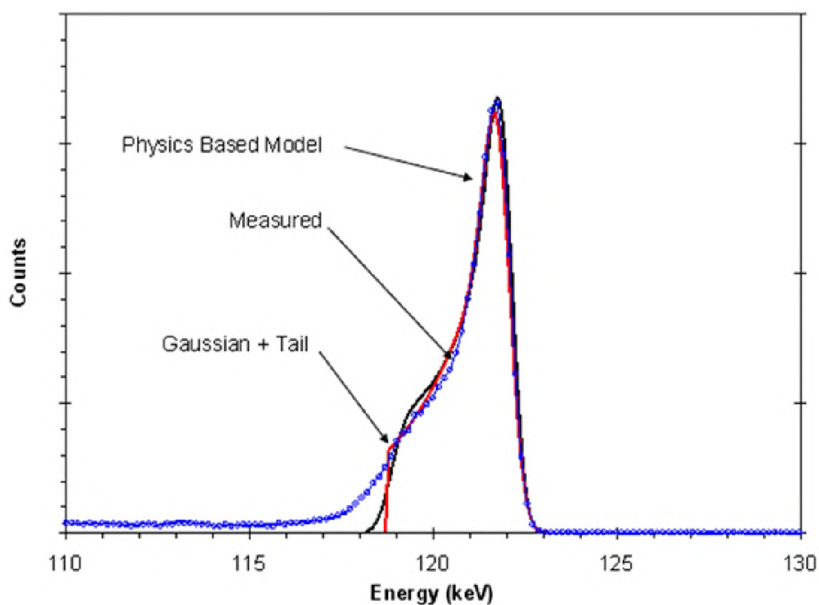
Figure 1.13: Plot comparing a charge carrier trapping model with measured results (blue), a model of charge carrier traping (black), and a fitted gaussian function (red) [86]

This is the result of photons being incorrectly scored at lower energies instead of within the photopeak area. Carrier diffusion within the pixelated CZT array is a concern for inner pixels and for small pitch pixels, because of the greater number of neighboring pixels and the inherent diffusion length of charge carriers within the medium [69]. Charge induction efficiency is a measure of charge generation at a given location. Charge induction efficiency should be maximized but remain constant over the thickness, from cathode to anode, of the crystal. Any reduction in charge induction efficiency can lead to loss in

energy resolution as low values imply tail effects on the photopeaks. This is mitigated by providing a bias voltage that is large and constant, to ensure only a drop in charge induction efficiency toward the anode. Therefore, the depth of interaction is not as important of a parameter unless the photon is interacting close to the anode. When weighing these parameters, it is important to note that thick CZT crystals are expensive, and imaging nuclear fuels requires thicker crystals due to energies from 600-800 keV.

The size of the pixels on the CZT grid impact the spatial resolution of the resulting imaging. Utilizing smaller pixels allows for finer spatial resolution, but the spatial resolution is only partially dependent on the detector. Collimation, as mentioned prior, also influences the overall system resolution. For any detector, the total 1D spatial resolution can be defined as a function of detector resolution and collimator resolution as shown in Equation 6

$$R_0 = \sqrt{R_c^2 + \left\{\left(\frac{Z}{a}\right)R_i^2\right\} + R_s^2} \tag{6}$$

R_c^2 is the square of the collimator resolution, Z is the distance from the object to the aperture, a is the distance from aperture to detector, and R_i^2 is the square of the intrinsic resolution from the detector. R_s^2 is the component of the resolution from scattering. Scattering always increases overall system spatial resolution, but this effect can be minimized with optimized pixel sizing and energy windowing. By combining a collimator, source, and detector a gamma tomography system can be designed and modelled. The design choices and modelling are introduced in Section 2.

2. DESIGN AND MODELLING

2.1. DESIGN APPROACH

The proposed design for a submersible gamma tomography system incorporates solutions for common design challenges. These challenges consist of the system being underwater, low sampled activity from the fuel specimen, irregular irradiation and decay cycles at the ATR, quantity of detector positions, and the ability to acquire data within a workday. The current design is rated for underwater use, and it attempts to ameliorate low sampled activity from imaging test fuels instead of full-scale assemblies. The irregular irradiation and decay cycles of the ATR are considered and implemented in the modelling and are considered within the physical design. Lastly, the quantity of detector positions or radiographic projections is considered, and this system is capable of completing them within a workday.

The proposed gamma tomography design consists of two main data acquisition modes. One is a gamma transmission tomography system to examine physical changes within the nuclear test fuels. The focus of this is to use an interrogating Co-60 source to examine the nuclear fuel and acquire information about physical abnormalities as a function of fuel depletion. The second, which is the focus of this dissertation, is a gamma emission tomography system. This system would try to acquire information about chemical buildup and radionuclide concentrations as a function of fuel depletion. However, due to the expensive nature of high energy resolution detection systems, the gamma emission tomography component will not be implemented in the final design. The main feature of the final design is the gamma transmission tomography mode. However, the gamma

emission tomography mode does share many of the same constituent components. The final design can be seen in Figure 2.1.
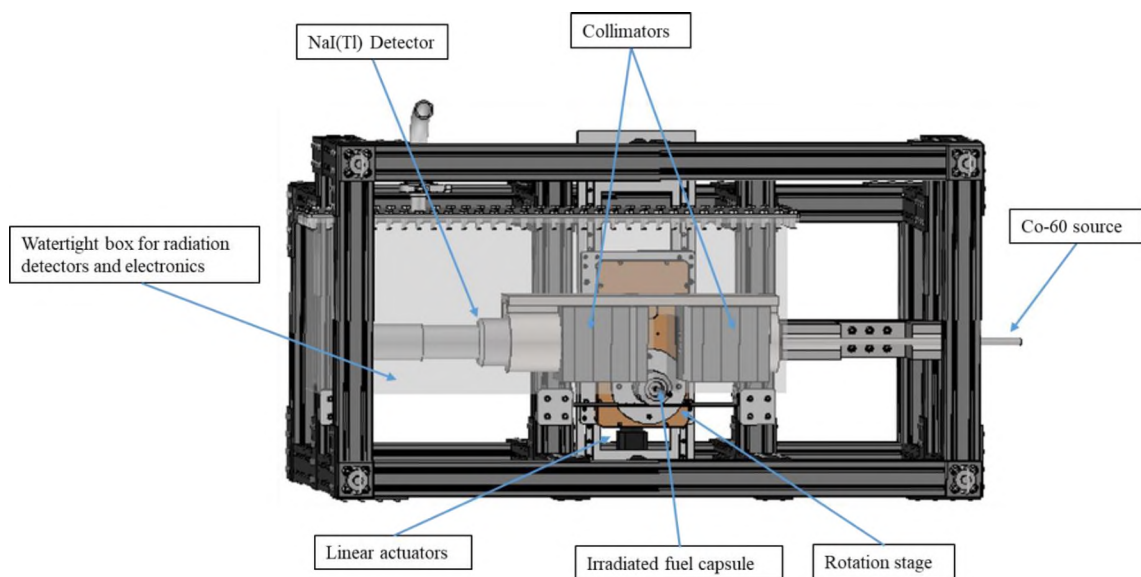
Figure 2.1: Finalized design for a submersible gamma tomography system

The design for an emission tomography system includes three key components, a source, a collimator, and a detector. A conceptual gamma emission tomography design consists of all three of those components with an additional interest on two types of collimators, pinhole collimators and parallel beam collimators.

2.1.1. Nuclear Fuel Capsule. The imaging object of this design is a capsule of nuclear fuel material that is currently undergoing testing to determine potential candidates for next generation fuel design. This system is designed specifically to handle INL designed capsules. These nuclear fuels are irradiated at the ATR at INL and are irradiated to varying burnup points. In order to image these capsules, the fuel is held by a chuck on rotation stage. The rotation stage will rotate the test fuel so the theta dimension can be

scanned completely. Once a 360- ° rotation is complete, the stage can move axially to acquire data along the z-axis of the fuel capsule. The stage also has the ability to travel in a linear direction to allow for the entire width of the fuel to be scanned, because the field of view of a parallel beam collimator is not the entire radial dimension of the nuclear fuel, and for a 3D image of the capsule one needs r, z, and θ have to be scanned in their entirety. For pinhole collimators, the nuclear fuel capsule only needs two degrees of motion, θ and z, as the diameter of the fuel is completely within the field of view defined by the pinhole itself.

2.1.2. Parallel Beam Collimator and LaBr$_3$(Ce) Scintillator. For the design of an emission tomography addition to the overall system, the design of the collimator is important. For the initial design process a parallel beam collimator was considered. The collimator was made primarily of tungsten, lead, and steel. The tungsten was utilized as an insert in an SS304 sleeve that was surrounded by lead. This can be seen in Figure 2.2.
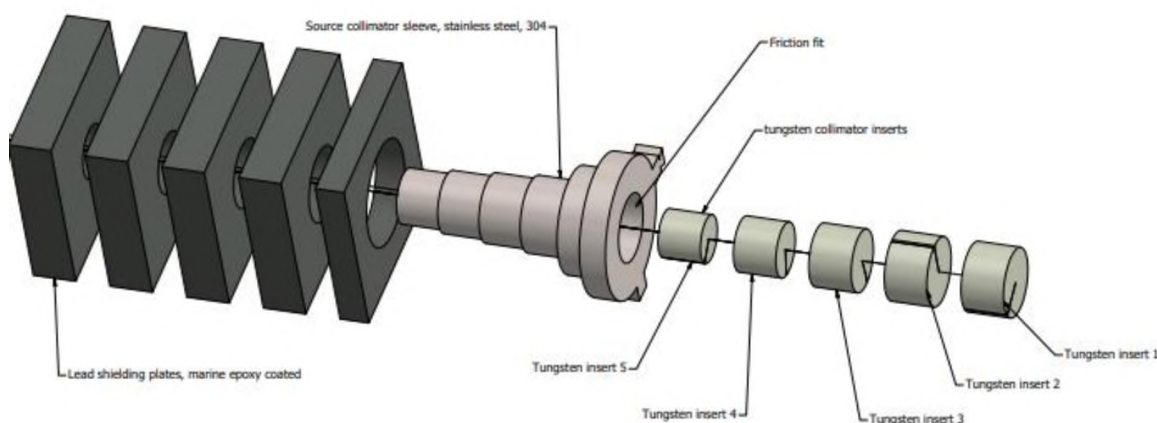
Figure 2.2: Diagram of the source side parallel beam collimator with lead shielding plates, a structural SS304 sleeve, and tungsten inserts

The lead shielding plates attenuate radiation streaming above and below the collimator tungsten inserts. The SS304 sleeve is used for a structural connector for each of the tungsten inserts. The tungsten inserts act as the primary radiation attenuation component between fuel and detector line-of-sight. The tungsten insert aperture is milled out using wire EDM to be 200 microns in diameter. As mentioned in Section 1.3.1 the spatial resolution of a parallel beam collimator will primarily be dependent upon the physical size of the aperture and the length of the overall collimator. The overall collimator length in this design is approximately 16.4 cm long. For the parallel beam collimator design, a $LaBr_3(Ce)$ detector is used for spectral acquisition. This detector type was chosen due to superior energy resolution (2.2-2.6% at 662 keV) over a detector such as an NaI (Tl) scintillator (7-8% at 662 keV). It also boasts a higher mass density over NaI (Tl) which results in higher detection efficiencies as more photons will interact within the medium. The only potential downside is the interference that arises from lanthanum [87]–[89]. It should be noted that for this parallel beam collimator, a monolithic $LaBr_3(Ce)$ is used to measure each projection. Since the resulting aperture is 200 microns, the projections are 200 micron slices of the nuclear fuel.

2.1.3. Pinhole Collimator and Pixelated CZT Detector. In addition to a parallel beam collimator, a pinhole collimator was also designed. Pinhole collimators allow for increased sampling due to an increase in field of view. This results in higher count rates at the expense of spatial resolution. The pinhole collimator design consists of tungsten as the attenuating material along with a 3 x 3 x 1.5 cm pixelated CZT detector with a pixel width of 2 mm. CZT was chosen due to ambient temperature operations combined with a pixelated array for data acquisition. A CAD model of the design is shown in Figure 2.3
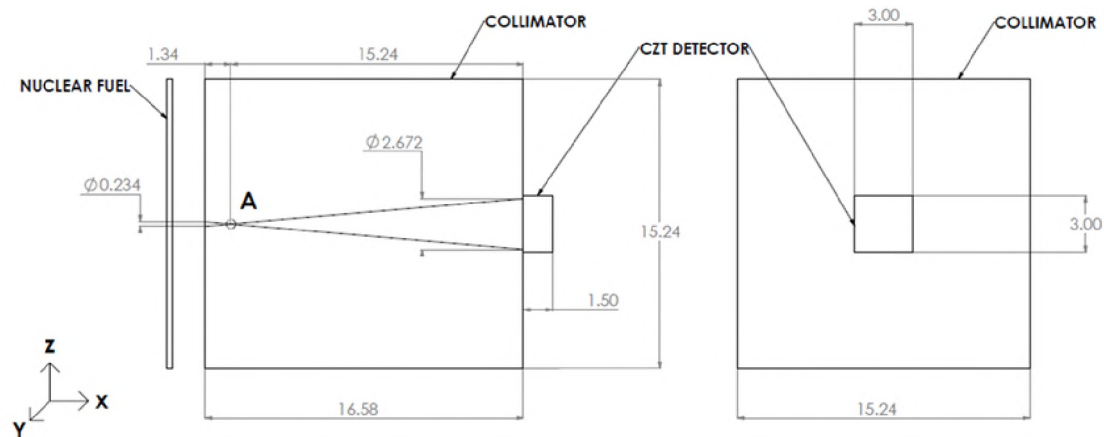
Figure 2.3: Pinhole collimator design combined with a CZT detector

For the design of the aperture, a 100-micron aperture diameter was selected along with a 5 ° acceptance angle. In this configuration, the radius of the field of view at the fuel capsule is approximately equal to its radius of nuclear fuel at 0.234 cm. The magnification factor that this design yields is 5.05. The only variable that is undetermined is the thickness of the CZT detector. Thicker detectors are more expensive, and therefore incident photon energy should determine the thickness of the detector. Higher energies will require thicker detector crystals to maximize the probability of interaction and to minimize and depth of interaction effects within the crystal.

2.2. MODELLING

Modelling the above systems is a necessity to further predict behavior and finalize a design. The primary choice for modelling the fuel behavior and radioisotope concentrations as a function of depletion is Oak Ridge Isotope Generator (ORIGEN) in the SCALE 6.2 package. ORIGEN is a deterministic depletion code that solves a series of energy averaged time dependent 1st order linear differential equations using the CRAM

matrix solver. The resulting solutions to these differential equations yield information regarding 174 actinides, 974 activation products, and 1149 fission products [90]. Due to the deterministic solvers within ORIGEN, the program provides information quickly.

The photon transport and detector response are modelled using Monte-Carlo N Paticle (MCNP) transport. This modelling software is a Monte Carlo transport program that enables users to stochastically transport particles with high degrees of accuracy over complex geometries, particle energy, and time [91]–[93]. MCNP also allows for the binning of particle data in tallies of user defined energies.

2.2.1. Fuel Source Term. To model the fuel source term, ORIGEN is used to provide an order of magnitude analysis on the potential fission products that exist within a given quantity of nuclear fuel. In order to utilize ORIGEN for a depletion calculation, a user must know about the power history of the reactor, enrichment of the fuel, and decay time of the reactor. In this case, the nuclear fuel of choice was a 17x17 Westinghouse PWR assembly enriched to 6% U-235; 6% is the upper limit on enrichment of these standard PWR reactor fuels. Since ORIGEN has the ability to perform fuel depletion on a per mass basis, the quantity of initial uranium concentration is not a concern as long it is normalized to a basis that is defined by the user. To account for the ATR power cycles, a 55-day uptime was used for the time component of the power history; this was selected due to it being the upper time limit for ATR operations. A power of 22.5 MW was chosen as the irradiation power. This represents a placeholder as the exact irradiation position was unknown. The ATR refuels and shuffles after 55 days of operation, and the reactor is down for approximately 22 days. Therefore, between each upcycle there is a 22-day delay period which ORIGEN will track and apply the proper Bateman equations to the concentrations

of products. At the end of each irradiation cycle ORIGEN tracks the quantity of depletion and records it. Through the use of a constant power and time, a user can calculate the amount of cycles needed to achieve a specific burnup. For the sake of these simulations, 18.5 GWd/MTU was chosen as it represents a middle ground between low burnup and high burnup conditions. Physically, high burnups require significantly more time in the ATR, and unlikely to be analyzed due to the time constraint.

Once the fuel has undergone depletion a representative gamma spectrum is needed as an input into a transport package. At the end of 18.5 GWd/MTU, a gamma spectrum is taken from 0-20 MeV with a bin width of 6.67 keV. These resulting spectra are normalized by dividing each bin by the total amount of photons that are generated. This yields a gamma emission rate probability. To correct for the activity difference between a full scale PWR assembly and a test capsule, the activity of the simulation is multiplied by the amount of material within the fuel capsule. This changes the activity from a basis dependent on a large system and transforms it to a basis dependent on the physical dimensions of the source capsule. The fuel gamma emission probability is then implemented into MCNP source definition with the appropriate dimensional sampling to provide information regarding the transport for both the parallel beam and pinhole collimators. The fuel dimensions are generated in surface cards and the volume is generated from those surface cards. This is the source definition that is utilized for both the Monte Carlo transport calculations for the parallel beam collimator, and the pinhole collimator. The focus of this is to generate an idea of potential count rates for the data acquisition systems.

Lastly, a model of a collimator with a pixelated CZT, in this case a pinhole collimator, needs to include a general phantom of a fission product to determine if the

signal can be seen in the detector pixel array. In this simulation, a localized sub-volume and a volumetrically uniform distribution is created to contain a fraction of overall activity of a specific radioisotope, in the case of the phantom, and a uniform activity distribution throughout the fuel. The end result of this is a 2D radiograph which is a singular input for an image reconstruction algorithm. The fuel phantom is then rotated to acquire multiple radiographic projections.

2.2.2. Parallel Beam Collimator Modelling Methodology. Using the source definition obtained from ORIGEN, MCNP can calculate the photon transport and the associated detector response. MCNP is a powerful radiation transport modelling program that relies upon stochastically transporting particles through user defined cells and media. MCNP simulates individual particles and records aspects of their average behavior in a tally [91]–[94]. The average behavior of particles within the system are inferred using the central limit theorem from the average simulated particle behavior. MCNP, unlike deterministic techniques, does not require any averaging in space, energy, and time. It has a high degree of fidelity in complex geometries and through all energy in which there are evaluated nuclear data libraries. Using a modified design of the parallel beam collimator, with a 200-micron collimator aperture shown in Figure 2.2, a geometry can be produced for the transport calculation. Since nuclear fuel emits radiation isotropically, it should be obvious to the reader that the probability of a photon with a given random 4π direction passing through a 200-micron diameter aperture is low. A visualization of this phenomenon is provided in Figure 2.4.
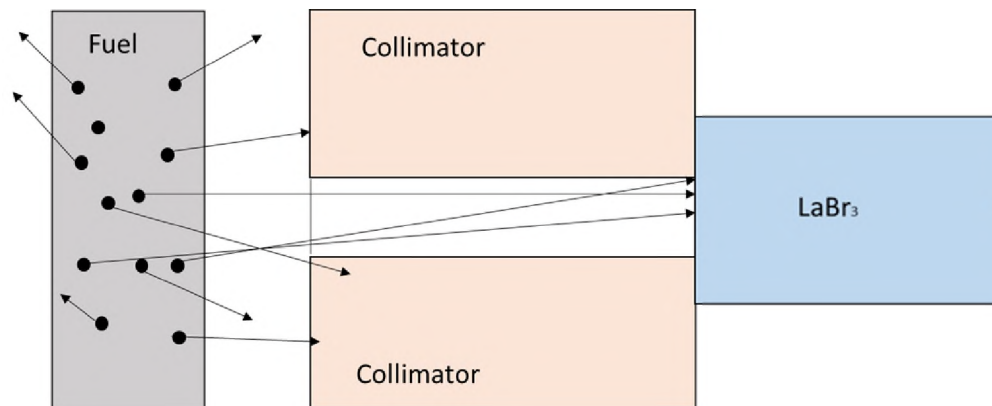
Figure 2.4: Isotropic photon emission from the nuclear fuel to the scintillator detector

MCNP, as a result, wastes computational resources tracking particles that will not contribute to the overall f8 detector response tally. Therefore, to increase the efficiency a different approach is necessary, and a monodirectional source biased method can be applied to increase the efficiency. Instead of having MCNP sample from an isotropic distribution, a monodirectional distribution can be forced. As a result, all of the particle within the fuel volume will be forced to go in a forward direction toward the detector. However, this would still result in many particles not contributing to the overall solution. Therefore, a sub-volume can be defined as the projection of the collimator aperture upon the nuclear fuel capsule. This shown in Figure 2.5. While this increases the number of particles that will impinge upon the detector, it is an unphysical system in the sense that particle do not behave this way. This means that a correction is needed to alter the simulation back to being isotropic. A series of geometric and solid angle semi-analytic factors can be applied to the detector response tally to achieve this end [95]. This is the focus of Paper 1.
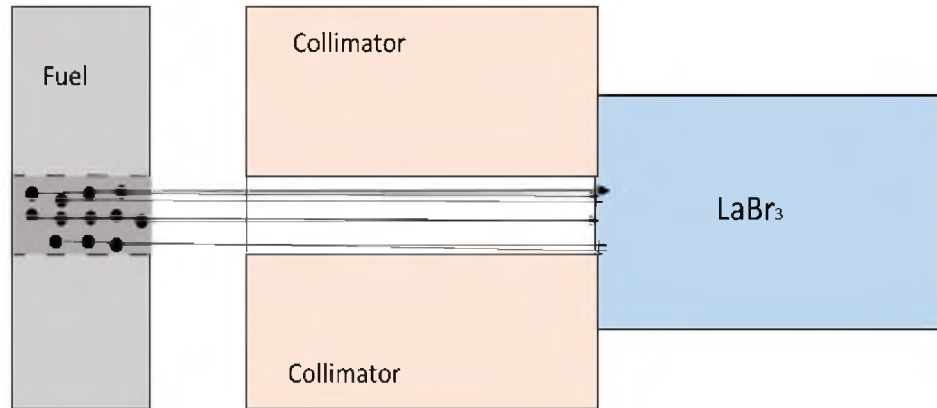
Figure 2.5: Monodirectionally biased beam of photons through the collimator aperture toward the scintillator detector

The semi-analytic models are compared with other acceleration techniques applicable for f8 detector response tallies within MCNP, and that is the focus of Paper 2 [92]–[94], [96]–[98].

2.2.3. Pinhole Collimator with Pixelated CZT Modeling Methodology. In this design, a pinhole collimator is used in conjunction with a pixelated CZT detector outlined in 2.1.3. The objective in this instance is to determine spatial resolution for this system design, and an idea of the increase in count rates that arises from the increased field of view. MCNP is used again for the transport of photons to the pixelated detector, and the simulation is just a standard isotropic run with no variance reduction methodologies. An f8 detector response tally is applied over the entirety of the medium to determine a count rate to compare to the results in Paper 1. To model a pinhole collimator within MCNP, a series of cones is used to define the aperture diameter and acceptance angle. In this case those parameters are 100 micron and 5 °, respectively. The results of this simulation study are presented in Paper 3.

The modelling of the fuel phantom or volumetrically uniform radioisotope distribution mentioned in 2.2 utilizes the same pinhole collimator and detector system that sampled the photon spectrum. For this model there are parameters that are needed. First, a phantom of a localized sub-volume or uniform distribution is required. Two, a model of a pixelated detector array for tally data is needed to generate a per pixel response. This manifests itself as an f4 mesh tally. While f4 cell flux tallies are not detector response tallies, an approximation of photon population can be determined. Third, a prediction of activity density is needed to determine if a phantom can be distinguished from the overall activity within the entire fuel volume. Both a uniform Eu-154 distribution and a localized activity of Cs-137 are modelled and the phantom is shown in Figure 2.6.
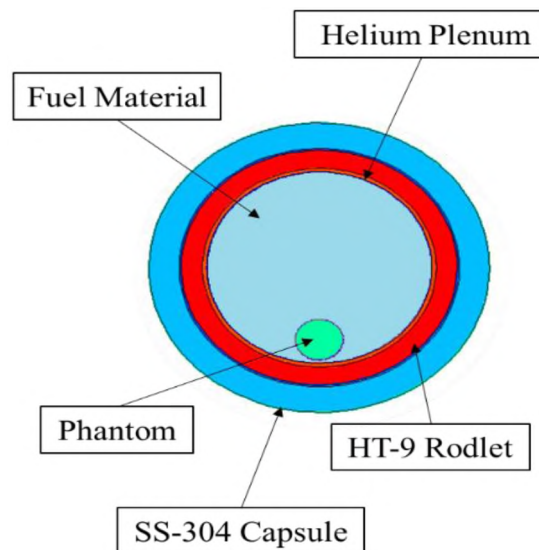
Figure 2.6: Nuclear fuel capsule with a Cs-137 phantom at a 0 ° rotation. 0 ° represents the furthest point within direct line of sight to the detector

The preliminary results on the radiographic projections of the Cs-137 phantom are shown in Section 3 of this dissertation. The Eu-154 distribution is used as a check to

determine if a line scan of central pixels shows a semicircular distribution and to check if there are variations along a row of pixels. The line scans are also shown in Section 3 of this dissertation.

PAPER

I. A SOURCE BIASING AND VARIANCE REDUCTION TECHNIQUE FOR MONTE CARLO RADIATION TRANSPORT MODELING OF EMISSION TOMOGRAPHY PROBLEMS

Seth Kilby[1], Zhongmin Jin[1], Ashish Avachat[1], Bryant Kanies[1], Nicholas Woolstenhulme[2], Hyoung K. Lee[1], Joseph Graham[1]

[1]Missouri University of Science and Technology 301 W 14th St. Rolla, MO 65409
[2]Idaho National Laboratory 1955 N. Fremont Avenue Idaho Falls, ID 83415

ABSTRACT

A numerical radiation transport methodology for predicting gamma emission tomographs was developed utilizing the deterministic fuel burn-up software ORIGEN in the SCALE code package as source definition input for Monte Carlo N Particle Transport ver. 6.1 to simulate gamma emission spectra from irradiated nuclear fuel and measured by an inorganic scintillator detector. Variance reduction utilized analytical expressions for the solid angle and field of view between source, collimator, and detector to normalize the gamma energy spectrum from a non-analog monodirectionally biased beam source problem to approximate the equivalent analog problem of an isotropic source. One normalization scheme, which assumes that the source is distributed in a thin cylindrical volume can achieve lower than 20% error and an order of 10^7 reduction in the computational cost. A different normalization scheme involving a truncated cone source distribution overestimated the count rate by approximately 45% but had similar computational savings. In both approaches, the accuracy and computational savings of the

method improves with increasing collimator aspect ratio. This method is therefore useful for problems with high aspect ratio collimators.

1. INTRODUCTION

As more advanced nuclear fuels are developed, it is necessary to learn how the fuel behaves in a reactor environment. Knowledge of both chemical and physical changes, such as fission product migration, cracking, and defect formation, is key in qualifying test fuels for future adoption in power reactors. Driven by the need for non-destructive pool-side characterization capabilities that provide both chemical and physical information of various next generation fuels, radiography and tomography represent an important class of experimental techniques. Since this manuscript pertains specifically to pool-side characterization, we look at the situation where water will be surrounding the entire system including the imaging object, irradiated nuclear fuel. Given the high density of nuclear fuel and presence of water between object and detector in this particular imaging problem, one can compare the relative advantages and disadvantages of X-ray, neutron and gamma tomography and radiography. While X-ray emission tomography can provide a wealth of chemical information from a radioactive material, dense nuclear fuel exhibits strong mass attenuation at characteristic X-ray energies in the range of 30 keV to 100 keV. Large mass attenuation coefficients on the order of 10^2-10^{-1} cm^2 g^{-1} [1] preclude observation of the internal fuel structure, even in small volume fuel specimens. Neutrons, on the other hand, can be highly penetrating and therefore well suited for interrogating dense materials. However, given that water – a strong neutron scatterer – surrounds the imaging object in

this particular instance, an initially clear radiographic projection would be quickly scattered by water. This would yield tomographs with low signal-to-noise ratios which would result in noise and poor spatial resolution in the resulting reconstructed tomographs. Gamma tomography utilizes inherently higher photon energies than X-ray tomography. The mass attenuation coefficient in water is up to two orders of magnitude lower at photon energies between 500 keV and 2 MeV [1] permitting observation of the internal fuel structure with greater ease. Additionally, the scattering and mass attenuation effects of gammas in water are small compared to X-rays and neutrons.

In recent years, as a byproduct of the ever increasing interest in nonproliferation related technology, gamma emission tomography has piqued the interest of researchers. Previous experiments have employed emission gamma tomography to detect partial defects in nuclear fuel assemblies [2-7]. In tomography measurements conducted at the Forsmark Nuclear Power Plant in Forsmark, Sweden, Ba-140 was used to construct a tomographic image with 10,200 detector positions. Image processing included background noise subtraction to minimize the effect of unwanted gammas [8]. In experiments at the Halden Research Reactor in Halden, Norway, which had a similar scanning geometry to the proposed design presented in this manuscript, the authors mapped fission products such as Cs-137 and Ba/La-140 in the reactor fuel [9-10].

The present study looks at a design for a tomography system to be installed in the fuel canal of the Advanced Test Reactor (ATR) at Idaho National Laboratory. The design requirements for the system differ from experiments at Forsmark and Halden in several important respects. The ATR test fuel capsules are centimeters in scale and thus their activity is significantly lower than the activity available in full fuel assemblies. The lower

activity of the test fuel makes the use of semiconductor detectors time consuming compared to scintillator detectors. Semiconductor detectors used in gamma spectroscopy have low efficiencies, requiring longer acquisition times compared to inorganic scintillators. Cost is another limiting factor. Inorganic scintillators offer greater efficiencies at the cost of poorer energy resolution. $LaBr_3(Ce)$ scintillators, which offer about twice the resolution and 1.3 times the efficiency of a NaI detector [11], represent a reasonable compromise between efficiency, cost, and resolution.

Another major difference is that the present design requires a collimator aperture on the order of microns to achieve an order of 10^2 microns spatial resolution whereas the tomography experiments at Forsmark and Halden had millimeter resolution. Moreover, the Halden experiments used a Beer-Lambert ray tracer approximation in the construction of images, and only focused on imaging isotopes with high gamma energies because of the attenuation effect through the fuel.

In the present design, with its small solid angles and strongly attenuating materials, variance reduction becomes an important consideration, especially if one wants to simulate entire radiographic projection and tomographs. Techniques like Russian roulette, geometry splitting, energy splitting, implicit absorption and weight windowing are frequently used in photon transport calculations to good effect as are those detailed in [12]. For the purposes of calculating the intensity under a photopeak in a gamma spectroscopy problem, Russian roulette, geometry splitting, energy splitting, implicit absorption and weight windowing – techniques which mainly reduce the variance from absorption and scattering interactions but not from uncollided particles – are of marginal benefit. In this particular incidence, it is the uncollided photons and, to a lesser extent, low angle scattered photons that contribute

to the tallies in the energy range of interest. Compton scattering is an important feature in gamma spectra of course, but for high aspect ratio collimator problems, it is primarily the Compton scattering in the detector that contributes to the spectrum. Source biasing is a more powerful variance reduction technique in this instance. The proposed technique in this work essentially combines directional source biasing with volumetric source biasing and an analytical expression of the particle weight at the detector to reduce the variance. A characteristic sub-volume of the source is forward biased so that the majority of photons are "aimed" at the scintillator detector. Analytical factors are used to normalize tally values to match the equivalent full-volume, isotropic source problem (i.e. the analog problem). The work presented here examines only the source biasing and normalization/weighting methods. These methods, however, are not incompatible with other variance reduction strategies such as geometry splitting, Russian roulette, or implicit absorption. For problems involving larger mass thicknesses or wider collimators, source biasing might be combined with other variance reduction techniques to reduce the computational time.

2. METHODOLOGY

To model the gamma source used in radiation transport simulations (i.e. the fuel capsule), fuel burnup and the resulting fission product spectra were simulated. This was done by using the fuel burnup and depletion code, ORIGEN in the SCALE 6.2 package, and will be referred to as ORIGEN throughout the rest of the paper [13]. This calculated the concentration of fission products and respective gamma spectra. For this calculation, a 17×17 pressurized water reactor (PWR) fuel library was used with U-235 enriched to 6%.

This was chosen due to the comparability to standard power reactor enrichment as the goal was to acquire a same order of magnitude analysis only. The fuel geometry, neutron flux spectra and typical power histories at ATR are different, hence not entirely reliable for calculating burnup in fuel irradiated in the ATR without a dedicated reactor library. However, it should be stressed here that accurate prediction of irradiation fuel spectra is not the end goal of the present work. The burnup calculations were merely used to produce typical fission product yields in a thermal flux reactor and generate strong photopeak activities correct within an order-of-magnitude. The fuel was subjected to irradiation cycles of 55 days at 22.5 MW, and decay times of 22 days between irradiation cycles. For the model, the selected burnup was set at 18.50 GWd. Since fission product creation is asymptotic, any burnup selected after 18.50 GWd was found to have diminishing returns in terms of available photopeak activity for a given irradiation time. In addition to activity data, ORIGEN also calculates gamma spectra, and each ORIGEN entry was divided by the total gamma intensity to achieve a probability of emission. To achieve this, the gamma spectrum was binned from 0 MeV to 20 MeV with 3000 energy bins spaced 6.67 keV apart. Given the many thousands of emission lines from hundreds of fission products, the use of the ORIGEN gamma spectrum output was determined to be the most straightforward way to incorporate the irradiated fuel emission spectrum in the MCNP 6.1 source definition. In principle, it is also possible to parse the ORIGEN output and multiply each radionuclide activity by its branching ratios and gamma intensities to define a truly discrete (as opposed to energy binned) gamma spectrum. Another option is to parse the ORIGEN output for radionuclide concentrations and employ Evaluated Nuclear Structure Data Files to simulate the process of radioactive decay within MCNP 6.1. These later approaches, though

arguably more physically accurate, come at a higher computational cost and are not justified given the objectives of the present work. They should, however, be considered for simulations where accurate recreation of real spectra is sought.

The burnup calculations were performed on a per metric ton uranium (MTU) basis. Activities were multiplied by the fraction of a metric ton within the test fuel. By doing this, a per test fuel basis was achieved. MCNP 6.1 [14] was then utilized to model the radiation transport of the irradiated fuel in the tomography system.
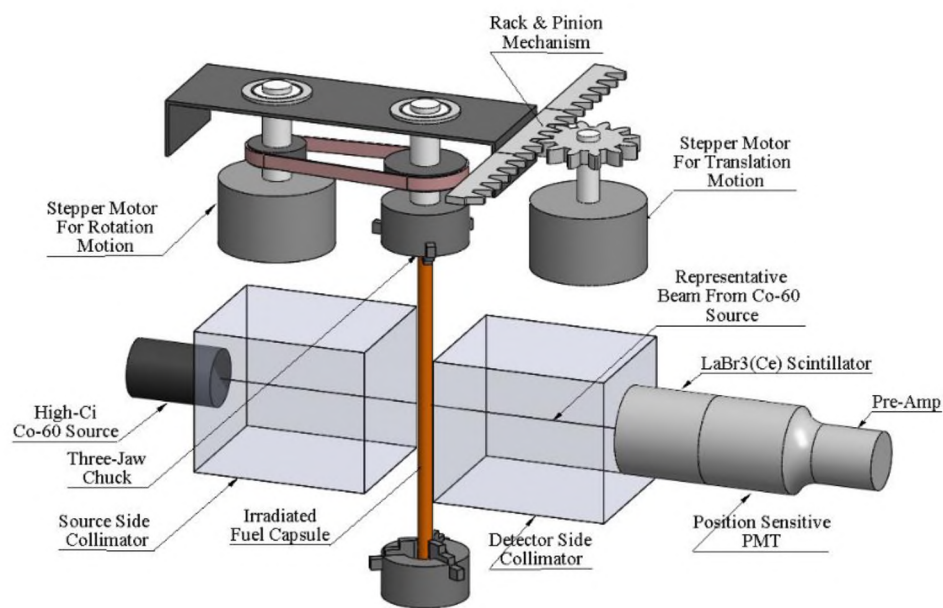
Figure 1: CAD model of the gamma tomography system

Figure 1 shows a conceptual layout of the tomography system. It comprises two tungsten collimators, a Co-60 source, a fuel capsule, and a $LaBr_3(Ce)$ detector box and the corresponding mechanical drive components. Though not the focus of this manuscript, the

Co-60 source is used for simultaneous transmission computed tomography. An MCNP 6.1

model was developed based on the design in Figure 1 excluding the mechanical drive

components. The collimator aperture width was set to 1 mm for the purpose of testing the

variance reduction techniques. Setting the collimator aperture to 0.1 mm with an isotropic

source proved to be more computationally demanding than necessary to demonstrate the

validity of the variance reduction techniques. Based on the burnup calculations described,

a source definition was added to the MCNP 6.1 model to define the gamma source within

the fuel. To model the gammas being emitted from the fuel, a source definition card (SDEF)

was utilized. The SDEF card uses discrete energies from 0-2 MeV in 20 keV increments,

and probabilities of emission directly calculated from the ORIGEN output files. Depending

on the type of photon transport calculation being performed, the source angular distribution

was either treated as spherically uniform (i.e. isotropic) and distributed uniformly across

the volume of the fuel material or in the non-analog simulations, treated as a

monodirectional beam directed towards the detector along the collimator axis with source

uniformly distributed in a sub-volume of the fuel. The sub-volume, defined below, falls

within the detector's field of view, roughly speaking. A photon physics model was included

and electron transport was turned off. MCNP 6.1 stores information about the production

of secondary electrons but does not transport them as it is a computationally expensive

process not needed for this problem [14]. A pulse height (F8) tally was then used to

generate a representative gamma spectrum in the detector scintillator volume (cell filled

with $LaBr_3(Ce)$.

When utilizing a small collimator aperture, radiation transport is inherently

inefficient, owing to the small field of view seen by the detector. This is further exacerbated

by the isotropic nature of the source and small detector solid angle. Most of the particles are lost in the sense that they travel away from the detector or interact with the collimator. A way to counteract that is to utilize variance reduction techniques. In this system, three main techniques were used for the full isotropic case. One, a Russian roulette technique was used to end the tracking of particles that go in the opposite direction of the $LaBr_3(Ce)$ detector. Importance manipulation was also utilized to reject any photons that interacted with the tungsten collimator. Photons entering the thick collimator are virtually guaranteed to be absorbed, thus tracking them is wasted computational effort. Importance manipulation and Russian rouletting were used to accelerate the computational speed in the isotropic simulations but they have little additional bearing on the discussion that follows.

In a second set of simulations, the source particles were sampled from a characteristic volume, a sub-volume of the fuel capsule defined as the intersection of the outer cylindrical surface of the fuel capsule and the inner cylindrical surface of the collimator. This was combined with directional source biasing. A monodirectional source definition was used with a direction vector parallel to the collimator axis towards the detector cell. In other words, the source photons were aimed towards the detector. Used together, these two techniques force all uncollided source particles to be deposited in the detector. This approach does, however, overestimate the count rate by orders of magnitude, especially as the collimator aspect ratio increases. Therefore, particle weight correction factors are required to account for both the volume and solid angle departures from the full volume, isotropic case. Assuming that the gamma ray source is distributed in a volume defined by the intersection of the cylindrical fuel capsule and a cylindrical surface

extending from the inner wall of the collimator, the characteristic volume correction factor

is approximated by a ratio of volumes

$$F_{v,cyl} = \frac{V_{char,cyl}}{V_{fuel}} \tag{1}$$

where $V_{char,cyl}$ is the volume of the characteristic cylinder within the fuel, and V_{fuel} is the

volume of the total fuel element. By substituting the volumes into Equation 1, $F_{v,cyl}$ is

simplified in Equations 2-4

$$F_{v,cyl} = \frac{\pi r_1^2 h}{\pi R^2 H} = \frac{2\pi r_1^2}{\pi R H} \tag{2}$$

$$F_{v,cyl} = \frac{2r_1^2}{RH} \tag{3}$$

r_1 is the radius of the characteristic volume which is also the radius of the collimator

aperture shown in Figure 2, $h = 2R$ is the length of the sub-volume cylinder, R is the radius

of the test fuel, and H is the height of the test fuel. However, it should be noted that

Equations 2 and 3 underestimate the volume that the collimator aperture sees. A somewhat

better approximation is obtained by including two hemispherical caps on each end of the

cylinder. These caps approximate the gap between the characteristic volume and the fuel

capsule. The total cylindrical volume factor is then given by

$$F_{v,cyl} = \frac{2r_1^2}{RH} + \frac{4r_1^3}{3R^2 H} \tag{4}$$

This factor only represents one approximation of the field of view. If one considers

the divergence solid angle subtended by the finite diameter collimator one arrives at a

truncated cone. The volume factor for a truncated cone is derived in Equations 5-7 and

Figure 2.

$$F_{v,truncated\ cone} = \frac{V_{char,truncated\ cone}}{V_{fuel}} \tag{5}$$

$$F_{v,truncated\ cone} = \frac{\frac{\pi}{3}(r_3^2 x_3) - \frac{\pi}{3}(r_2^2 x_2)}{\pi R^2 H} \tag{6}$$

$$F_{v,cone} = \frac{(r_3{}^2 x_3) - (r_2{}^2 x_2)}{3R^2 H} \tag{7}$$

r_3 is the radius of the truncated cone's larger base, and r_2 is the radius of the smaller base.

x_3 is the distance from r_3 to the center of the collimator aperture, and x_2 is the distance

from r_2 to the center of the collimator aperture.
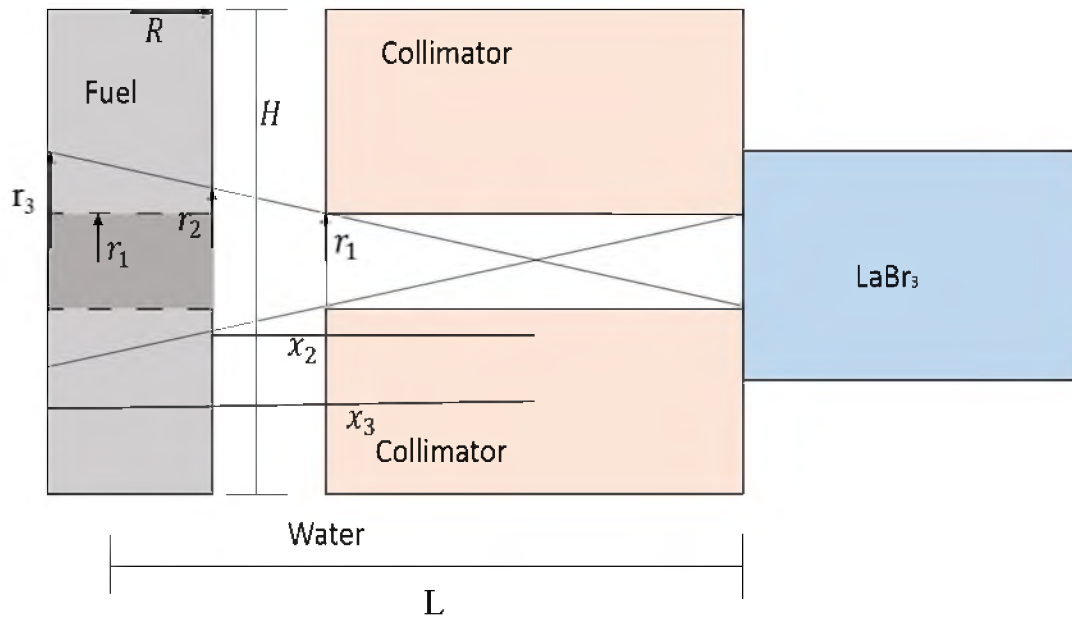
Figure 2: Geometry factor visualization (not drawn to scale)

To correct for the solid angle effects, one can start with a point source

approximation as derived in Equations 8-9

$$F_\Omega = \frac{\text{aperature area}}{\text{area of sphere at detector}} = \frac{\pi r_1^2}{4\pi L^2} \tag{8}$$

$$F_\Omega = \frac{r_1^2}{4L^2} \tag{9}$$

where L is the length from the center of the test fuel to the surface of the detector. The volume and solid angle factors are multiplied together with the activity of the test fuel from ORIGEN as shown in Equation 10.

$$\text{Corrected Activity} \cong A_{Test\ Fuel}(F_v \times F_\Omega) \tag{10}$$

where $A_{Test\ Fuel}$ is the activity of the fuel element calculated by normalizing the ORIGEN activity in Table 1 for a per capsule basis and F_v is either the cylindrical or truncated cone volume factor. Equation 10 is the correction from a monodirectional biased source to an isotropic source, and this value is multiplied with every bin of an F8 tally. Utilizing this variance reduction technique allows the one to run a non-analog simulation at approximately a factor $F_v \times F_\Omega$ faster. It should be mentioned that the solid angle correction factor of Equation 9 assumes that all points in the characteristic volume contribute about the same amount of solid angle to the corrected activity. This is approximately true in the case of a large collimator aspect ratio. For small aspect ratios, the two geometric factors will overestimate the count rates of the photopeaks. As the aspect ratio increases, the geometric factors converge to a degenerate cylinder. In principle, one could numerically integrate the solid angle over the fuel volume to achieve an even more accurate normalization factor but the simple analytical form of these equations and their clear relation to the problem geometry is clearly advantageous.

A measure of the computational savings of this variance reduction technique can be derived from the variance of the data within the MCNP 6.1 tallies. The counting statistics in each of the energy bins in the pulse-height tally follows Poisson statistics,

meaning that the mean number of counts within the tally bin, μ, is equal to its variance. Taking the number of counts as the sample estimate of the mean and considering that the mean should be proportional to the number of particle histories for an unchanging geometry, a figure of merit can be derived which describes the reduction of variance per particle history. A proportionality factor, f_m, relates the mean to the number of particle histories, N_m. This can be seen in Equation 11.

$$\mu \approx f_m N_m \qquad (11)$$

The subscript, m, denotes the method (i.e. source and problem geometry). In a Poisson process, the mean is equal to the variance (σ^2) so Equation 11 can be simplified into Equation 12

$$f_{\mathrm{m}} \approx \frac{\sigma_m^2}{N_m} \qquad (12)$$

To incorporate the fractional error associated with an MCNP 6.1 tally, the fractional error in a bin with c_m counts can be expressed as Equation 13

$$\epsilon_m = \frac{\sigma_m}{c_m} \approx \frac{1}{\sqrt{c_m}} \approx \frac{1}{\sqrt{f_m N_m}} \qquad (13)$$

If $N_1{}^*$ and $N_2{}^*$ are the minimum number of histories required to reduce the tally fractional error below, ϵ, for methods 1 and 2, respectively, then the computational savings, S, can be defined as Equation 14

$$S = \frac{N_2^*}{N_1^*} \approx \frac{N_2 \sigma_1^2}{N_1 \sigma_2^2} \qquad (14)$$

where pairs of N_m and σ_{m}^2 are the number of histories and bin variances for a given pair of simulations and for a given tally bin.

3. RESULTS AND DISCUSSION

Using ORIGEN, a gamma spectrum for a 1 MTU 17×17 PWR fuel assembly was produced to give an order of magnitude analysis. Three test cases are described in Table 1.

Table 1: ORIGEN Burnup Data

	60 Day Decay		
Burnup (GWd/MTU)	0.50	18.50	49.50
Decay Time (Days)	60.00	60.00	60.00
Activity/MTU (Ci/MTU)	1.00×10^6	4.56×10^6	5.33×10^6
Activity (Ci)	8.84	40.17	46.82

A 60 day decay time was utilized as it represents a relatively long decay time (and hence moderate count rate) for the tomography system's intended use. As mentioned previously, 18.50 GWd MTU^{-1} was the selected case for initial modelling. The un-normalized activity was used with Equation 5 to calculate the corrected activity for the monodirectional biased source definition. For this calculation, 40.17 Ci was used.

For the burnup case above, a spectrum was generated using MCNP 6.1 with a monodirectional biased source term corrected with the cylindrical geometric factor with the hemispherical caps and the solid angle correction factor, and the detector response generated from MCNP 6.1 is seen in Figure 3.
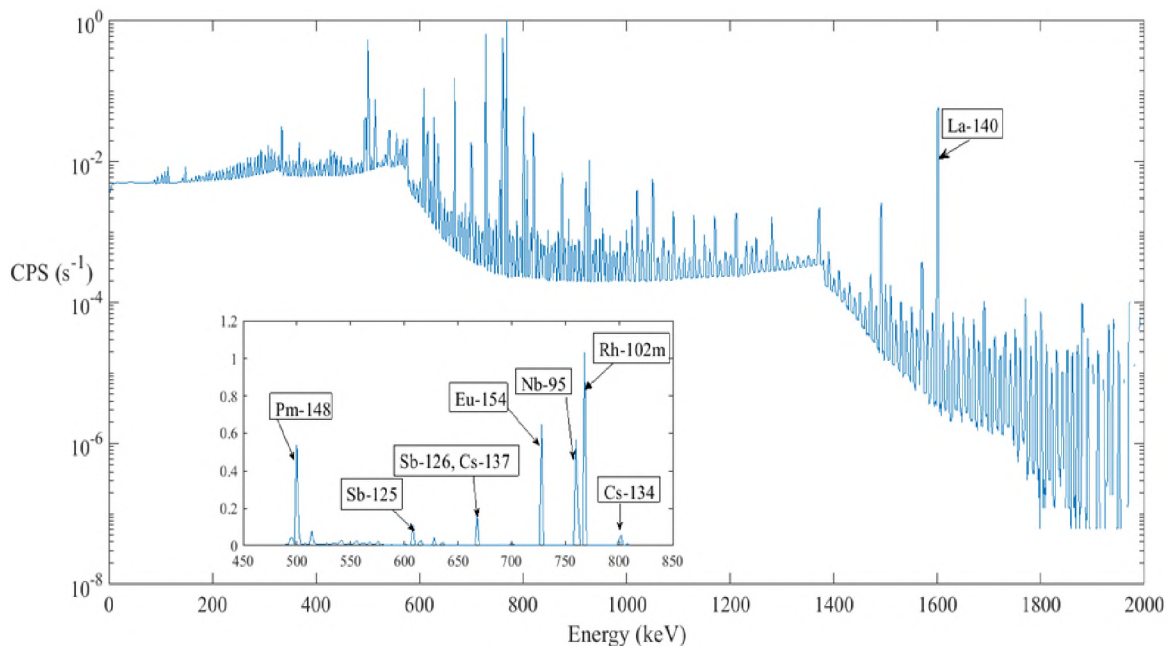
Figure 3: MCNP 6.1 pulse-height tally in the scintillator crystal of the gamma detector

The spectrum generated shows that out of the hundreds of fission products created, there are only 8-9 with photopeak intensities great enough to be practical for emission tomography in the present enrichment, burnup and decay conditions. As seen in Figure 3, the count rates are on the order of single digits. This implies that a pencil-beam-like collimator with the given geometry is probably too narrow to provide fuel emission tomographs with reasonable acquisition speed for the burnup considered. The per-photopeak count rate must be on the order of hundreds of counts per second in order to achieve a tolerable signal-to-noise ratio and to be able to acquire enough projections to reconstruct a detailed 3D tomograph in a period of days. Furthermore, $LaBr_3(Ce)$ detectors have an intrinsic lanthanum activity associated with them that would create comparably intense interference peaks in this spectrum [15]. Another important component of this spectrum that needs to be considered is that, since the source term is monodirectional, the

X-rays below 100 keV, principally from gamma-induced X-ray fluorescence of the fuel, are less frequently generated by randomly scattered or emitted gamma rays. This means that the characteristic X-rays in this spectrum are artificially lower than otherwise expected in an actual experiment. X-rays are not the focus of this work, but this difference needs to be mentioned should one try to apply this variance reduction technique to an X-ray fluorescence problem.

4. VERIFICATION OF VARIANCE REDUCTION

To verify whether the derived correction factors applied to a monodirectional case are quantitatively accurate in approximating the isotropic case, ratios of the photopeak areas for each method are compared. A ratio of the normalized monodirectional counts to the isotropic counts for the strongest seven photopeaks were graphed over the energy. The closer the values to unity, the better the accuracy of the approximation. These ratios can be seen in Figure 4. The cylindrical volume correction factor with the point source solid angle factor yields results that overestimate the count rates by about 18% for the 1 mm radius collimator, on average. Over 99% of the uncertainty in the ratio is propagated from the isotropic tally. The truncated cone factor results in about 45% excess counts for 1 mm. The same variance reduction technique applied to the 0.1 mm radius specified in the actual collimator design, would, presumably, improve the accuracy of the predictions. Nevertheless, the magnitude of agreement shown in Figure 4, is justified in applications where computational speed takes greater preference over accuracy such as this one where the burnup calculations only offer order of magnitude estimates of the real conditions
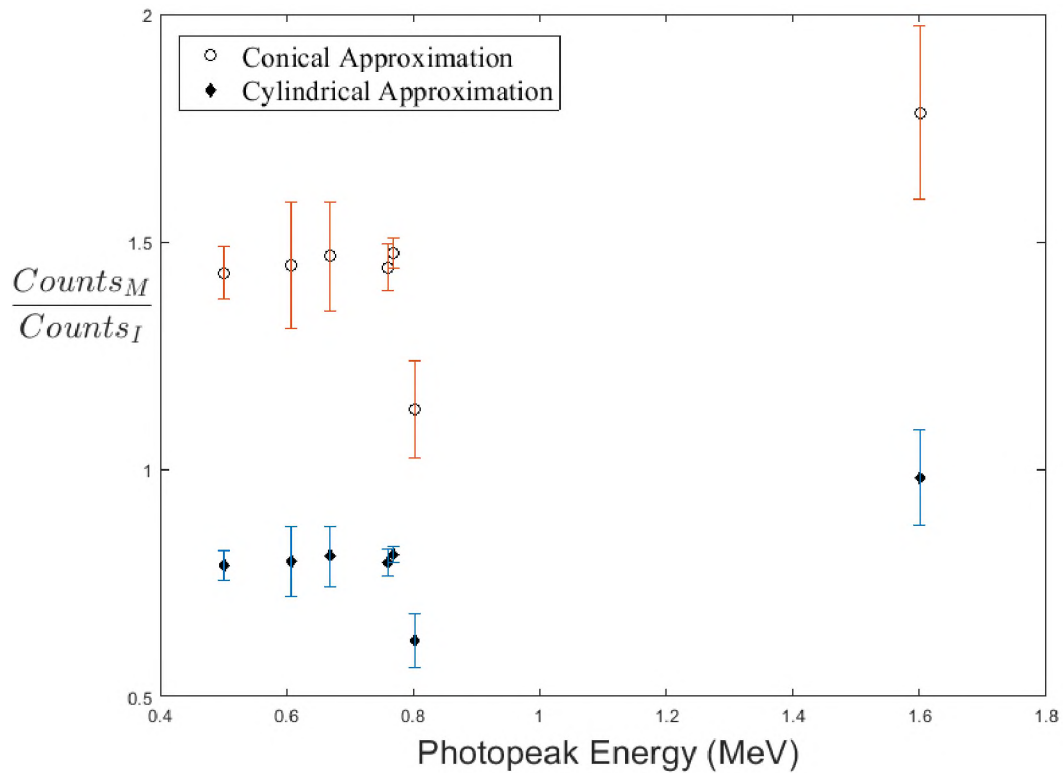
Figure 4: Ratio of the photopeak areas for each transport method for seven high intensity photopeaks at their corresponding decay energies. The ratios are calculated using both the truncated cone normalization and the cylindrical normalization for a 1 mm aperture collimator

In both geometric cases, the solid angle factor assumes a point source and is not a true volume average of all solid angles within the sampling volume. Therefore, the solid angle correction factor overestimates the volume averaged solid angle. As the collimator aperture decreases, the aspect ratio increases which will cause the volume correction factor to tend towards a cylindrical sampling and limit the solid angle variations. To model the effect that the aspect ratio has on the system, MCNP 6.1 simulations of both isotropic and monodirectional sources were carried out for collimator radii of: 1 mm, 3 mm, 5 mm, and 10 mm. The values of the ratios are plotted in Figure 5.
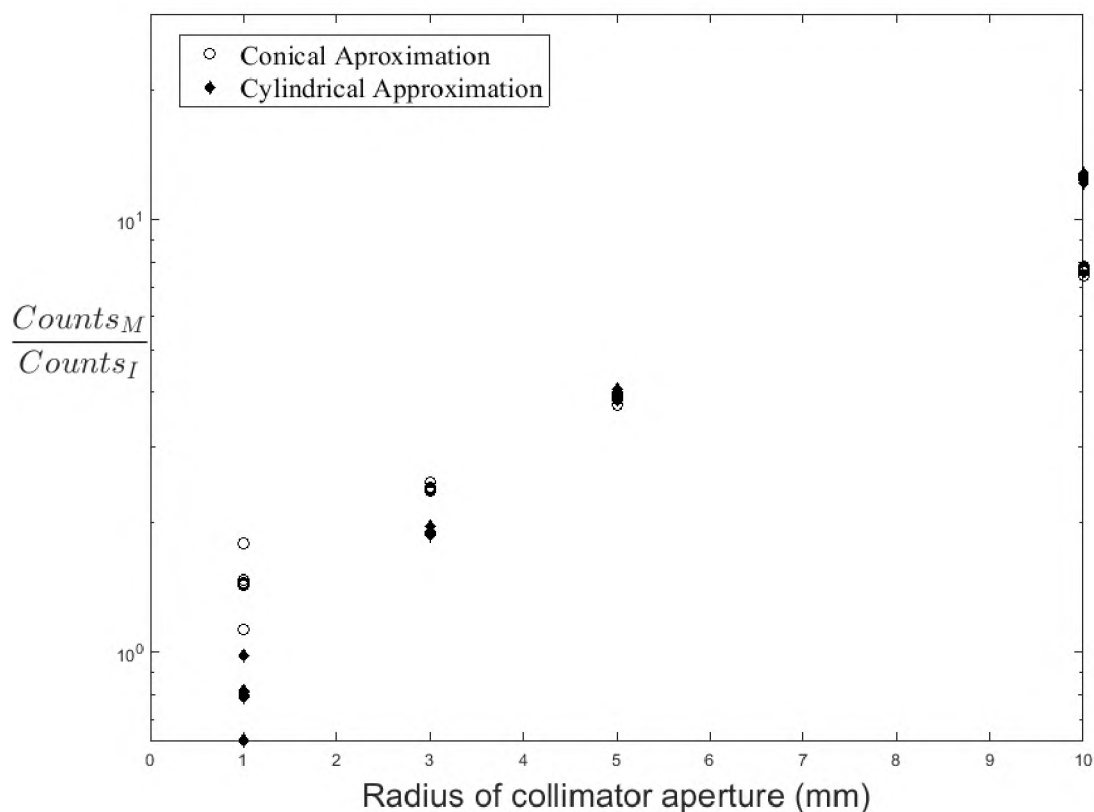
Figure 5: Comparison between of isotropic and monodirectionally biased (post normalization) count rates as a function of aperture radii. Each data marker indicates a photopeak. Ratios for the seven strong photopeaks are shown in each cluster

This relationship shows that as beam size or collimator aperture decrease, the correction factors improve in accuracy. While the photopeak ratios show little dispersion over energy, their magnitude suffers as the collimator radius increases. This figure also shows that the truncated cone correction factor better approximates the count rate than the cylindrical correction factor in most cases. At smaller radii, the two correction factors are comparable. Most of the dispersion in the ratios at 1 mm is caused by the large relative error in the isotropic tally which gets propagated into the ratio. Even so, the cylindrical approximation is accurate to less than 20% at 1 mm, on average and can be expected to

converge to unity as the radius in decreased further. The computational savings can be observed in Figure 6.
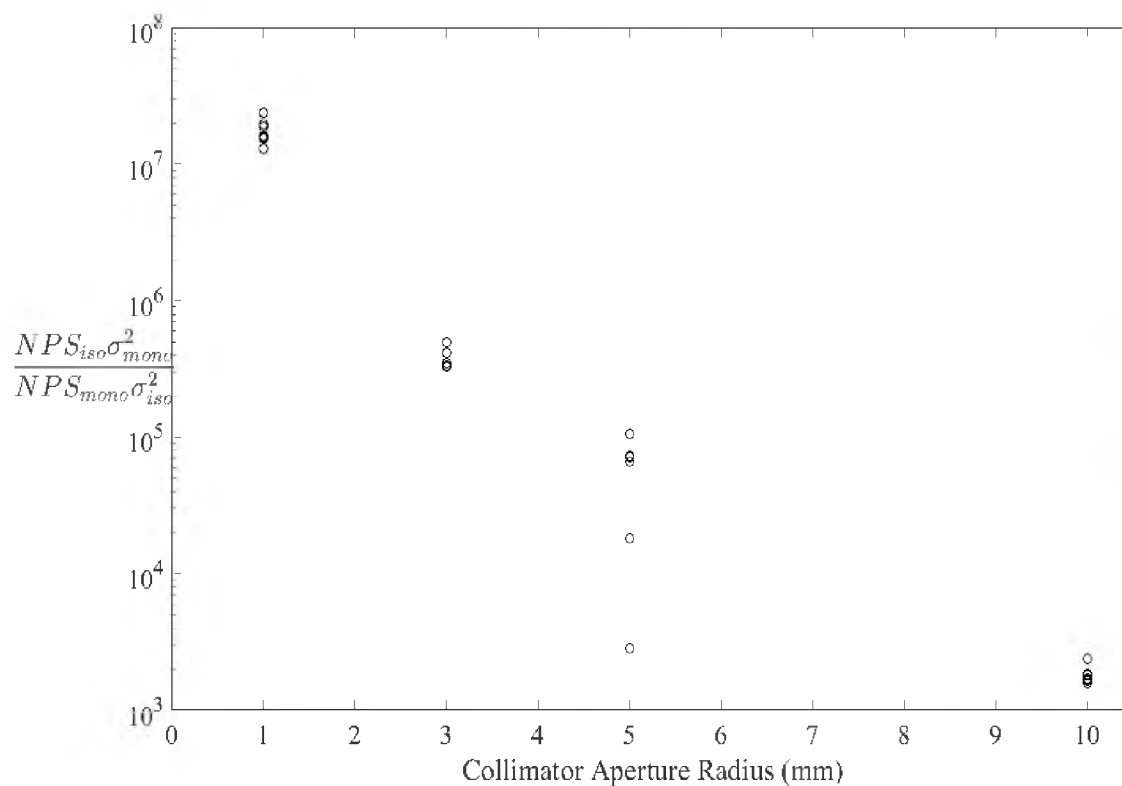
Figure 6: Computational savings of all photopeaks at various collimator aperture radii

The general trend for the data is that as the collimator aperture radius decreases the computational savings increase exponentially. The computational savings for a 1 mm aperture is on the order of more than 10^7 meaning that a monodirectional calculation can achieve the same relative error as an isotropic case in over ten million times fewer particles histories. Given the tolerable systematic error (18%) this incurs it is still a major advance over the fully analog case. When the radius is increased to 10 mm, the computational savings are on the order of 10^3. While this may be useful in simulations where only

qualitative spectral information or order of magnitude estimates are sought, the error is significantly increase, as seen in Figure 5. Thus the power of this variance reduction technique is reserved to a particular class of problem geometries where a high aspect ratio collimator is used but in those problems the method works to good effect.

The sources of error can be summarized as follows. The systematic error in the variance reduction technique comes from the use of directional and volumetric source biasing as well as the solid angle and geometric correction factors. The amount of systematic error is mainly related to the choice of correction factor and collimator aspect ratio. As seen in Figure 5 the ratios diverge as the aspect ratio decreases, and the use of these factors will greatly diminish the accuracy of the result for large collimator aperture radii. The error associated with counting statistics of the tally has two contributing factors. One, the emission probabilities for some of the energy bins in the source definition are low, which means a larger number of particle histories are needed to further decrease the fractional error. Two, the higher variances in the isotropic tally manifest themselves as greater dispersion/scatter in the photopeak ratios with decreasing radius, making it difficult to estimate the convergence of the systematic errors for each method. The variance and relative errors on the normalized spectra are straightforward to estimate, however. Once a normalized spectrum is obtained, the uncertainty in each bin can be estimated as the square root of the number of counts in that bin, according to Poisson statistics.

5. CONCLUSIONS

A numerical model coupling ORIGEN burn data with MCNP 6.1 was developed to predict emission spectra for different burnups and decay times in irradiated nuclear fuel. Spectra were simulated in MCNP 6.1 using both an isotropic source definition and a monodirectional source distributed over a characteristic sub-volume. This variance reduction technique showed reasonable quantitative agreement with the analog problem (isotropic source) while reducing the computational cost by up to seven orders of magnitude. Approximating the field of view as a truncated cone yielded a systematic error of 45% for a 1 mm collimator aperture. Approximating it as a cylinder with hemispherical end caps yielded a systematic error of 18% for the same collimator radius though in most other cases the truncated cone approximation resulted in smaller errors. The variance reduction technique rapidly improves in accuracy and computational savings as the aspect ratio of the collimator is increased making the method particularly effective for problems involving narrow collimators. As the field of view tends towards a degenerate cylinder, the ratio of count rates between the analog and non-analog methods converges to unity. However, making the aperture size too small will, unsurprisingly, reduce the detector signal to background rates, as was the case in the present design.

ACKNOWLEDGEMENTS

REFERENCES

[1]   X-Ray Mass Attenuation Coefficients - Water, Liquid, NIST
       https://physics.nist.gov/PhysRefData/XrayMassCoef/ComTab/water.html
       Accessed 15 Jul 2018

[2]   Jacobsson S, Bäcklin A, Håkansson A, P Jansson (2000) A tomographic method
       for experimental verification of the integrity of spent nuclear fuel. Appl Rad
       Isotopes. 53:681–689

[3]   Jacobsson S, Håkansson A, Jansson P, Bäcklin A (2001) A tomographic method
       for verification of the integrity of spent nuclear fuel assemblies - II: Experimental
       investigation. Nucl Technol. 135

[4]   Jacobsson S, Håkansson A, Bäcklin A, Jansson P, Osifo O, Willman C (2006)
       Tomography for partial-defect verification : experiences from measurements using
       different devices ESARDA Bulletin. 33:15–25

[5]   Lundqvist T, Jacobsson S, Håkansson A (2007) SPECT imaging as a tool to prevent
       proliferation of nuclear weapons. Nucl. Instruments Meth A. 580:843–847

[6]   Jacobsson S, Lundqvist T, Håkansson A (2008) Verification of completeness of
       spent nuclear fuel assemblies by means of tomography. PHYSOR 08 4:3131–3137

[7]   Parker H, Joyce M (2015) The use of ionising radiation to image nuclear fuel: A
       review. Prog Nucl Energy. 85:297–318

[8]   Jansson P,Svärd S, Håkansson A, Bäcklin A (2006) A Device for Nondestructive
       Experimental Determination of the Power Distribution in a Nuclear Fuel Assembly.
       Nucl Sci Eng. 152:76-86, 2006.

[9]   Andersson P, Holcombe S (2017) A computerized method (UPPREC) for quantitative analysis of irradiated nuclear fuel assemblies with gamma emission tomography at the Halden reactor. Ann Nucl Energy. 110:88–97

[10]   Holcombe S, Jacobsson S, Hallstadius L (2015) A Novel gamma emission tomography instrument for enhanced fuel characterization capabilities within the OECD Halden Reactor Project Ann. Nucl. Energy 85:837–845

[11]   Lanthanum Bromide Scintillation Detectors, Ortec-online.com. (2017) http://www.ortec-online.com/-/media/ametekortec/brochures/lanthanum.pdf Accessed 15 Dec. 2017.

[12]   Kawrakow I, Fippel M (2000) Investigation of variance reduction techniques for Monte Carlo photon dose calculation using XVMC. Phys Med Bio 45:2163-2183

[13]   Rearden B, Jessee M (2016) "SCALE Code System."

[14]   Goorley T, et al., "Initial MCNP6 Release Overview", Nuclear Technology, 180, pp 298-315 (Dec 2012).

[15]   J. Nilsson (2010), Using the LaBr3:Ce scintillation detector for mobile γ-spectrometry.
http://lup.lub.lu.se/luur/download?func=downloadFile&recordOId=2157130&file OId=2157384 Accessed 17 Feb. 2018

II. COMPARISON OF A SEMI-ANALYTIC VARIANCE REDUCTION TECHNIQUE TO CLASSICAL MONTE CARLO VARIANCE REDUCTION TECHNIQUES FOR HIGH ASPECT RATIO PENCIL BEAM COLLIMATORS FOR EMISSION TOMOGRAPHY APPLICATIONS

Seth Kilby[1], Jack Fletcher[1], Zhongmin Jin[1], Ashish Avachat[1], Devin Imholte[2], Nicolas Woolstenhulme[2], Hyoung K. Lee[1], Joseph Graham[1]

[1]Missouri University of Science and Technology 301 W 14th St. Rolla, MO 65409
[2]Idaho National Laboratory 1955 N. Fremont Avenue Idaho Falls, ID 83415

ABSTRACT

A semi-analytic variance reduction technique developed for collimated gamma emission tomography problems was compared to classic Monte Carlo variance reduction techniques within the Monte Carlo N Particle Transport (MCNP) code. In the semi-analytic technique, a computationally efficient, non-analog, monodirectional source biased Monte Carlo simulation is first performed. Analytical expressions are then used to correct for solid angle and field-of-view effects introduced by the non-analog source definition. This variance reduction technique was compared with deterministic transport sphere (DXTRAN) and geometry splitting variance reduction schemes to determine the accuracy and computational savings of each technique relative to an analog pulse height tally (F8 tally) at 1, 3, 5, and 10 mm collimator aperture radii. The computational savings and accuracy were evaluated for seven photopeaks. While the monodirectional source biasing technique overestimated the count rates by approximately 19%, it offered computational saving factors on the order of 10^8-10^{13} over the range of collimator radii studied. DXTRAN and geometry splitting methods yielded higher accuracy, but computational savings range

from approximately 0.13-2.2 and 0.07-2.9, respectively indicating marginal improvement at best.

1. INTRODUCTION

1.1. HIGH ASPECT RATIO PENCIL BEAM COLLIMATORS FOR GAMMA RAY EMISSION TOMOGRAPHY

Photon collimators have many applications in the fields of medicine and radiation imaging [1]. Collimators allow for control over beam shape and width, and as a result, collimators facilitate imaging and reduce radiation dose to a person or imaging object. Gamma-ray collimators work by defining a small solid angle from which isotropically emitted gamma rays are sampled. The inherent difficulty in modeling narrow, high aspect ratio collimators using Monte Carlo (MC) radiation transport is that only a small proportion of particles is likely to pass through the collimator. This proportion is comparable to the ratio of the collimator solid angle to the total solid angle (4π steradians). Thus, the smaller the collimator, the fewer the number of particle histories that contribute non-zero weights to tallies placed on the exiting side of the collimator. The purpose of this work is to use several variance reduction techniques to transport gamma rays through a narrow collimator and compare the rates of convergence of each technique to that of a fully analog simulation. This work was motivated by a project to design a submersible gamma tomography system to examine next-generation nuclear fuels [2]. Gamma ray tomography is a technique that has been utilized to examine full scale pressurized water reactor and boiling water reactor fuel assemblies. For large scale emission tomography problems such as those conducted at the Halden Reactor Project in Norway or the Forsmark Nuclear Power Plant in Sweden,

pencil beam collimators are commonly used in conjunction with high purity germanium detectors (HPGe). These systems use the strong material attenuation of tungsten or lead with the superior energy resolution, typically less than 1% at 662 keV, of an HPGe detector [3]–[5]. However, large scintillator crystals coupled with photo-multiplier tubes can be used instead of HPGe detectors to provide greater counting efficiency at the cost of energy resolution. Nonetheless, these systems are difficult to model as they generally require thousands of detector projections to obtain a well-constructed tomograph. Thus, it is not a particularly efficient use of computational resources to model detector signal using Monte Carlo N Particle Transport (MCNP) or GEANT4 in low particle count regions such as those that are created due to collimation [3]–[12]. It is common to rely on numerical techniques, such as ray tracing matrices, at the expense of some degree of accuracy, as the user makes assumptions about either the attenuating media or the particle interactions throughout the problem. For emission tomography problems that analyze a fuel assembly or even a single fuel pellet, the associated modeling challenges consist of low-sampled activity and high geometric and material attenuation. Low-sampled activity tends to lead to longer acquisition times, and smaller fuel geometries force users to utilize smaller collimator diameters to improve spatial resolution, which further increases geometric attenuation. The necessity for efficient Monte Carlo or deterministic methodologies for these high aspect ratio transport problems becomes apparent to acquire an efficient simulation without sacrificing accurate results.

1.2. MONTE CARLO VS DETERMINISTIC TECHNIQUES

In radiation imaging system design, radiation transport modeling can be used to predict detector response and performance before physical prototyping begins. Within radiation transport modeling, the techniques that are primarily used are deterministic, MC, or some combination of the two. Deterministic techniques focus on solving systems of equations that govern the mean properties of the particles being transported while MC techniques calculate the stochastic trajectories for a vast number of individual particle histories. Deterministic techniques are generally faster than MC based techniques at calculating statistical properties. Deterministic equations predict average particle behavior such as average energy, average cross section, average flux or grouped probability distributions. Discrete ordinate techniques, the most common of the deterministic techniques, rely on phase space discretization. Phase space discretization could be thought of as the segmentation of phase space into boxes of decreasing size toward the region of interest. As a result, discrete ordinate techniques can provide accurate information regarding parameters such as the flux in the system throughout all of phase space [13]. Consequently, deterministic techniques are simpler and place less demand on computational resources. However, a deterministic approach generally requires the selection of a suitable averaging, grouping or differencing scheme prior to solution.

MC, in contrast, is a powerful technique that can statistically transport particles through user-defined geometries and media. MC methods rely on simulating individual particle tracks and recording, in a tally, their average behavior. The nature of the particles in the system can be inferred using the central limit theorem from the average behavior of the simulated particles that are recorded in tallies assuming a sufficient number of particle

histories [14]. MC methods tend to be inefficient, in comparison to their deterministic counterparts, as most computational resources are utilized tracking particles that are not likely to contribute to the solution. Compared to deterministic techniques, however, there are two main advantages of MC transport. First, MC techniques have a high degree of efficacy for transport within more complex geometries, which implies that they provide greater accuracy when the problem geometry is complex. Second, they are generally not bound by strict energy grouping; as a result, the user may utilize continuous energy transport [15]. The coupling of continuous energy and complex 3D geometries with time allows for a detailed representation of a transport problem. Since MC does not use increasingly discretized phase space boxes such as those used in discrete ordinance methods, there is no averaging required a priori in phase space. Realizing such solutions, however, requires increasingly powerful computational resources or utilizing methods to reduce the convergence statistics of a given radiation transport problem. While arguably a more accurate representation of the physics, the time required for a well-converged solution is larger than that of typical deterministic methodologies, and as a result, certain problems can be computationally prohibitive. This phenomenon forces users to choose between efficiency and accuracy in their simulations. It is possible to compromise, however, with the use of variance reduction techniques in conjunction with MC to reduce the computational time and resources needed to converge, within a specified certainty, to a solution.

The primary disadvantage of variance reduction is the ability of the technique to give solutions that are misrepresentative of the physics of the problem. Variance reduction techniques are non-analog, that is to say, they introduce some non-physical mechanism

(e.g. splitting one particle into two half particles) to accelerate statistical convergence [13] [15]. In order to produce a result with a physical meaning, they must also apply a procedure for correcting the running average in question. Additionally, while variance reduction techniques can help bridge the gap between MC and deterministic approaches, variance reduction can only reduce computational cost by a given amount that is reflective of the method utilized, problem geometry, and the transport physics.

1.3. MONTE CARLO VARIANCE REDUCTION TECHNIQUES

Within the MCNP package, there exist global variance reduction techniques that users enable in order to increase the precision of tally statistics. As mentioned previously, these techniques can be split into various categories, and the techniques of focus will be those that can be applied to an F8 pulse height tally. It should be noted that the weight window generator was designed for non-F8 tallies. The generator estimates the importances of single particles within phase space, and the generator cannot estimate the importance of a collection of particles in phase space. Therefore, within MCNP, the weight window generator is incompatible with an F8 tally [14].

Perhaps the simplest applicable variance reduction technique is geometry splitting and roulette, which is a population control method. In geometry splitting and roulette, a geometry is subdivided into smaller pieces with different importance values within a cell [13][16]. This allows for particles to be virtually split, which increases the number of potential particles impinging on the tally. For example, if a geometry is divided into two sublayers, as a particle crosses from the layer closest to the source into the layer closest to the tally surface, it is split into two particles with identical velocity, but each with a fraction

of the original particle's weight. If particles are successively split as they approach a tally surface, the total number of histories contributing to a mean can be multiplied, thereby reducing the variance on the mean. In the case of roulette, a particle travels from a cell of higher importance to one of lower importance, and as a result, this particle has a probability to roulette. This process does not change the tally mean due to the internal weight adjustment. The result is either an increased quantity of particles within a cell, in the case of geometry splitting, or a reduction in tracked particles that will likely not interact with the tally. This is generally considered a safe variance reduction technique because weight is conserved while the particle count increases or decreases. For example, if a photon transports from a cell of importance 1 to importance 3 the number of branches that are created from that split is 3, while the weight of each branch is one third. Splitting occurs when a particle moves from a lower importance cell to a higher importance cell. If the particle moves from the cell of importance 3 to the cell of importance 1 then the particle has a 33% probability to survive the transport or a 67% probability to roulette. If the particle survives the winnowing process, the weight is readjusted to 1. If R is any ratio of importances between two consecutive cells, then a general form can be stated as seen in Equation 1.

$$R = \frac{I_2}{I_1} \tag{1}$$

If R is greater than 1 a split occurs, and if R is less than 1 a roulette can occur. The summed constituent weights must be conserved during a split or roulette. While this is relatively simple concept if R is an integer, an integer number is not required. If R is a non-integer greater than 1, the split is determined probabilistically. For example, if R is 2.5 then the particle is split into 3 with an occurrence probability of 50% and 50% occurrence

probability of being split into 2. If 2 and 3 are floor and ceiling values respectively and weight is conserved along each branch of a split, the weights are still conserved. Since weight is internally conserved among each of the split branches, this technique is simple to apply, and it offers the user a great deal of reliability in the resulting accuracy of the simulation. Another population control method related to geometry splitting and roulette is weight windowing. Within the F8 pulse height tally framework, it is not recommended to utilize the inbuilt weight window generator [13][16]. However, it is feasible to simulate the weighting value. This is not a trivial process, and generally requires some initial weight window operations such as using a deterministic approach to determine the importance function as a function of space, time, and energy. Programs such as ADVANTG and other adjoint deterministic techniques can provide detailed deterministic importance functions that estimate the optimal weight window for a given transport problem [17][18]. It should be noted that the weight windowing method can be applied to all elements of phase space whereas geometry splitting is limited to spatial dimensions.

Another category of variance reduction is modified sampling techniques. Within this category are the specific techniques of forced collisions, source biasing, implicit capture, and exponential transform. These techniques generally modify the way MCNP scores a particle. In the case of exponential transforms, the path length in a preferred direction is stretched between collisions by adjusting the total interaction cross section as seen in Equation 2,

$$\Sigma_t^* = \Sigma_t(1 - p\mu) \tag{2}$$

where p is the stretching parameter and μ is the cosine of the angle between the direction of the particle and the stretching direction [13][19]. This has the benefit of amplifying

particles within highly attenuating media, such as in deep shielding problems, which can be useful in determining the photon penetration in a collimator. This technique requires weight windowing to adjust for the stretching that takes place. Source biasing, in contrast, allows the user to change how the transport is sampled. For example, a source could be biased in a preferential direction or biased in terms of the probability of emission for a specific particle at a given energy. The location of the source itself can also be biased. Source biasing allows the user to take advantage of nonanalog processes to decrease the variance per particle while increasing the figure of merit, which implies a more efficient simulation. It is rather intuitive, for example, that a source directionally biased towards a tally region would have a higher sampling efficiency, in comparison to an analog simulation of an isotropic source. Source biasing, however, usually requires a correction to account for degrees of freedom removed from the random sampling process; in this case, direction has been thus affected. In an input file within MCNP, this manifests itself as a source biasing card that should correct for the differences in sampling, though analytical corrections for this effect are possible as well.

Forced collisions are another type of variance reduction method that alter the mean free path of the particle. Forced collisions force particles to undergo an interaction if they enter any given cell. The particle and the associated weights split into two subcomponents, collided and uncollided. This method is generally useful in creating source inputs for DXTRAN spheres, point detectors, or ring detectors. Implicit capture is a technique that allows a particle to continue transporting even after colliding in a material. When a particle interacts in a medium, all potential interactions are recorded with relevant probabilities, as

opposed to exclusively undergoing an absorption event. The particle will then travel as if it had not been absorbed, but with an adjusted weight, multiplied as in Equation 3,

$$W_f = W_i \left(1 - \frac{\sigma_a}{\sigma_t}\right) \tag{3}$$

where W_f is the final adjusted weight, W_i is the initial weight, and $\frac{\sigma_a}{\sigma_t}$ is the ratio of the absorption cross section to the total cross section [19][20]. This allows for the weight to be properly adjusted to compensate for losses associated with absorption. This technique is useful in problems where strong material attenuation causes absorption events.

The last set of global variance reduction schemes are partially deterministic methods including DXTRAN spheres. This is a weight-independent technique that allows the user to improve sampling within an unlikely region of phase space by applying a particle split, in conjunction with a split transport. When an interaction occurs, a particle is split into two counterparts; one continues transporting in the direction dictated by the scattering physics (the non-DXTRAN particle), while the other travels directly towards a user-specified spherical surface surrounding the unlikely region of phase space usually a tally region (the DXTRAN particle). The DXTRAN particle only interacts upon entering the sphere, therefore assuring that particles reach the desired region, independent of the interaction. The DXTRAN particle is the uncollided fraction of the original particle, while the non-DXTRAN particle is the collided fraction of the original particle, although it should be noted that in this method, weight is not conserved: since the collided particle continues with the same weight it was originally assigned, the total weight of the interaction is greater than the initial starting weight at the collision location. This is due to how the

weight is assigned for the DXTRAN particle. The DXTRAN particle has a weight that is described in Equation 4,

$$W_{DXTRAN} = W_i \frac{P(\mu)}{P_{arb}(\eta)} e^{-\lambda} \tag{4}$$

where W_{DXTRAN} is the weight of the DXTRAN particle. W_i is the original weight. $\frac{P(\mu)}{P_{arb}(\eta)}$ is the ratio of a probability density function dependent on the cosine of the angle between the scattering direction and incoming direction to an arbitrary probability density function, and $e^{-\lambda}$ is the negative exponential of the optical mean free path. However, to make up for this weighting issue, the DXTRAN particle has zero weight for all tallies outside of the DXTRAN sphere. The non-DXTRAN particle has a standard weight for all tallies outside the DXTRAN sphere and will not impinge in a tally within the DXTRAN sphere if the particle reaches the sphere on the next flight. It is also advantageous to view DXTRAN spheres not only as mechanisms to increase sampling efficiency in regions where particles are unlikely to transport, but also to shield high-weight particles from impinging upon a tally. Nested DXTRAN spheres may be utilized to control weight fluctuations from collision events occurring near the sphere boundary; with the addition of more DXTRAN spheres, the user gains greater control over the particle weight and sampling in the area of interest [20][21].

The aforementioned variance reduction techniques can be utilized to lower tally variance without distorting the tally mean. For this manuscript, an analytical source-biased variance reduction technique is compared in MCNP to geometry splitting, DXTRAN spheres, and analog simulations of gamma ray transport through pencil beam collimators with varying radii. The authors intend to provide the reader with a notion of various

tradeoffs between accuracy and efficiency using different variance reduction techniques for high aspect ratio pencil beam collimator problems.

2. METHODOLOGY

2.1. SOURCE DEFINITION

The variance reduction techniques were applied to a single basic geometry, containing a source representing an irradiated fuel pin, a pencil beam tungsten collimator, and a detector, as seen in Figure 1. The source term utilized in the MCNP variance reduction simulations was created using Oak Ridge Isotope Generator (ORIGEN), within the SCALE package [22]. A gamma spectrum of spent nuclear fuel, dependent on the burnup, was generated and implemented. From the ORIGEN output, the user may acquire gamma emission intensities, and upon normalizing the spectrum, emission probabilities for each energy bin. The gamma spectrum generated from the fuel in ORIGEN was divided into 3000 energy bins from 0-20 MeV with a width of 6.67 keV, and the gamma source energies and probabilities of emission were implemented within the MCNP source definition. The F8 tally, however, utilized 1024 energy bins with an energy width of 2 keV. An in-depth description of how this source term was generated and implemented is found in Kilby *et al.*; Details of the source description, however, are not particularly critical in the following analysis [2]. The source term may be regarded as an unspecified mixed radionuclide multi-photon source. The results and conclusions largely transfer to single photon sources and single nuclide multi-photon sources.

The purpose of a pencil beam collimator geometry is to sample gamma radiation from a small solid angle; this allows the collection of high spatial resolution tomographs. The collimator dimensions were altered across multiple simulations to model the effect of aspect ratio variations. Since the length of the collimator is fixed by material attenuation constraints at 15.24 cm, the radius is modified to introduce variation in the aspect ratio. Due to the aspect ratio being a function of the length of the collimator and the diameter of the aperture, the decrease in the radius yields a greater effect on the aspect ratio. The radii simulated were 1, 3, 5 and 10 mm, while the scintillator detector dimensions were constant at 7.6×7.6 cm. Geometry splitting, DXTRAN spheres, and an analog simulation without Russian roulette were compared to an analytically-corrected, source-biased technique developed by Kilby *et al.* [2]. Roulette was disabled because of the adverse effect the technique has on the accuracy pulse height tallies [23]. Simulation accuracy and computational savings were analyzed to determine which variance reduction schemes are preferable as the radius of the collimator changes. As a final note to the reader, the purpose of this work is to provide a foundation to view variance reduction techniques independently. Combining variance reduction techniques may provide smaller tally variance, yet the time required to implement them can in many ways be an unoptimized use of the time if the problem could be more easily served by applying a simple technique. It should also be noted that these techniques are compared for problems involving a pencil beam collimator and gamma radiation transport. While this is an important class of transport problems encountered in radiation imaging, the conclusions presented here do not necessarily extend to other radiation transport problems.

2.2. GEOMETRY SPLITTING/ROULETTE

For geometry splitting and roulette, a geometry must be partitioned into smaller pieces for importance manipulation to have a beneficial effect on the transport problem. In the case of high aspect ratio pencil beam collimators, increased particle count is required in the collimator aperture due to extreme geometric attenuation; therefore, the collimator was split into 5 equal parts as a rough approximation to maintain a relatively constant particle population through the split regions as seen in Figure.1.
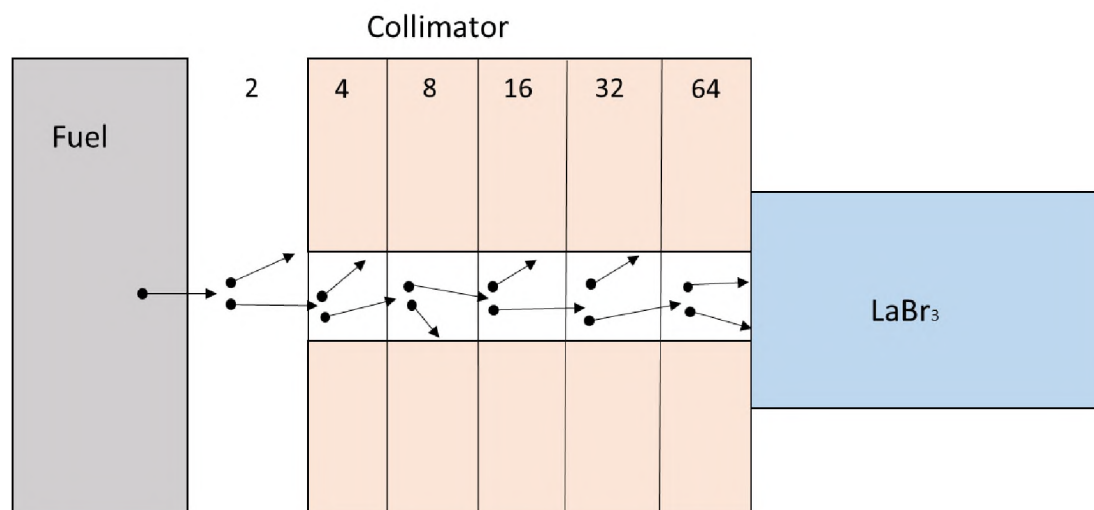
Figure 1: Geometry splitting of the tungsten collimator (not drawn to scale)

Within each of the split cells, the importance ratio defined in Equation 1 increases by a factor of 2 as the particles transport through the cells, towards the detector and associated F8 tally. As the radius of the aperture is increased, the importance ratios remain the same. It should be noted that a user may split the geometry into smaller portions and introduce additional importance ratios to increase or maintain greater control of particle count; however, the user will need to ensure that the population of particles remains

relatively constant throughout the split region. Five evenly spaced cells, each with a width of 3.05 cm, were created with importance ratios of 2 to maintain a relatively constant number of particles throughout the transport problem. If the collimator aspect ratio increases, then the user may consider increasing the importance ratios.

2.3. SOURCE BIASING

The analytically-corrected, directionally source-biased technique developed in Kilby *et al.* is compared to the global variance reduction techniques within MCNP. Source biasing, as with all modified sampling techniques, will tend to overestimate the count rates as the source photons are forced into the collimator aperture, but corrections are required to compensate for this effect. Therefore, this technique relies on two parts: a sub-volume correction factor and a solid angle correction factor. Source points are only defined the sub-volume of the imaging object within the field of view of the collimator. The region is defined as the intersection of the source volume with an extended wall of the collimator. It is important to note that this study approximates the fuel geometry as a conical frustum as developed in Kilby *et al.* Due to nonzero importance values within the tungsten collimator, umbral and penumbral effects within the collimator are possible.

A solid angle correction factor based on a point source approximation is introduced; this correction is acceptable if and only if the aspect ratio of the collimator is high. For the monodirectional source-biased technique, all the source points are sampled from a volume defined as the intersection of the cylindrical fuel capsule and the cylindrical collimator, as seen in Figure.2.
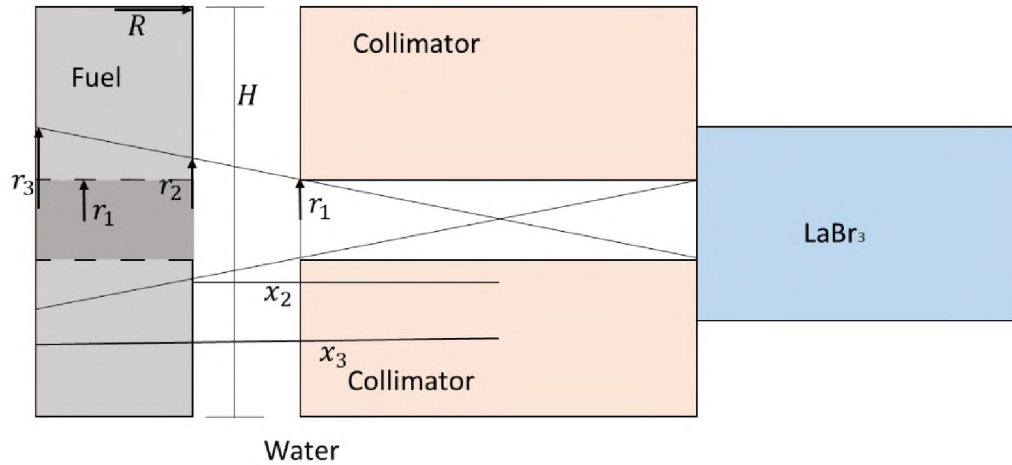
Figure 2: Analytical source biased geometry (not drawn to scale)

The aforementioned volumetric correction factor is defined in Equation 5,

$$F_{v,cone} = \frac{(r_3{}^2 x_3) - (r_2{}^2 x_2)}{3R^2 H} \tag{5}$$

where r_3 is the radius of the conical frustum's larger base, and r_2 is the radius of the smaller base. x_3 is the distance from r_3 to the center of the collimator aperture, and x_2 is the distance from r_2 to the center of the collimator aperture. R is the radius of the source, and H is the height of the source. Additionally, as the radius of the pencil beam collimator aperture decreases, the effective solid angle decreases as well. This implies that as the aspect ratio increases, the point-source approximation for the calculation of the solid angle correction factor becomes more accurate. The factor is shown in Equation 6,

$$F_{\Omega} = \frac{r_1^2}{4L^2} \tag{6}$$

where L is the length from the center of the source to the detector, and r_1 is the radius of the collimator aperture as seen in Figure 2.

To complete the correction for the departure from isotropy, the correction factors must be multiplied together with the total activity of the source, which is acquired through ORIGEN. This can be seen in Equation 7,

$$\text{Corrected Activity} \cong A_{Source}(F_v \times F_\Omega) \tag{7}$$

where A_{Source} is the activity of the source. F_v is the correction factor derived from the sub volume defined in Equation 5, while F_Ω is the solid angle correction factor defined in Equation 6.

2.4. DXTRAN SPHERE

The DXTRAN sphere method begins with a sphere around a cell or group of cells in MCNP. This sphere, while not defined as a physical cell, alters the way particles interact in the entire MCNP simulation. The DXTRAN sphere causes all particles that interact in any media, outside the sphere, to split into two components, DXTRAN and non-DXTRAN. As discussed previously, the DXTRAN particles will move toward the user-defined sphere, while the non-DXTRAN particle will continue its Markovian walk until, it reaches the DXTRAN sphere boundary or is absorbed. The DXTRAN particle will always transport toward the sphere volume, wherein it has the weight defined by Equation 5, but zero weight everywhere outside the DXTRAN sphere region. This principle ensures that the scattered particle will reach the desired tally region regardless of strong attenuation or low sampling efficiencies due to small solid angles. For high aspect ratio pencil beam collimators, DXTRAN spheres can be used to account for particles that miss the detector tally due to small angle scattering. DXTRAN spheres can further increase the likelihood of a particle impinging on a tally by using an inner radius. If an inner radius is specified, the likelihood

of a particle being sampled is increased by a factor 5. For this simulation, a DXTRAN sphere was added to the detector tally in the MCNP simulation as seen in Figure 3.
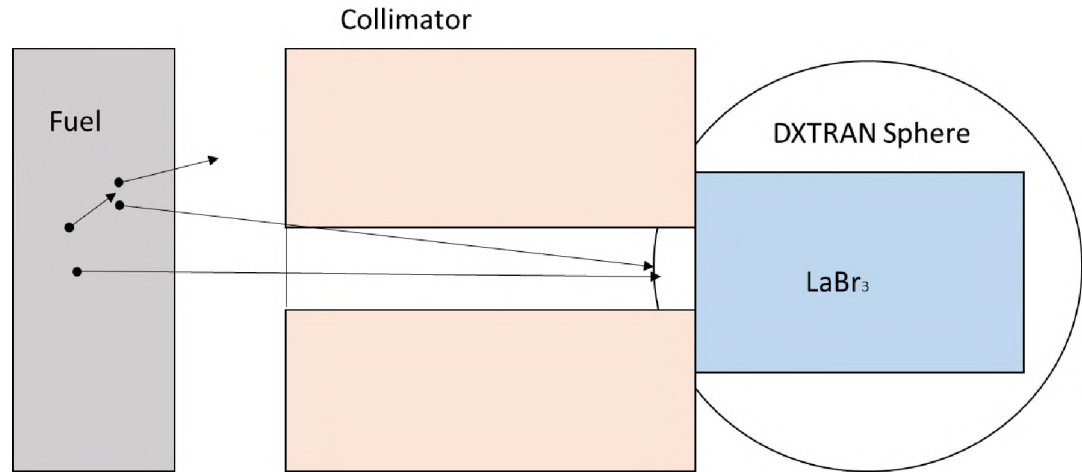
Figure 3: Geometry with a DXTRAN sphere around the detector cell tally region

The DXTRAN sphere is defined with an inner radius of 8.52 cm and an outer radius of 11.76 cm. It is important to note that scattering towards the inner radius is five times likelier than towards the outer. The collimator aperture is increased to determine computational savings and accuracy with changes to the aspect ratio.

2.5. COMPUTATIONAL SAVINGS

To evaluate the computational savings of each variance reduction technique one utilizes a figure of merit. In MCNP the figure of merit is defined in Equation 8,

$$FOM = \frac{1}{P^2 T} \tag{8}$$

where P^2 is proportional to the inverse of the particle histories, and T is the simulation time, proportional to the number of particle histories [20]. A large figure of merit over the

course of the simulation is desirable. While this is an indicator of the efficacy of a simulation, the authors wish to utilize a figure of merit that considers the particle history counts and the respective variances. This allows for a broader time-independent comparison that can be extended to operation with different computational resources, such as high-powered computing clusters. Ratios of this figure of merit style are used to evaluate the computational savings between variance reduction techniques.

In a tally bound by Poisson statistics, the mean (μ) is the number of counts within the tally bin; it is proportional to the number of particles utilized in the simulation. In a Poisson process, the mean is equal to the variance. However, to incorporate the volumetric correction factors of the analytical source biased technique or the other variance reduction methods, a factor f_m is needed, where m is the method or specific geometry used. This is shown in Equation 9.

$$\mu = f_m NPS_m \tag{9}$$

By substituting variance in for the mean, Equation 10 results.

$$f_\mathrm{m} = \frac{\sigma_m^2}{NPS_m} \text{ where } \sigma^2 = \text{Counts} \tag{10}$$

To incorporate the fractional error associated with the MCNP tally bins, the fractional error (ϵ_m) can be expressed as a function of counts (c_m) and standard deviation, as shown in Equation 11.

$$\epsilon_m = \frac{\sigma_m}{c_m} = \frac{1}{\sqrt{c_m}} = \frac{1}{\sqrt{f_m NPS_m}} \tag{11}$$

For a given fractional tally bin error (ϵ_m), NPS$_1$* is the minimum number of particles needed to achieve the fractional error of the tally for method 1. NPS$_2$* is the minimum number of histories for method 2. Computational savings (S) is then defined in Equation 15,

$$S = \frac{NPS_2^*}{NPS_1^*} = \frac{NPS_{m,2}\sigma_{m,1}^2}{NPS_{m,1}\sigma_{m,2}^2} \tag{12}$$

where NPS is user-defined in each MCNP input file, and σ_m^2 is acquired from the MCNP output file for a given NPS. In this relationship, if S > 1, then the simulation results in net computational savings. If S < 1, then the simulation results in increased computational expenses.

3. RESULTS

3.1. VARIANCE REDUCTION COMPARISONS

When examining the efficacy of a variance reduction technique, it is necessary to benchmark the technique against an analog simulation. In this case, as accurate photopeak data are desired within a reasonable simulation time, each technique is compared at 7 strong photopeaks energies: 0.500, 0.608, 0.669, 0.761, 0.768, 0.800, and 1.60 MeV. These photopeaks were determined to be of importance from the ORIGEN simulations that formulated the emission data for the transport calculations. In order to calculate the photopeak accuracy of a variance reduction technique, the bin counts in the variance reduced F8 tallies were divided by the bin values of the analog F8 tally. These ratios can be seen in Table 1, and error bars were calculated using error propagation by division. The error bars can be seen in Table 2. The DXTRAN values are accurate, within the error bars until the 1 mm case where some variance is noted. The 0.802 MeV peak and the 1.6 MeV peak differ from the analog case the most, but these could result from random error. Given the uncertainties, the results are still within agreement.

Table 1: Variance-reduced-to-analog photopeak ratios for a monodirectional source-biased conical frustum (cone) approximation; geometry splitting; and DXTRAN as a function of collimator aperture radius

Energy (MeV)	Cone Approximation				Geometry Splitting				DXTRAN			
	1 mm	3 mm	5 mm	10 mm	1 mm	3 mm	5 mm	10 mm	1 mm	3 mm	5 mm	10 mm
0.500	1.32	2.17	3.53	11.3	1.04	0.99	0.99	1.00	0.98	0.97	0.98	0.99
0.608	1.26	2.06	3.35	10.6	1.09	0.98	0.99	0.99	0.98	0.96	0.99	1.00
0.669	1.15	2.10	3.33	10.8	0.97	1.00	0.99	1.00	0.94	0.98	0.98	1.01
0.761	1.20	2.14	3.48	11.1	0.97	1.01	1.00	1.00	0.95	1.00	1.00	1.00
0.768	1.24	2.14	3.46	11.2	0.99	1.00	1.00	1.00	0.98	0.99	0.99	1.00
0.802	1.00	2.00	3.35	11.0	0.89	0.95	0.98	1.01	0.89	0.93	0.96	0.99
1.600	1.17	1.93	3.13	10.2	1.16	1.00	0.99	1.00	1.40	1.00	0.98	1.00

Table 2: Error bars for each of the variance reduction techniques as a function of collimator aperture radius

Energy (MeV)	Cone Approximation				Geometry Splitting				DXTRAN			
	1 mm	3 mm	5 mm	10 mm	1 mm	3 mm	5 mm	10 mm	1 mm	3 mm	5 mm	10 mm
0.500	5×10^{-2}	4×10^{-2}	3×10^{-2}	3×10^{-2}	6×10^{-2}	1.9×10^{-2}	9×10^{-3}	4×10^{-3}	4×10^{-2}	1.7×10^{-2}	8×10^{-3}	3×10^{-3}
0.608	1.0×10^{-1}	8×10^{-2}	6×10^{-2}	7×10^{-2}	1.3×10^{-1}	4×10^{-2}	2×10^{-2}	9×10^{-3}	9×10^{-2}	4×10^{-2}	1.9×10^{-2}	7×10^{-3}
0.669	8×10^{-2}	7×10^{-2}	5×10^{-2}	6×10^{-2}	1.0×10^{-1}	4×10^{-2}	1.7×10^{-2}	7×10^{-3}	7×10^{-2}	3×10^{-2}	1.6×10^{-2}	6×10^{-3}
0.761	4×10^{-2}	3×10^{-2}	2×10^{-2}	3×10^{-2}	4×10^{-2}	1.7×10^{-2}	8×10^{-3}	3×10^{-3}	3×10^{-2}	1.6×10^{-2}	7×10^{-3}	3×10^{-3}
0.768	2×10^{-2}	2×10^{-2}	1.5×10^{-2}	1.7×10^{-2}	3×10^{-2}	1.0×10^{-2}	5×10^{-3}	2×10^{-3}	2×10^{-2}	9×10^{-3}	4×10^{-3}	1.6×10^{-3}
0.802	8×10^{-2}	9×10^{-2}	7×10^{-2}	8×10^{-2}	1.1×10^{-1}	4×10^{-2}	2×10^{-2}	1.0×10^{-2}	8×10^{-2}	4×10^{-2}	2×10^{-2}	8×10^{-3}
1.600	9×10^{-2}	7×10^{-2}	6×10^{-2}	6×10^{-2}	1.1×10^{-1}	4×10^{-2}	1.9×10^{-2}	8×10^{-3}	3×10^{-1}	4×10^{-2}	1.8×10^{-2}	7×10^{-3}

Perhaps as anticipated, geometry splitting emerges as the most accurate of the techniques for all collimator sizes. The accuracy is resistant to changes in collimator aperture radius. This means that some of the weaker photopeaks are not adversely impacted through using this technique. It is important to note that a comparison of the Compton region was not considered in quantitative analysis, as the ability for the analog simulation to fully resolve the region is hindered by high geometric attenuation, which is exacerbated by decreasing collimator apertures. A significant increase in particle histories would be necessary to achieve a result with lower relative errors. The increase in the ratios at 0.802

and 1.60 MeV can be explained by statistical variations, and the photopeak count ratios with respect to the analog case do fall within the region for agreement, i.e. values close to 1. The conical frustum approximation overestimates count rates across all aperture sizes tested and is thus considered the least accurate method. However, the conically corrected photopeak count ratios trend toward agreement at higher collimator aspect ratios. At 1 mm, the conical frustum approximation produces satisfactorily comparable count rates within the photopeak bins to the isotropic case. The photopeak counts are, on average, 19% higher than the analog case—disregarding variance—and by increasing particle histories in the analog case, the associated error could be reduced, thus minimizing the variance.

3.2. COMPUTATIONAL SAVINGS

The computational savings from all the applied variance reduction techniques at each of the strongest intensity photopeaks are shown as a function of collimator radius in Figure 4. From Figure 4, the monodirectional bias case yields the greatest computational savings, between 10^8 and 10^{13} depending on the aperture size. In contrast, the DXTRAN and geometry splitting techniques vary in terms of computational savings and cost between 1-10mm.

Both methods have noticeable savings compared to the isotropic case for the 1 mm and 10 mm collimator apertures. The DXTRAN sphere method has a savings of approximately 2.3 and 1.0 at 1 mm and 10 mm, respectively. The geometry splitting method has a savings of 2.9 and 1.4 at 1 mm and 10 mm, respectively. This means that the variance reduction techniques at those collimator apertures do have a positive impact on the ability of the computer to arrive at a given fractional tally bin error per given particle.

However, at 3 mm and 5 mm, both the DXTRAN and geometry splitting are more computationally expensive than the isotropic analog case.
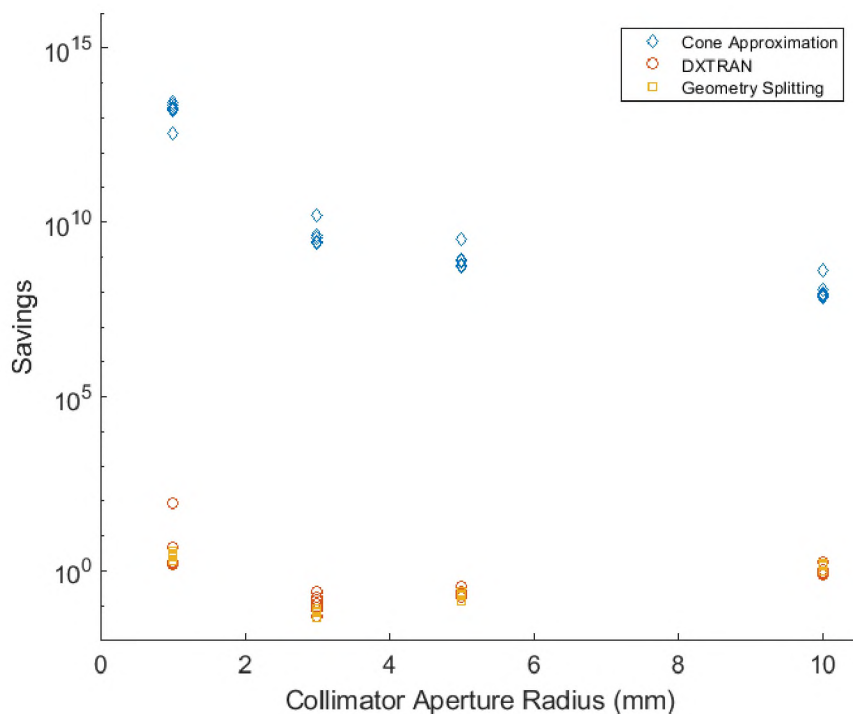
Figure 4: Computational savings for the seven strongest photopeaks, as a function of collimator aperture radius. Each of the seven strongest photopeaks are shown in each cluster

This means that for a given photopeak at a given collimator aperture radius, these methods have no positive impact on the ability of the computer to arrive at a given fractional tally bin error per given particle.

Upon closer inspection, there is no discernible benefit to the DXTRAN and geometry splitting methods solely by measure of the photopeak regions for the 3 mm and 5 mm collimator aperture. For the geometry splitting method, the average savings are

approximately 0.2 and 0.07 for the 3 mm and 5 mm collimator aperture radii respectively, implying that there are no computational advantages to the geometry splitting method solely to examine photopeaks in this type of problem. The DXTRAN method, meanwhile, yields an average savings of approximately 0.24 and 0.13 for the 3 mm and 5 mm radii respectively. For the purpose of measuring photopeak counts, both techniques offer little reduction to computational cost at these collimator aperture radii. While it is difficult to fully resolve the Compton region in the analog case, it is possible to compare savings across the entire spectrum as a function of radius to gauge each technique's effectiveness across the entire tally. These savings are visualized in Figure 5. When considering total tally bins, the variance reduction techniques do provide an appreciable increase in computational savings. For the DXTRAN method, a savings factor of 23, 0.31, 0.76, and 3.44 is achieved for 1, 3, 5, and 10 mm respectively, which is a significant improvement over the geometry splitting method, which has a savings of 4.2, 0.09, 0.27, and 2.1 at 1, 3 ,5 and 10 mm respectively. The DXTRAN method generally outperforms the geometry splitting method throughout each of the collimator aperture radii simulated.

Comparing Figures 4 and 6, one can conclude that tally bins associated with photopeaks converge more slowly using the geometry splitting with a slightly higher degree of accuracy than the other methods, the background and Compton continuum converge more rapidly than in the isotopic analog case.

Comparing Figures 4 and 6, one can conclude that tally bins associated with photopeaks converge more slowly using the geometry splitting with a slightly higher degree of accuracy than the other methods, the background and Compton continuum converge more rapidly than in the isotopic analog case. Thus, when modeling spectral

background, the DXTRAN method has advantages over analog simulation and geometry splitting. The source-biased technique, as in the photopeak regions, significantly outperforms the other variance reduction schemes with the caveat that its accuracy is only tolerable for high aspect ratio collimators.
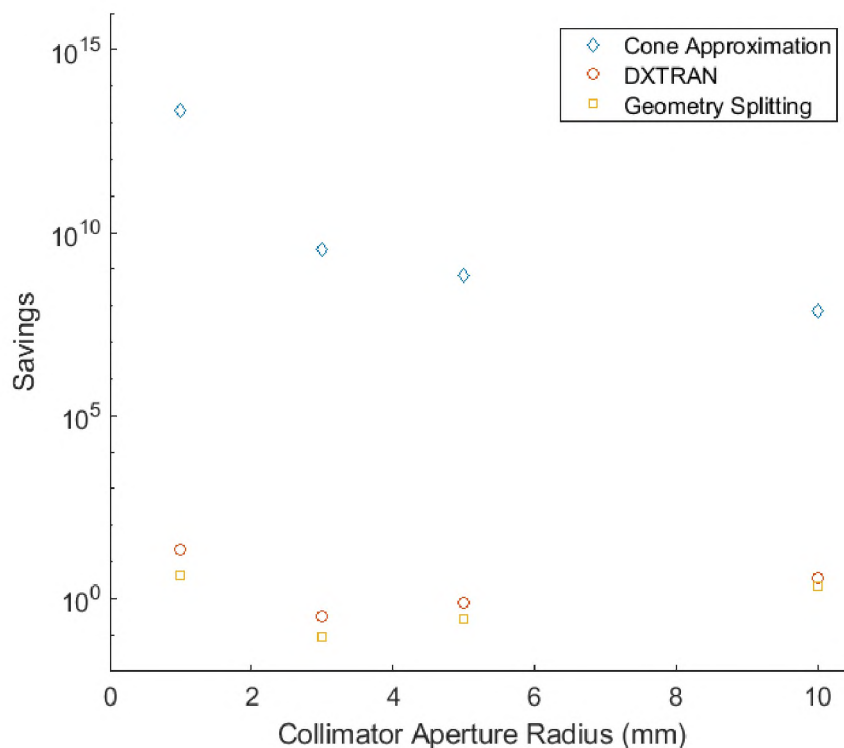
Figure 5: Computational savings for the total tally bin at varying collimator aperture radii

4. CONCLUSIONS

The speed and accuracy of three variance reduction techniques for accelerating radiation transport problems involving transport of gamma rays through narrow pencil

beam collimators was compared. Geometry splitting emerged as the most accurate by providing photopeak ratios nearly identical to those predicted from fully analog simulations. In contrast, the corrected monodirectional source biasing technique exhibited the least accuracy. However, as the collimator radius decreased, accuracy improved significantly. At 1 mm, photopeak counts were on average only 19% higher than in the analog case. The source biasing technique is expected to perform better as the collimator aspect ratio increases, due to increasing geometric attenuation mitigating small angle scattering and minimizing penumbral effects. The DXTRAN sphere provided accurate photopeak tallies except at 1 mm collimator aperture radius. This is most likely attributed to the fact weaker peaks are being better sampled within the system and therefore are being binned in the photopeak bin thus increasing the counts. This could be fixed by reducing the energy width of the tally bins.

With regard to computational savings, the corrected monodirectional source-biased technique provided the greatest computational savings over all of the collimator aperture radii. Compared to the fully analog simulations, DXTRAN spheres and geometry splitting were actually more computationally expensive for the 3 mm and 5 mm collimator aperture radii, indicating that computational resources are better spent on an analog simulation than to use the techniques when examining only the photopeak regions in the F8 tally. Considering the entire tally, the DXTRAN sphere sees a pronounced increase over the analog case in computational savings. Compared with the geometry splitting technique, the DXTRAN method performs better over the entire F8 tally spectrum at each of the collimator aperture radii simulated.

When choosing a variance reduction technique to utilize for high aspect ratio pencil beam collimator problems, it is important to understand which component of the spectrum needs to be analyzed. The geometry splitting method provides the least variation in accuracy and seems better poised to outperform the DXTRAN method for predicting photopeak intensities. The DXTRAN method should be used when accuracy and greater computational savings are desired over the entirety of the F8 tally spectrum (including the Compton background). Ultimately, the monodirectional source biasing technique is vastly more efficient than DXTRAN and geometry splitting but will only provide quantitative results when the aspect ratio of the collimator is large

ACKNOWLEDGEMENTS

REFERENCES

[1]   I. Kawrakow and M. Fippel, "Investigation of variance reduction techniques for Monte Carlo photon dose calculation using XVMC," Phys. Med. Biol, vol. 45, pp. 2163–2183, 2000.

[2]   S. Kilby et al., "A source biasing and variance reduction technique for Monte Carlo radiation transport modeling of emission tomography problems," J. Radioanal. Nucl. Chem., Apr. 2019.

[3]   H. M. O. D. Parker and M. J. Joyce, "The use of ionising radiation to image nuclear fuel: A review," Prog. Nucl. Energy, vol. 85, pp. 297–318, 2015.

[4]   A. Anastasiadis, "A Monte Carlo simulation study of collimators for a high-spatial-resolution Gamma Emission Tomography instrument," Uppsala Universitet, 2019.

[5]   T. Lundqvist, S. Jacobsson Svärd, and A. Håkansson, "SPECT imaging as a tool to prevent proliferation of nuclear weapons," Nucl. Instruments Methods Phys. Res. Sect. A Accel. Spectrometers, Detect. Assoc. Equip., vol. 580, no. 2, pp. 843–847, 2007.

[6]   P. Andersson and S. Holcombe, "A computerized method (UPPREC) for quantitative analysis of irradiated nuclear fuel assemblies with gamma emission tomography at the Halden reactor," Ann. Nucl. Energy, vol. 110, pp. 88–97, 2017.

[7]   S. Holcombe, S. Jacobsson Svärd, and L. Hallstadius, "A Novel gamma emission tomography instrument for enhanced fuel characterization capabilities within the OECD Halden Reactor Project," Ann. Nucl. Energy, vol. 85, pp. 837–845, 2015.

[8]   S. J. Svärd, A. Håkansson, A. Bäcklin, P. Jansson, O. Osifo, and C. Willman, "Tomography for partial-defect verification experiences from measurements using different devices Tomography for partial-defect verification − experiences from measurements using different devices," 2006.

[9]   S. Caruso, M. F. Murphy, F. Jatuff, and R. Chawla, "Determination of within-rod caesium and europium isotopic distributions in high burnup fuel rods through computerised gamma-ray emission tomography," Nucl. Eng. Des., vol. 239, no. 7, pp. 1220–1228, 2009.

[10]   S. Caruso, M. F. Murphy, F. Jatuff, and R. Chawla, "Nondestructive determination of fresh and spent nuclear fuel rod density distributions through computerised gamma-ray transmission tomography," J. Nucl. Sci. Technol., vol. 45, no. 8, pp. 828–835, 2008.

[11]   P. Andersson, S. Holcombe, and T. Tverberg, "Inspection of a LOCA test rod at the halden reactor project using gamma emission tomography," in Top Fuel 2016: LWR Fuels with Enhanced Safety and Performance, 2016.

[12]   S. Jacobsson, A. Bäcklin, A. Håkansson, and P. Jansson, "A tomographic method for experimental verification of the integrity of spent nuclear fuel," Appl. Radiat. Isot., vol. 53, no. 4–5, pp. 681–689, 2000.

[13]   M. C. Team, "MCNP-A General Monte Carlo N-Particle Transport Code, Version 5 Volume I: Overview and Theory X-5 Monte Carlo Team," 2003.

[14] J. T. Goorley et al., "MCNP6 TM USER'S MANUAL Alamos National Laboratory 2 NEN-5 Systems Design and Analysis, Los Alamos National Laboratory 3 XCP-7 Transport Applications, Los Alamos National Laboratory 4 NEN-5 Systems Design and Analysis, Los Alamos National Laboratory, contr," 2013.

[15] J. E. Morel, "Title: Deterministic Transport Methods and Codes at Los Alamos Deterministic Transport Methods and Codes at Los Alamos."

[16] T. E. Booth, "Common Misconceptions in Monte Carlo Particle Transport," 2011.

[17] S. W. Mosher et al., "ADVANTG-An Automated Variance Reduction Parameter Generator," 2015.

[18] A. Davis and A. Turner, "Comparison of global variance reduction techniques for Monte Carlo radiation transport simulations of ITER," Fusion Eng. Des., vol. 86, no. 9–11, pp. 2698–2700, Oct. 2011.

[19] K. J. Kelly et al., "implicit-capture simulations for quantification of systematic uncertainties from experimental environments," Nucl. Inst. Methods Phys. Res. A, no. July, 2018.

[20] T. E. Booth, "Pulse Height Tally Variance Reduction in MCNP PULSE-HEIGHT TALLY VARIANCE REDUCTION IN MCNP," 2004.

[21] T. E. Booth, K. C. Kelley, and S. S. McCready, "Monte Carlo variance reduction using nested dxtran spheres," Nucl. Technol., vol. 168, no. 3, pp. 765–767, 2009.

[22] B. T. Rearden and M. A. Jessee, SCALE Code System, no. April. 2016.

[23] J. S. Bull, "Validation Testing of Pulse Height Variance Reduction in MCNP," vol. 836, 2008.

[24] J. K. Shultis and R. E. Faw, "AN MCNP PRIMER by," 2004

III. DESIGN AND OPTIMIZATION OF A PINHOLE COLLIMATOR FOR A HIGH-RESOLUTION EMISSION GAMMA RAY TOMOGRAPHY SYSTEM

Seth Kilby, Joseph Graham

Missouri University of Science and Technology: 222 Fulton Hall 301 W. 14th St., Rolla, MO, 65401, smkbpc@mst.edu

1. INTRODUCTION

As next generation nuclear fuels are developed for use in advanced reactors, analyzing fission product migration and fuel structural changes in irradiated test fuel becomes a major priority in qualifying fuels for eventual deployment. Idaho National Laboratory (INL) is interested in utilizing an emission and transmission tomography system to image test capsules of next generation nuclear fuels. The focus of this abstract will be solely on the emission tomography part of a proposed system for the Advanced Test Reactor (ATR).

Emission tomography has been utilized for nuclear fuel characterization, nonproliferation, and safeguards research. Jacobsson, Holcombe, and Lundqvist studied fission product mapping and partial defect analysis of spent nuclear fuel using decay radiation of the fission products [1-6]. Experiments done at the Forsmark reactor in Sweden mapped ^{140}Ba utilizing Single-Photon Emission Computed Tomography (SPECT). The Halden reactor project, which examined cylindrical fuel elements, looked at fission products such as ^{137}Cs and ^{140}Ba/La. The main experimental drawbacks identified in these

previous studies were long decay times and the large number of slices needed to reconstruct a tomographic image.

Within the last decade, there has been a push for increasingly smaller spatial resolutions in multipurpose imaging systems such as those used in small animal SPECT. Most devices in that field have used scintillators coupled with silicon photomultipliers (SiPMs), charge coupled devices (CCDs), or compound semiconductors such as CdZnTe (CZT). Each of these detection systems have benefits and drawbacks. Scintillators coupled with a CCD can offer spatial resolution on the order of 10^1-10^2 microns. However, energy resolution degrades, especially with the use of EM-CCDs [7]. SiPMs offer improved energy resolution over CCDs, but do not offer the same spatial resolution. However, SiPMs can be coupled with EM-CCDs to improve energy resolution. The semiconductor route allows for even higher energy resolution than that offered by scintillators such as $LaBr_3(Ce)$. This is particularly important when analyzing nuclear fuel emission spectra which contains multiple energy peaks, some in close proximity to each other in energy. Direct conversion in a semiconductor is also advantageous as it obviates the intermediate step of converting particle energy into light. Light spread reduces spatial resolution as the width of the scintillator crystal increases. Thus, there is an inherent tradeoff between spatial resolution and efficiency, particularly for high energy photopeaks. Given these technical considerations, a pixelated CZT was used in this analysis.

2. PROPOSED DESIGN

The present design is an evolution from previous designs. The first incorporated a 200 μm tungsten pencil beam collimator, similar to those used in full assembly or full element tomography except smaller in size and higher in spatial resolution. In previous work, it was found that a pencil beam collimator is likely infeasible as the predicted count rate was found to be too low to permit rapid acquisition given the expected activity of fuel rodlets [8]. A pinhole collimator was therefore proposed to increase the field of view and thereby increase the sampled activity. This also simplifies some of the manipulation requirements for the fuel goniometer. With a pinhole collimator, however, a spatially and energy resolved detector is required. Two detector types were considered. In the first, a LaBr$_3$(Ce) scintillator detector is coupled with an EM-CCD. In the second, a pixelated CZT detector is used. As explained in the introduction the CZT was ultimately chosen for reasons of spectral and spatial resolution. The emission system is shown in Figure 1.
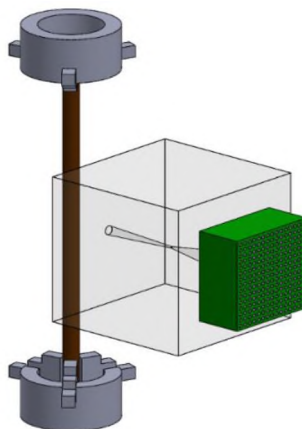

Figure 1: Emission tomography design (not modelled to scale). Gamma rays emitted from the fuel rodlet (cylinder) pass through a tungsten pinhole aperture (grey cube) and into a pixelated array of CZT detectors

3. METHODOLOGY

To model the gamma source used for emission tomography, a fission product gamma spectrum was simulated using fuel depletion program ORIGEN within the SCALE 6.2 package [9]. ORIGEN was used to simulate a 17×17 pressurized water reactor (PWR) fuel assembly with 6% ^{235}U enrichment and a power history typical for the Advanced Test Reactor (ATR). The fuel was subject to irradiation cycles of 55 days at 22.5 MW, and decay times of 22 days. The gamma spectrum was binned from 0 MeV to 20 MeV with 3000 energy bins spaced 6.67 keV apart. The resulting gamma spectrum data was divided by the total intensity of photon emission to acquire a probability of emission. A total burnup of 18.5 GWd was assumed corresponding to a total irradiation time of 825 days. Further explanation of the source methodology can be found in Kilby *et al.* [8].

Burnup calculations were performed on a per metric ton uranium (MTU) basis. The total activity of the simulated assembly was multiplied by the MTU fraction within the ATR test fuel rodlet to approximate its activity. MCNP 6.1 was used along with the burnup predictions to perform transport calculations and predict the detector response for a CZT detector [10]. Tungsten pinhole collimators with various acceptance angles and 100 μm aperture diameter were included in order to optimize spatial resolution and count rate.

The determination of the spatial resolution of the detector considered two contributions. The first is the contribution from the collimator. The collimator resolution contribution, R_c, can be approximated with Equations 1-2

$$R_c = \frac{a + Z}{a} d_e \tag{1}$$

$$d_e = \left[d \left(d + 2\mu^{-1} \tan \frac{\alpha}{2} \right) \right]^{\frac{1}{2}} \qquad (2)$$

the collimator resolution is dependent on the diameter of the aperture (d), the mean free path of the photon (μ^{-1}), the distance from object to aperture (Z), the distance from aperture to detector (a), and the acceptance angle (α).

The second contribution to the resolution is the intrinsic resolution of the CZT detector. This is determined by the pixel size, pixel quantity, and the magnification factor. The pixel size can impact the spatial resolution in a few ways. One, the photons can scatter out of the pixel and into another. Two, the pixel size is too small, there is spillover of charge carriers between adjacent pixels. The total system resolution includes contributions from the collimator (R_c), the detector (R_i), and scattering (R_s).

$$R_0 = \sqrt{R_c^2 + \left(\frac{Z}{a} \right) R_i^2 + R_s^2} \qquad (3)$$

To predict the count rate and emission spectrum, a pulse height (F8) tally was included in the MCNP model within the CZT detector volume.

4. RESULTS

With a pinhole collimator with an acceptance angle of 5°, the total count rate per second is 7.30×10^4. A representative emission spectrum is shown in Figure 2. The 5° acceptance angle is able to adequately minimize Compton scatter into the detector allowing for clear identification of seven strong photopeaks. While count rate is an important parameter in determining the speed of image acquisition, the resolution contribution from

the pinhole is important in determining the spatial resolution of the associated image. For a pinhole with a fixed diameter of 100 micron and a fixed angle of 5°, the collimator resolution is solely determined by the photon energy.
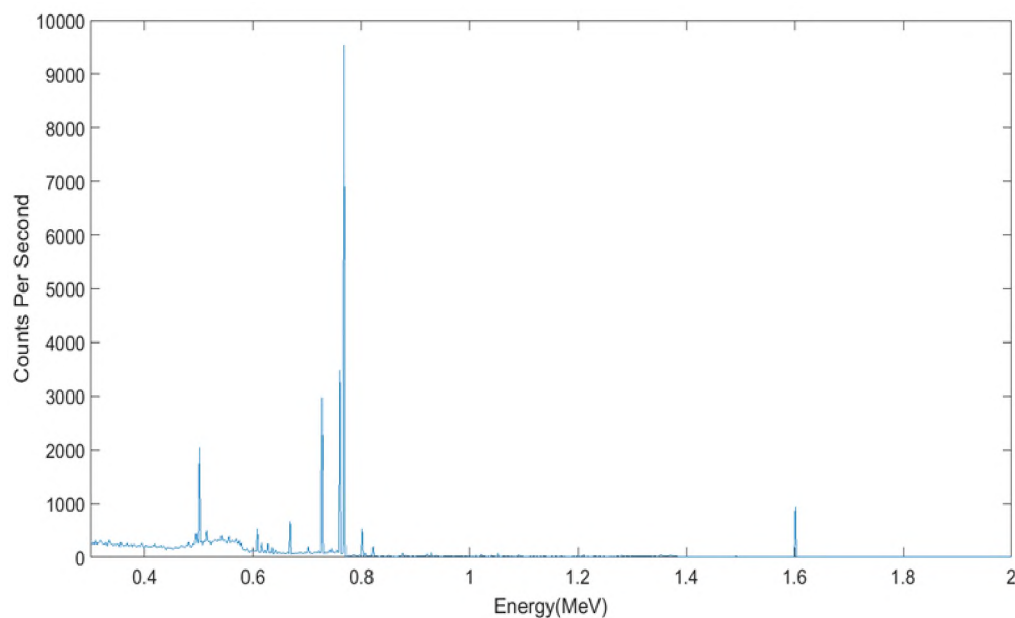
Figure 2: Gamma-ray emission spectrum collected with a 5° tungsten pinhole aperture and CZT detector

Within energy range of 600 to 800 keV, where the majority of the most intense photopeaks lay, the collimator resolution component was found to be 270-300 micron. This is adequate for sub-mm spatial imaging though further improvement in the spatial resolution is possible by reducing the diameter of the pinhole aperture. Reduced aperture size comes at the cost of reduced count rates.

ACKNOWLEDGEMENTS

REFERENCES

1. Jacobsson S, Bäcklin A, Håkansson A, P Jansson (2000) A tomographic method for experimental verification of the integrity of spent nuclear fuel. Appl Radiat Isotopes. 53:681–689

2. Jacobsson S, Håkansson A, Jansson P, Bäcklin A (2001) A tomographic method for verification of the integrity of spent nuclear fuel assemblies - II: Experimental investigation. Nucl Technol. 135

3. Jacobsson S, Håkansson A, Bäcklin A, Jansson P, Osifo O, Willman C (2006) Tomography for partial-defect verification : experiences from measurements using different devices ESARDA Bulletin. 33:15–25

4. Lundqvist T, Jacobsson S, Håkansson A (2007) SPECT imaging as a tool to prevent proliferation of nuclear weapons. Nucl. Instruments Meth A. 580:843–847

5. Jacobsson S, Lundqvist T, Håkansson A (2008) Verification of completeness of spent nuclear fuel assemblies by means of tomography. PHYSOR 08 4:3131–3137

6. Parker H, Joyce M (2015) The use of ionising radiation to image nuclear fuel: A review. Prog Nucl Energy. 85:297–318

7. M. Korevaar, J. Heemskerk, M. Goorden and F. Beekman, "Multi-scale algorithm for improved scintillation detection in a CCD-based gamma camera", *Physics in Medicine and Biology*, vol. 54, no. 4, pp. 831-842, 2009. Available: 10.1088/0031-9155/54/4/001.

8. S. Kilby et al., "A source biasing and variance reduction technique for Monte Carlo radiation transport modeling of emission tomography problems", *Journal of Radioanalytical and Nuclear Chemistry*, vol. 320, no. 1, pp. 37-45, 2019. Available: 10.1007/s10967-019-06457-1.

9. Rearden B, Jessee M (2016) "SCALE Code System." RSICC, Oak Ridge

10. Goorley T. et al. (2012) Initial MCNP6 release overview. Nucl Technol 180:298–315

SECTION

3. DESIGN OF A FUEL PHANTOM FOR A HIGH-RESOLUTION EMISSION GAMMA RAY TOMOGRAPHY SYSTEM USING A PIXELATED CZT DETECTOR

3.1. PROPOSED DESIGN

The present design is based off of the design outlined in Paper III. Initially, a 200-micron tungsten pencil-beam collimator was investigated, similar to those used in full assembly or full element tomography, though smaller in size and offering higher spatial resolution. Previous work found the predicted count rate utilizing a pencil-beam collimator was too low to permit rapid acquisition, given the expected activity of the fuel rodlet [99]. A pinhole collimator was therefore proposed to increase the field of view, thereby increasing the sampled activity, but also simplifying some of the manipulation requirements for the fuel goniometer. With a pinhole collimator, however, a spatially and energy resolved detector is required. Two detector types were considered. Initially, a $LaBr_3(Ce)$ scintillator detector was coupled with an electron-multiplying charge-coupled device. A pixelated CZT detector was ultimately chosen for its higher spectral and spatial resolution. The emission detection system modelled is the same system outlined in Paper III.

3.2. METHODS

To model the gamma source used for emission tomography, a fission product gamma spectrum was simulated using the fuel depletion program ORIGEN, within the SCALE 6.2 package [90]. ORIGEN was used to simulate a 17×17 pressurized water reactor

(PWR) fuel assembly with 6% U-235 enrichment and a power history typical for the ATR. The fuel was subject to irradiation cycles of 55 days at 22.5 MW and 22-day decay periods. The gamma spectrum was partitioned from 0 MeV to 20 MeV with 3000 energy bins spaced 6.67 keV apart. The resulting gamma spectrum data was divided by the total intensity of photon emission to acquire a probability of emission. A total burnup of 18.5 GWd was selected due to asymptotic creation of fission products, corresponding to a total irradiation time of 825 days.

Burnup calculations were performed on a per metric ton uranium (MTU) basis. The total activity of the simulated assembly was multiplied by the MTU fraction within the ATR test fuel rodlet to approximate its activity. MCNP 6.2 was used along with the burnup predictions to perform transport calculations and predict the detector response for a CZT detector [10]. Tungsten pinhole collimators with various acceptance angles and a 100 μm aperture diameter were examined to optimize spatial resolution and count rate.

To model the pixelated CZT response, a volume-averaged cell flux mesh was used to define the detector pixilation. The source points were distributed uniformly throughout the fuel cylinder. One transport simulation, with an energy cutoff (ECUT) card, removes photons from the simulation upon falling below 600 keV, effectively tallying the signal photons and removing scattering noise. This was used as a rough approximation to understand the nature of scattering within the CZT medium. Another simulation, without the ECUT card, allows for inter-pixel scattering and includes the scattering contribution.

3.3. PRELIMINARY RESULTS

The data acquired from the above simulation methodologies yields three main results. A Eu-154 distribution that demonstrates the efficacy of the imaging grid and the effect of interpixel scattering. A Cs-137 distribution that demonstrates the quantity of activity density that is needed to contrast the phantom from the fuel matrix. The Cs-137 distribution is also used in a rotation scheme to demonstrate rotational efficacy of radiographic projections of the nuclear fuel.

3.3.1. Eu-154 Spatially Uniform Distribution Results. The tally results of the first simulation (with an ECUT card) represent the signal from photons that are within the energy regime of interest. The roughly uniform distribution of signal reflects the spatially uniform distribution of Eu-154 in ceramic fuels. There is a decrease in signal on the periphery of the Y-axis due to the projection of a cylindrical fuel phantom onto an array of square pixels. A plot of this signal is given in Figure 3.1.
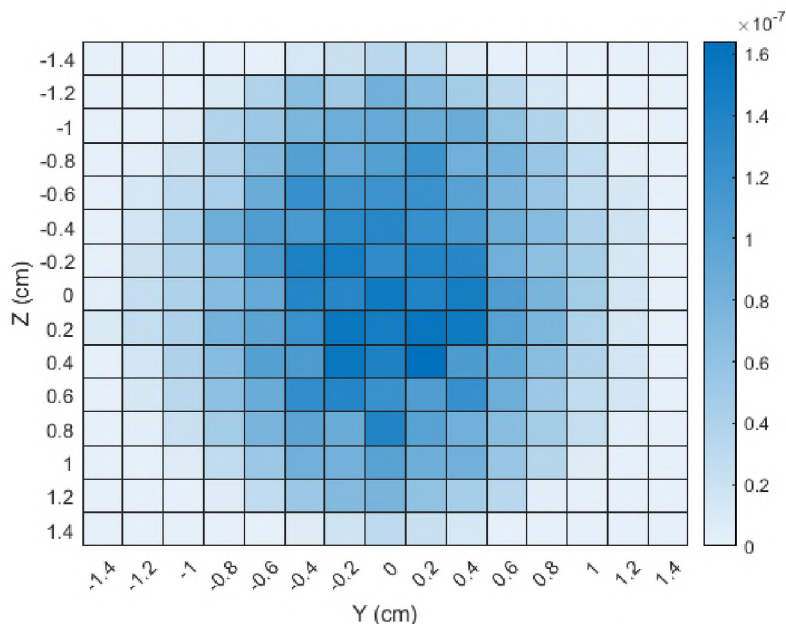
Figure 3.1: Signal per source particle source photons in a pixelated CZT array

Subtracting the tally results of the first simulation from those of the second (that without an ECUT card), a representation of the signals from photons that scatter into neighboring pixels results. Figure 3.2 depicts a line scan of the central pixels on the y-axis.
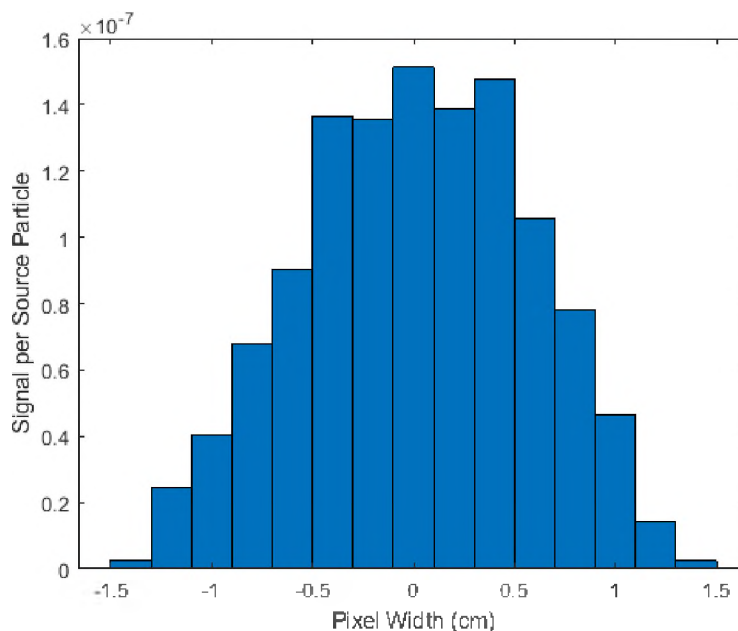
Figure 3.2: Line scan of the central pixels along the y-axis at Z=0

Since the distribution of the fission products is uniform, the expected result of a line scan about the y axis would be a semicircular distribution. Any deviation from a perfect semicircular can most likely be explained by interpixel scattering in the medium. However, due to the Monte Carlo process, there is the introduction of simulation error, and with larger particle history counts, the simulation error contribution will continue to decrease. While this is a problem, the general semicircular shape is still achieved. The contribution from the scattered photons in each pixel can be seen in Figure 3.3.
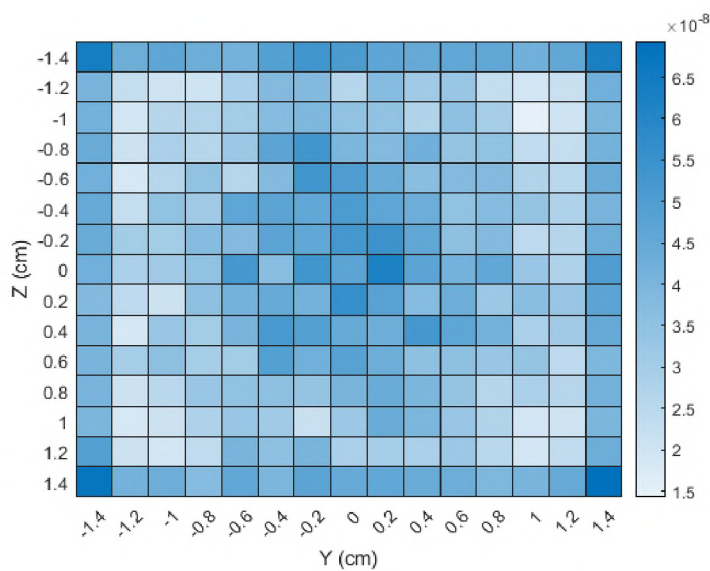
Figure 3.3: Signal per source particle due to scattered photons in each pixel volume

The scattered photons represent a nontrivial number of excess photons. CZT is a highly scattering medium, increasing the probability of scatter in each pixel within the array. The corner and outer pixels contain a significant number of scattered particles. The inner pixels in the array contain non-negligible scattering contributions as well, but increased signal in the inner pixels necessitates a comparison of scattered photons and signal photons to definitively examine the detector performance.

3.3.2. Cs-137 Activity Density and Radiographic Projections. In addition to the Eu-154 distribution a Cs-137 phantom is created to determine the ability for the pixelated array to spatially resolve activity data on the phantom. The phantom uses a localized sub-volume cylinder of Cs-137 which was shown in Figure 2.6; the radius of the phantom is 0.05 cm, and the height is 0.4 cm. To determine the activity density, simulations were conducted to determine the emission probabilities needed to contrast the phantom from the fuel medium. Emission probability represents the probability that a photon is generated in

a volume. For example, if there is an emission probability of 5% in the phantom, then the phantom will produce 5 photons in its volume per 100 photons generated. The results are shown in Figure 3.4.
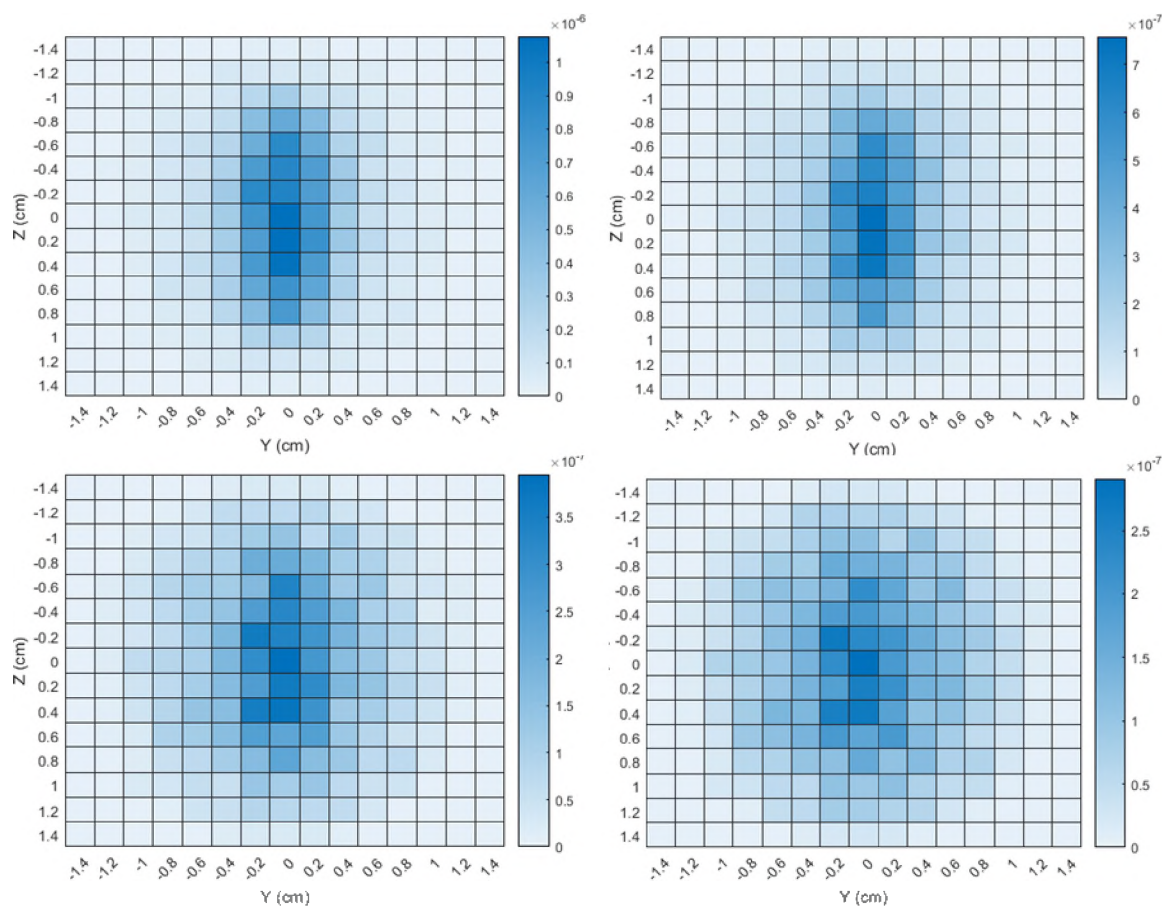
Figure 3.4: Emission probabilities of 8% (upper left), 5% (upper right), 2% (lower left), and 1% (lower right) of Cs-137 at a 0° rotation. Signal is normalized per particle history

From Figure 3.4, the phantom becomes indistinguishable from the rest of the fuel material between 5% and 2% emission probability. Therefore, for the radiographic angle dependent simulations an emission probability of 5% is used. The phantom is rotated, and

radiographic projections can be acquired at each rotation angle. The rotations are shown

relative to collimator and detector in Figure 3.5.
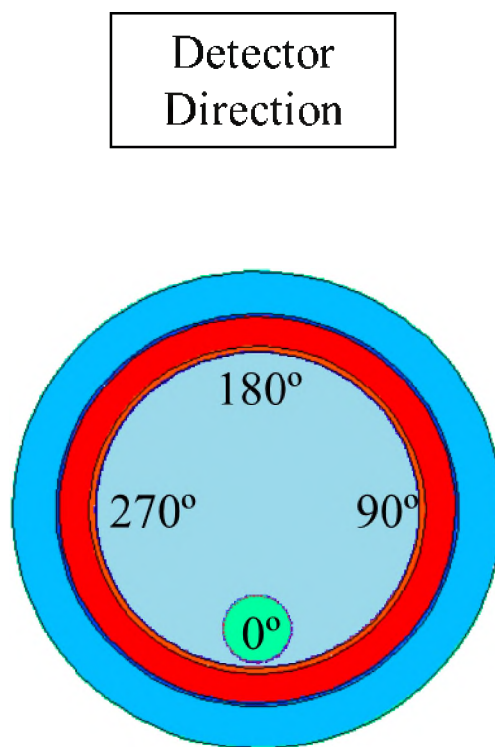
Figure 3.5: 4 rotational angles that establish a relative rotation pattern for the phantom (green cylinder) in 90° increments relative to the detector direction

From Figure 3.5, 0° represents the furthest distance from the detector while being

within line of sight. 180° represents the closest that the phantom will be toward the detector.

90° and 270° represent the rotation angles with the most optically tenuous path for photons

to travel due to the phantom existing near the conical peripheries of the field of view.

Photons that do impinge on the detector generally do so with significant scattering

contributions as well. Essentially, the phantom, at those angles, has the least direct

sampling of any angle in the circle. Therefore, scattering is likely to be high. The normalized photon flux at 4 angle increments is shown in Figure 3.6
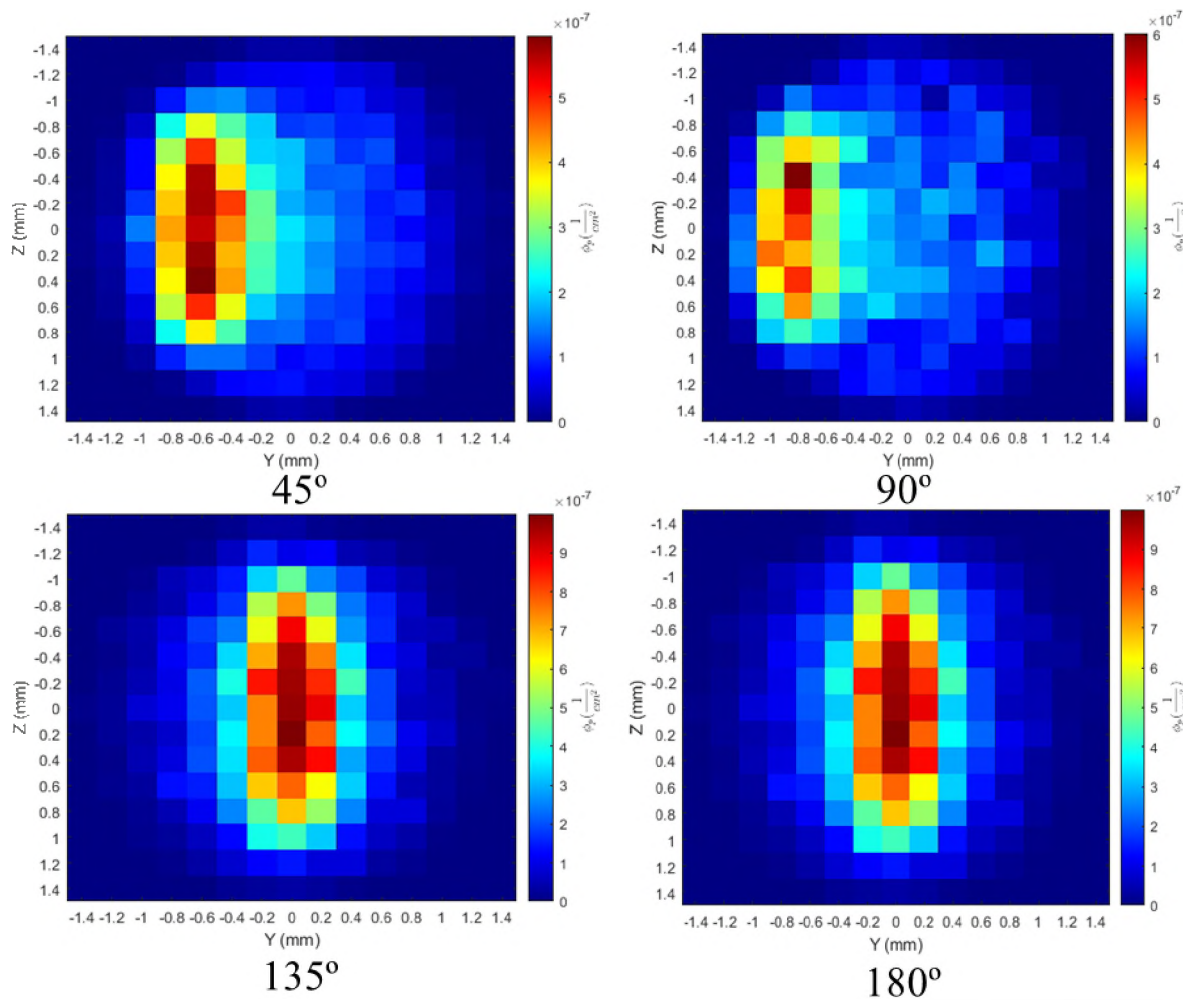
Figure 3.6: Radiographic projections using an MCNP normalized photon flux ($\frac{1}{cm^2}$) of a Cs-137 phantom at stated angles. 180° represents the closest point for the phantom relative to the detector system

Since the fuel phantom, is symmetrical each of these projections can be mirrored. For example, 90° rotation is a reflection of 270° about the y axis. Therefore, projections taken from 0-180° represents a mirrored reflection of 180-360°. This significantly reduces

the computational time required to acquire a 360° sampled data set. The final objective for these radiographs is to apply an algorithm to create a 2D reconstruction of the fuel volume.

4. CONCLUSIONS AND RECOMMENDATIONS

4.1. CONCLUSIONS

To summarize the work accomplished, a series of objectives was created. In paper I, a radiation transport methodology was developed to increase the efficiency of simulating transport behavior in a high aspect ratio pencil beam collimator for the proposed detection geometry of a submersible gamma tomography system. A semi-analytic method provided computational savings on the order of 10^7 with a less than 20% reduction in count rates in the prominent photopeaks. Paper II compared this developed radiation transport methodology to three different subcategories of Monte Carlo variance reduction techniques. A comparison made between population control, DXTRAN, and modified sampling methods yielded computational savings on the order of 10^{14} for 1 mm aperture sizes at the expense of 18% fewer counts registered in the photopeak bins. The DXTRAN and geometry splitting methods yielded computational savings of 10^0-10^1 maintaining simulation accuracy.

The conclusion from Paper I is that the count rates are too low for fast data acquisition of gamma emission data. Therefore, in Paper III, a pinhole collimator coupled with a CZT detector is designed. The count rates between 10^2-10^3 in the photopeaks represent a significant increase over the 6 cps over the entirety of the photon spectrum in the parallel beam collimator case. The 1D spatial resolution was calculated to be between

414-565 micron depending on the energy of the incident photon. This collimator design is implemented in Section 3 to determine radiographic projections of a Cs-137 fuel phantom and a uniform Eu-154 distribution. For the Eu-154 distribution, a spatially uniform sampling was modelled in the MCNP input file and this resulted in a semi-circular distribution. By examining the line scan of a series of pixels on the grid, any deviation from a semi-circular distribution can be attributed to photon scattering between pixels. The Cs-137 fuel phantom was created and a study on the emission probability required to contrast the phantom from the nuclear fuel was conducted. Between 2-5% emission probability yielded the lowest emission probabilities that still yielded enough contrast to visually distinguish between the phantom and the fuel capsule. Therefore, for the sake of modelling, a 5% emission probability was used to produce radiographic projections. The phantom was then transformed to produce 2D radiographic projections on the detector grid. Through the use of more angular projections, it is possible to reconstruct an image from the scans.

4.2. RECOMMENDATIONS

In designing a small submersible gamma tomography system, a few recommendations can be made based on the results from this dissertation. First, for radiation transport methodologies that rely on high aspect ratio pencil beam collimators, there is not a better inbuilt Monte-Carlo variance reduction methodology than the developed semi-analytic method in Paper I. In place of a semi-analytic methodology, an inbuilt source bias correction can be used. However, this does not take full advantage of the figure of merit increase that the semi-analytic method provides. Since source biasing requires sampling from a biased probability density function, the results of a source biased

run are then corrected by MCNP before outputting the results in the tally. Thus, removing a process that happens internally within MCNP is likely to increase computational efficiency. Compared to the other variance reduction techniques outlined in Paper II, the semi-analytic method proved again to yield superior computational savings at the expense of approximately 18% fewer photopeak counts per bin across all photopeaks. Overall, this system had too high an aspect ratio to generate a spectrum quickly. A few ways to mitigate the low count rate that the parallel beam collimator detector system yields would be to change the surrounding water medium to a material such as air to reduce attenuation, and to increase fuel activity through the use of more fuel or longer irradiation times at higher powers.

The design of the pinhole collimator detection system was the result of the failure of the parallel beam collimator to yield sufficient count rates (on the order of 10^2 cps). By taking advantage of an acceptance angle, the sampled fuel activity increases. Initially, this system attempted to utilize a $LaBr_3(Ce)$ coupled with an EM-CCD. This was found in literature to degrade energy resolution by 34-65% at 141 keV. For gamma emission tomography applications, a degradation of that magnitude would lead to summation. It could be possible to optimize the thickness of a high energy resolution scintillator and combine the EM-CCD with a series of SiPMs to increase the energy resolution. At energies between 600 keV-1.6 MeV, this system could improve energy resolution. The main benefit of these systems is the spatial resolution capabilities. However, the detector does have to be optimally thick for individual cases. For example, a scintillator that detects 141 keV photons cannot be the same thickness as a scintillator that would detect 662 keV photons. Energy resolution would suffer, or the interaction probability would be too low at higher

energies. The design choice to mitigate the energy resolution loss was to implement a high energy resolution pixelated CZT, but this has worse spatial resolution capabilities. There is generally a tradeoff between these parameters, and as such, a well-designed system will be optimized for a specific energy application.

The pixelated CZT detection system with 2 mm pixel width is a promising compromise between EM-CCDs and scintillation detectors. The energy resolution is high for these compound semiconductors, and the pixelated grid provides reasonable detector spatial resolution combined with the collimator spatial resolution (414-565 microns from 0-2 MeV). Reducing the pixel size to 1 mm will yield better total system resolution (231-450 microns). However, a study done on the interpixel scattering of incident photons would be required to determine if the reduction in surface area leads to an unacceptable contribution of scattered photons to the per pixel signal. It does seem reasonable that a pixelated CZT detector would provide the necessary detection capabilities for a system such as the one outlined in this dissertation. The detection system has the ability to spatially resolve radiographic projections at varying angles. However, it would be more advantageous to model the signal and radiographic projections using a program such a GEANT 4 as there are more inbuilt capabilities for imaging applications [100].

BIBLIOGRAPHY

[1] H. M. O. D. Parker and M. J. Joyce, "The use of ionising radiation to image nuclear fuel: A review," *Prog. Nucl. Energy*, vol. 85, pp. 297–318, 2015.

[2] R. Yasuda *et al.*, "Application of neutron imaging plate and neutron CT methods on nuclear fuels and materials," *IEEE Trans. Nucl. Sci.*, vol. 52, no. 1 II, pp. 313–316, 2005.

[3] P. Hausladen, M. Blackston, E. Brubaker, D. Marleau, and R. P Newby, "Demonstration of Computed Tomography to Count Fuel Pins," 2012.

[4] W. K. Kim, Y. W. Lee, M. S. Cho, J. Y. Park, S. W. Ra, and J. B. Park, "Nondestructive measurement of the coating thickness for simulated TRISO-coated fuel particles by using phase contrast X-ray radiography," *Nucl. Eng. Des.*, vol. 238, no. 12, pp. 3285–3291, 2008.

[5] M. Mayorov *et al.*, "Gamma Emission Tomography for the Inspection of Spent Nuclear Fuel," *2017 IEEE Nucl. Sci. Symp. Med. Imaging Conf. NSS/MIC 2017 - Conf. Proc.*, pp. 17–18, 2018.

[6] International Atomic Energy Agency, "INFCIRC/140 - Treaty on the Non-Proliferation of Nuclear Weapons," *Int. At. Energy Agency*, no. April, pp. 1–4, 1970.

[7] T. Honkamaa, F. Levai, A. Turunen, B. Reinhard, S. Vaccaro, and P. Schwalback, "A prototype for passive gamma emission tomography," *IAEA Safeguards Symp.*, no. August 2015, p. 440, 2014.

[8] International Atomic Energy Agency (IAEA), "Model Protocol Additional to the Agreement(s) between State(s) and the International Atomic Energy Agency for the Application of Safeguards, INFCIRC/540," vol. 540, 1997.

[9] K P Ziock et al, "Radiation Imaging of Dry Storage Casks for Spent Nuclear Fuel," pp. 1–5, 2005.

[10] B. K. Barnes, J. R. Phillips, G. R. Waterbury, J. N. Quintana, J. R. Netuschil, and A. S. Murray, "Characterization of Irradiated Nuclear Fuels by Precision Gamma Scanning," *J. Nucl. Mater.*, vol. 81, pp. 177–184, 1979.

[11] J. Ely, R. Kouzes, J. Schweppe, E. Siciliano, D. Strachan, and D. Weier, "The use of energy windowing to discriminate SNM from NORM in radiation portal monitors," *Nucl. Instruments Methods Phys. Res. Sect. A Accel. Spectrometers, Detect. Assoc. Equip.*, vol. 560, no. 2, pp. 373–387, 2006.

[12] R. Hevener, M. S. Yim, and K. Baird, "Investigation of energy windowing algorithms for effective cargo screening with radiation portal monitors," *Radiat. Meas.*, vol. 58, pp. 113–120, 2013.

[13] P. Andersson and S. Holcombe, "A computerized method (UPPREC) for quantitative analysis of irradiated nuclear fuel assemblies with gamma emission tomography at the Halden reactor," *Ann. Nucl. Energy*, vol. 110, pp. 88–97, 2017.

[14] P. Andersson, S. Holcombe, and T. Tverberg, "Inspection of a LOCA test rod at the halden reactor project using gamma emission tomography," in *Top Fuel 2016: LWR Fuels with Enhanced Safety and Performance*, 2016.

[15] S. Jacobsson Svärd, S. Holcombe, and S. Grape, "Applicability of a set of tomographic reconstruction algorithms for quantitative SPECT on irradiated nuclear fuel assemblies," *Nucl. Instruments Methods Phys. Res. Sect. A Accel. Spectrometers, Detect. Assoc. Equip.*, vol. 783, pp. 128–141, May 2015.

[16] C. Hellesen, S. Grape, P. Jansson, S. Jacobsson Svärd, M. Åberg Lindell, and P. Andersson, "Nuclear spent fuel parameter determination using multivariate analysis of fission product gamma spectra," *Ann. Nucl. Energy*, vol. 110, 2017.

[17] T. Lundqvist, S. Jacobsson Svärd, and A. Håkansson, "SPECT imaging as a tool to prevent proliferation of nuclear weapons," *Nucl. Instruments Methods Phys. Res. Sect. A Accel. Spectrometers, Detect. Assoc. Equip.*, vol. 580, no. 2, pp. 843–847, 2007.

[18] S. Jacobsson, A. Bäcklin, A. Håkansson, and P. Jansson, "A tomographic method for experimental verification of the integrity of spent nuclear fuel," *Appl. Radiat. Isot.*, vol. 53, no. 4–5, pp. 681–689, 2000.

[19] S. Caruso, M. F. Murphy, F. Jatuff, and R. Chawla, "Nondestructive determination of fresh and spent nuclear fuel rod density distributions through computerised gamma-ray transmission tomography," *J. Nucl. Sci. Technol.*, vol. 45, no. 8, pp. 828–835, 2008.

[20] S. Caruso, M. F. Murphy, F. Jatuff, and R. Chawla, "Determination of within-rod caesium and europium isotopic distributions in high burnup fuel rods through computerised gamma-ray emission tomography," *Nucl. Eng. Des.*, vol. 239, no. 7, pp. 1220–1228, 2009.

[21] J. E. Gillam and M. Rafecas, "Monte-Carlo simulations and image reconstruction for novel imaging scenarios in emission tomography," *Nucl. Instruments Methods Phys. Res. Sect. A Accel. Spectrometers, Detect. Assoc. Equip.*, vol. 809, 2016.

[22] A. Davour *et al.*, "Applying image analysis techniques to tomographic images of irradiated nuclear fuel assemblies," *Ann. Nucl. Energy*, vol. 96, pp. 223–229, 2016.

[23] T. A. Holly *et al.*, "Single photon-emission computed tomography," *J. Nucl. Cardiol.*, vol. 17, no. 5, pp. 941–973, 2010.

[24] J. MacHac, "Cardiac positron emission tomography imaging," *Semin. Nucl. Med.*, vol. 35, no. 1, pp. 17–36, 2005.

[25] S. T. Hsue, T. W. Crane, W. L. Talbert, Jr, and J. C. Lee, "Nondestructive Assay Methods for Irradiated Nuclear Fuels," no. January, 1978.

[26] J. H. Jubbell and S. M. Seltzer, "Tables of X-Ray Mass Attenuation Coefficients and Mass Energy-Absorption Coefficients," 2004. .

[27] S. Holcombe, S. Jacobsson Svärd, and L. Hallstadius, "A Novel gamma emission tomography instrument for enhanced fuel characterization capabilities within the OECD Halden Reactor Project," *Ann. Nucl. Energy*, vol. 85, pp. 837–845, 2015.

[28] H. Wieczorek, A. Goedicke, F. Edström, C. Degenhardt, H. Botterweck, and R. Bippus, "Collimator Spatial Resolution Photon Emission Computed Tomography has been," *Ieee Nucl. Sci. Symp. Conf. Rec.*, pp. 1717–1721, 2005.

[29] F. van der Have *et al.*, "U-SPECT-II: An Ultra-High-Resolution Device for Molecular Small-Animal Imaging," *J. Nucl. Med.*, vol. 50, no. 4, pp. 599–605, 2009.

[30] T. U. Delft and R. M. Prof, *High-resolution EM-CCD scintillation gamma cameras.* 2013.

[31] E. Ccd *et al.*, "Photon-Counting Gamma Camera Based on an," vol. 52, no. 3, pp. 580–588, 2005.

[32] T. S. Suh and Y. Whee Bahk, "Appendix: Basic Physics of Pinhole Scintigraphy," *Basic Phys. Pinhole Scintigr.*, pp. 227–236.

[33] K. Ogawa, T. Kawade, K. Nakamara, A. Kubo, and T. Ichihara, "Ultra high resolution pinhole SPECT for small animal study.," *IEEE Trans. Nucl. Sci.*, vol. 45, no. 6, pp. 3122–3126, 1998.

[34] S. Aldawood *et al.*, "Comparative Characterization Study of a LaBr3(Ce) Scintillation Crystal in Two Surface Wrapping Scenarios: Absorptive and Reflective," *Front. Oncol.*, vol. 5, no. December, pp. 1–9, 2015.

[35] R. J. Jaszczak, J. Li, E. L. Johnson, and H. Wang, "Physics in Medicine & Biology Related content Pinhole collimation for ultra-high-resolution , small- field-of-view SPECT," 1994.

[36] J. A. Sorenson and M. E. Phelps, "The Anger Camera: Performance Characteristics," *Phys. Nucl. Med.*, pp. 331–345, 1987.

[37] R. Accorsi and S. D. Metzler, "Analytic determination of the resolution-equivalent effective diameter of a pinhole collimator," *IEEE Trans. Med. Imaging*, vol. 23, no. 6, pp. 750–763, 2004.

[38] G. F. Knoll and H. W. Kraner, *Radiation Detection and Measurement*, Fourth Edi., vol. 69, no. 4. Don Fowley, 1981.

[39] M. J. Weber, "Inorganic scintillators: Today and tomorrow," *J. Lumin.*, vol. 100, no. 1–4, pp. 35–45, 2002.

[40] H. Sadrozinski, "Particle Detector Applications in Medicine," *Nucl. Inst. Methods Phys. Res. A*, vol. 23, no. 1, pp. 1–7, 2011.

[41] P. R. Menge, G. Gautier, A. Iltis, C. Rozsa, and V. Solovyev, "Performance of large lanthanum bromide scintillators," *Nucl. Instruments Methods Phys. Res. Sect. A Accel. Spectrometers, Detect. Assoc. Equip.*, vol. 579, no. 1, pp. 6–10, 2007.

[42] P. Lecoq, "Development of new scintillators for medical applications," *Nucl. Instruments Methods Phys. Res. Sect. A Accel. Spectrometers, Detect. Assoc. Equip.*, vol. 809, pp. 130–139, 2016.

[43] S. Sajedi *et al.*, "Design and development of a high resolution animal SPECT scanner dedicated for rat and mouse imaging," *Nucl. Instruments Methods Phys. Res. Sect. A Accel. Spectrometers, Detect. Assoc. Equip.*, vol. 741, pp. 169–176, 2014.

[44] G. Hesz, Szlávecz, K. Kovács, and B. Benyó, "Investigation of 3D SPECT reconstruction with multi-energy photon emitters 1," *IFAC-PapersOnLine*, vol. 28, no. 20, pp. 30–35, 2015.

[45] C. Diaz-Ledezma, C. Lamberton, P. Lichstein, and J. Parvizi, "Diagnosis of Periprosthetic Joint Infection: The Role of Nuclear Medicine May Be Overestimated," *J. Arthroplasty*, vol. 30, no. 6, pp. 1044–1049, 2015.

[46] G. Cinelli, L. Tositti, D. Mostacci, and J. Baré, "Calibration with MCNP of NaI detector for the determination of natural radioactivity levels in the field," *J. Environ. Radioact.*, vol. 155–156, pp. 31–37, 2016.

[47] C. Rozsa and P. Menge, "Efficiency Calculations for Selected Scintillators," *Doc. from Saint-Gobain website*, 2004.

[48] B. Aleandrov, J. Audia, M. Browne, K. Ianakiev, H. Hguyen, and P. Reass, "Temperature compensation of NaI(TI) scinitillator detectors," in *Insititute of Nuclear Material Management*, 2005.

[49]   St. Gobain, "Lanthanum Bromide and Enhanced Lanthanum Bromide." [Online].
         Available:https://www.crystals.saintgobain.com/sites/imdf.crystals.com/files/docu
         ments/lanthanum-material-data-sheet.pdf.

[50]   M. A. N. Korevaar, M. C. Goorden, and F. J. Beekman, "Cramer-Rao lower bound
         optimization of an EM-CCD-based scintillation gamma camera," *Phys. Med. Biol.*,
         vol. 58, no. 8, pp. 2641–2655, 2013.

[51]   S. Salvador *et al.*, "Improved EMCCD gamma camera performance by SiPM pre-
         localization," *Phys. Med. Biol.*, vol. 57, no. 22, pp. 7709–7724, 2012.

[52]   J. W. T. Heemskerk *et al.*, "Experimental comparison of high-density scintillators
         for EMCCD-based gamma ray imaging," *Phys. Med. Biol.*, vol. 57, no. 14, pp.
         4545–4554, 2012.

[53]   M. A. N. Korevaar, M. C. Goorden, J. W. T. Heemskerk, and F. J. Beekman,
         "Maximum-likelihood scintillation detection for EM-CCD based gamma cameras,"
         Phys. Med. Biol., vol. 56, no. 15, pp. 4785–4801, 2011.

[54]   J. W. T. Heemskerk *et al.*, "An enhanced high-resolution EMCCD-based gamma
         camera using SiPM side detection," *Phys. Med. Biol.*, vol. 55, no. 22, pp. 6773–
         6784, 2010.

[55]   M. A. N. Korevaar, J. W. T. Heemskerk, and F. J. Beekman, "A pinhole gamma
         camera with optical depth-of-interaction elimination," *Phys. Med. Biol.*, vol. 54, no.
         13, 2009.

[56]   e2v, "CCD97-00 Back Illuminated 2-Phase IMO Series Electron Multiplying CCD
         Sensor," 2004.

[57]   R. Wojcik, "High spatial resolution gamma imaging detector based on a 5″ diameter
         r3292 hamamatsu pspmt," *IEEE Trans. Nucl. Sci.*, vol. 45, no. 3 PART 1, pp. 487–
         491, 1998.

[58]   R. S. Miyaoka, S. G. Kohlmyer, and T. K. Lewellen, "Performance characteristics
         of a second generation micro crystal element (MiCE2) detector," *IEEE Nucl. Sci.
         Symp. Med. Imaging Conf.*, vol. 2, no. 4, pp. 1124–1127, 2001.

[59]   P. D. Oleott, F. Habte, A. M. Foudray, and C. S. Levin, "Performance
         characterization of a miniature, high sensitivity gamma ray camera," *IEEE Trans.
         Nucl. Sci.*, vol. 54, no. 5, pp. 1492–1497, 2007.

[60]   C. W. Lerche *et al.*, "Depth of γ-ray interaction within continuous crystals from the
         width of its scintillation light-distribution," *IEEE Trans. Nucl. Sci.*, vol. 52, no. 3 I,
         pp. 560–572, 2005.

[61] W. C. J. Hunter, H. H. Barrett, and L. R. Furenlid, "Calibration method for ML estimation of 3D interaction position in a thick gamma-ray detector," *IEEE Trans. Nucl. Sci.*, vol. 56, no. 1, pp. 189–196, 2009.

[62] C. R. Casaccia, "Multi-PSPMT Scintillating Camera," pp. 1068–1072, 1998.

[63] Y. Hirano, T. Zeniya, and H. Iida, "Monte Carlo simulation of scintillation photons for the design of a high-resolution SPECT detector dedicated to human brain," *Ann. Nucl. Med.*, vol. 26, no. 3, pp. 214–221, 2012.

[64] J. Kim *et al.*, "Efficient design of a Ø2×2 inch NaI(Tl)scintillation detector coupled with a SiPM in an aquatic environment," *Nucl. Eng. Technol.*, vol. 51, no. 4, pp. 1091–1097, 2019.

[65] G. Bondarenko, B. Dolgoshein, V. Golovin, A. Ilyin, R. Klanner, and E. Popova, "Limited Geiger-mode silicon photodiode with very high gain," *Nucl. Phys. B - Proc. Suppl.*, vol. 61, no. 3 SUPPL., pp. 347–352, 1998.

[66] P. Buzhan *et al.*, "Silicon photomultiplier and its possible applications," *Nucl. Instruments Methods Phys. Res. Sect. A Accel. Spectrometers, Detect. Assoc. Equip.*, vol. 504, no. 1–3, pp. 48–52, 2003.

[67] D. R. Schaart *et al.*, "A novel, SiPM-array-based, monolithic scintillator detector for PET," *Phys. Med. Biol.*, vol. 54, no. 11, pp. 3501–3512, 2009.

[68] A. Owens, "Semiconductor materials and radiation detection," *J. Synchrotron Radiat.*, vol. 13, no. 2, pp. 143–150, 2006.

[69] M. E. Myronakis and D. G. Darambara, "Monte Carlo investigation of charge-transport effects on energy resolution and detection efficiency of pixelated CZT detectors for SPECT/PET applications," *Med. Phys.*, vol. 38, no. 1, pp. 455–467, 2011.

[70] S. D. Chun *et al.*, "Property of a CZT semiconductor detector for radionuclide identification," *J. Nucl. Sci. Technol.*, vol. 45, pp. 421–424, 2008.

[71] L. C. Johnson, D. L. Campbell, E. L. Hull, and T. E. Peterson, "Characterization of a high-purity germanium detector for small-animal SPECT," *Phys. Med. Biol.*, vol. 56, no. 18, pp. 5877–5888, 2011.

[72] R. Rahman, A. J. Plater, P. J. Nolan, and P. G. Appleby, "Assessing czt detector performance for environmental radioactivity investigations," *Radiat. Prot. Dosimetry*, vol. 154, no. 4, pp. 477–482, 2013.

[73] W. L. Duvall *et al.*, "Reduced isotope dose and imaging time with a high-efficiency CZT SPECT camera," *J. Nucl. Cardiol.*, vol. 18, no. 5, pp. 847–857, 2011.

[74]   C. G. Wahl *et al.*, "Process Monitoring with High-Resolution CZT," *2017 IEEE Nucl. Sci. Symp. Med. Imaging Conf. NSS/MIC 2017 - Conf. Proc.*, pp. 2–6, 2018.

[75]   G. J. Schmid, D. A. Beckedahl, J. E. Kammeraad, J. J. Blair, K. Vetter, and A. Kuhn, "Gamma-ray Compton camera imaging with a segmented HPGe," *Nucl. Instruments Methods Phys. Res. Sect. A Accel. Spectrometers, Detect. Assoc. Equip.*, vol. 459, no. 3, pp. 565–576, 2001.

[76]   ORTEC, "Overview of Semiconductor Photon Detectors."

[77]   C. Domingo-Pardo *et al.*, "A novel γ-ray imaging method for the pulse-shape characterization of position sensitive semiconductor radiation detectors," *Nucl. Instruments Methods Phys. Res. Sect. A Accel. Spectrometers, Detect. Assoc. Equip.*, vol. 643, no. 1, pp. 79–88, 2011.

[78]   T. Steinbach *et al.*, "Compton imaging with a highly-segmented, position-sensitive HPGe detector," *Eur. Phys. J. A*, vol. 53, no. 2, 2017.

[79]   R. J. Cooper *et al.*, "SmartPET: Applying HPGe and pulse shape analysis to small-animal PET," *Nucl. Instruments Methods Phys. Res. Sect. A Accel. Spectrometers, Detect. Assoc. Equip.*, vol. 579, no. 1, pp. 313–317, 2007.

[80]   K. Taguchi and J. S. Iwanczyk, "Vision 20/20: Single photon counting x-ray detectors in medical imaging.," *Medical physics*, vol. 40, no. 10. p. 100901, 2013.

[81]   G. Montémont, S. Lux, O. Monnet, S. Stanchina, and L. Verger, "Studying spatial resolution of CZT detectors using sub-pixel positioning for SPECT," *IEEE Trans. Nucl. Sci.*, vol. 61, no. 5, pp. 2559–2566, Oct. 2014.

[82]   Y. Gu *et al.*, "Study of a high-resolution, 3D positioning cadmium zinc telluride detector for PET," *Phys. Med. Biol.*, vol. 56, no. 6, pp. 1563–1584, Mar. 2011.

[83]   S. Abbaszadeh and C. S. Levin, "3-D Position sensitive czt pet system: Current status," in *2016 IEEE Nuclear Science Symposium, Medical Imaging Conference and Room-Temperature Semiconductor Detector Workshop, NSS/MIC/RTSD 2016*, 2017, vol. 2017-Janua.

[84]   V. Ivanov, "DEVELOPMENT OF LARGE VOLUME HEMISPHERIC CdZnTe DETECTORS," no. July, 2016.

[85]   D. Goodman, J. Xia, J. Sanders, and Z. He, "FRAM v5.2 estimation of plutonium and uranium isotopics using digitized 3-D position-sensitive CdZnTe detectors," *Nucl. Instruments Methods Phys. Res. Sect. A Accel. Spectrometers, Detect. Assoc. Equip.*, no. July, pp. 2–6, 2018.

[86]   R. Redus, "Charge Trapping in XR-100T-CdTe Cadmium Telluride Detectors Application Note," 2007. [Online]. Available: https://www.amptek.com/internal-products/charge-trapping-in-xr-100t-cdte-cadmium-telluride-detectors-application-note.

[87]   D. Yuan and P. Guss, "Preliminary investigation of lanthanum-cerium bromide self-activity," in *Proceedings of SPIE - The International Society for Optical Engineering*, 2011.

[88]   P. Guss, M. Reed, and D. Yuan, "Comparison of CeBr 3 with LaBr 3 : Ce , LaCl 3 : Ce , and NaI : Tl Detectors," *Proc. SPIE*, vol. 7805, pp. 1–16, 2010.

[89]   D. Yuan, P. Guss, and S. Mukhopadhyay, "Computational removal of lanthanumcerium bromide self-activity," *Nucl. Instruments Methods Phys. Res. Sect. A Accel. Spectrometers, Detect. Assoc. Equip.*, vol. 644, no. 1, pp. 33–39, 2011.

[90]   B. T. Rearden and M. A. Jessee, *SCALE Code System*, no. 6.2.3. 2016.

[91]   J. K. Shultis and R. E. Faw, "AN MCNP PRIMER by," 2004.

[92]   M. C. Team, "MCNP-A General Monte Carlo N-Particle Transport Code, Version 5 Volume I: Overview and Theory X-5 Monte Carlo Team," 2003.

[93]   J. T. Goorley *et al.*, "MCNP6 TM USER'S MANUAL Alamos National Laboratory 2 NEN-5 Systems Design and Analysis, Los Alamos National Laboratory 3 XCP-7 Transport Applications, Los Alamos National Laboratory 4 NEN-5 Systems Design and Analysis, Los Alamos National Laboratory, contr," 2013.

[94]   T. E. Booth, "Common Misconceptions in Monte Carlo Particle Transport," 2011.

[95]   S. Kilby *et al.*, "A source biasing and variance reduction technique for Monte Carlo radiation transport modeling of emission tomography problems," *J. Radioanal. Nucl. Chem.*, Apr. 2019.

[96]   A. Davis and A. Turner, "Comparison of global variance reduction techniques for Monte Carlo radiation transport simulations of ITER," *Fusion Eng. Des.*, vol. 86, no. 9–11, pp. 2698–2700, Oct. 2011.

[97]   T. E. Booth, K. C. Kelley, and S. S. McCready, "Monte Carlo variance reduction using nested dxtran spheres," *Nucl. Technol.*, vol. 168, no. 3, pp. 765–767, 2009.

[98]   T. E. Booth, "Pulse Height Tally Variance Reduction in MCNP PULSE-HEIGHT TALLY VARIANCE REDUCTION IN MCNP," 2004.

[99]   S. Kilby *et al.*, "A source biasing and variance reduction technique for Monte Carlo radiation transport modeling of emission tomography problems," *J. Radioanal. Nucl. Chem.*, vol. 320, no. 1, 2019.

[100] S. Agostinelli *et al.*, "GEANT4 - A simulation toolkit," *Nucl. Instruments Methods Phys. Res. Sect. A Accel. Spectrometers, Detect. Assoc. Equip.*, vol. 506, no. 3, pp. 250–303, 2003.

VITA

Seth Michael Kilby grew up in the small town of Chatham, Illinois outside of the capital, Springfield. He graduated from Glenwood High School in 2012 (Titan for life). In the fall of 2012, he began his academic pursuits at Missouri S&T which culminated in an 8-year journey. He graduated Magna Cum Laude with a Bachelor of Science in Nuclear Engineering in May 2016. He began his Ph.D. studies that fall, and in December of 2018 he was awarded a Master of Science in Nuclear Engineering.

Throughout his Ph.D career, he fulfilled his research obligations which culminated in the completion of his dissertation in the summer of 2020. He received his Ph.D. in Nuclear Engineering in December of 2020 from Missouri University of Science Technology. Upon graduation, Seth continued nuclear fuel research as a staff member at Idaho National Laboratory.